Doctoral Dissertation (Censored)

博士論文（要約）

Nitrogen solubilities in the lower-mantle minerals: implications for the formation process of nitrogen reservoir in the deep Earth

（下部マントル鉱物への窒素溶解度:
地球深部における窒素貯蔵庫形成過程の考察）

A Dissertation Submitted for the Degree of Doctor of Philosophy

December 2020

令和 2 年 12 月　博士（理学）申請

Department of Earth & Planetary Science, Graduate School of Science,

The University of Tokyo

東京大学大学院理学系研究科

地球惑星科学専攻

Ko Fukuyama

福山　鴻

Abstract

Molecular nitrogen (N_2) constitutes approximately 78% of the Earth's atmosphere. Nitrogen is an essential element for sustaining life, and it plays a vital role in the biogeochemical cycle. Molecular nitrogen (N_2) is fixed as ammonium ions (NH_4^+) by microorganisms on the Earth's surface. Past variations in the atmospheric content of nitrogen, which are still under debate, may have played an essential role in regulating the early Earth's climate (e.g., Goldblatt et al., 2009; Wordsworth and Pierrehumbert, 2013). Therefore, nitrogen is an important volatile element in geoscience, but the geochemical behavior of nitrogen in the deep Earth remains controversial. Compared to other volatile elements, the amount of nitrogen in the bulk Earth, including the atmosphere, is one order of magnitude less (Marty et al., 2012). This constitutes the so-called "missing" nitrogen. However, the causes of nitrogen depletion have not been identified.

One of the hypotheses explaining this "missing" nitrogen is the existence of a nitrogen reservoir in the deep Earth. High-pressure and high-temperature experiments conducted by Watenphul et al. (2009) and Mallik et al. (2018) suggested that a deep nitrogen reservoir can be formed via subducting slabs. Li et al. (2013) and Yoshioka et al. (2018) also experimentally examined the possibility of nitrogen storage in the deep mantle through the solidification of a magma ocean. However, a nitrogen carrier in the lower mantle, which has the largest storage capacity in the Earth's interior, has not been discovered and its nitrogen storage mechanism has not been clarified. Furthermore, nitrogen solubility in ferropericlase, which is the secondary most abundant mineral in the lower mantle (e.g., Hirose et al., 2017), has not been reported.

In this thesis, I experimentally examined how much nitrogen is incorporated into lower-mantle minerals such as bridgmanite and periclase, including stishovite. In the high-pressure and high-temperature experiments, I used multi-anvil apparatus installed at the Geodynamics Research Center, Ehime University, under 28 GPa and 1400 °C–1700 °C. In all the experiments, Fe-FeO buffer was used to reproduce the redox state of the lower mantle. Nitrogen in recovered samples was analyzed using NanoSIMS installed at the Atmospheric Ocean Research Institute, The University of Tokyo and high-resolution SIMS (1280 HR2, CAMECA) installed at Centre de Recherches Pétrographiques et Géochimiques (CRPG). Nitrogen standard samples for NanoSIMS analysis were prepared by implanting $^{14}N^+$ into MgO single crystal plates and quartz glass plates at the National Institute for Materials Science (NIMS).

In the samples quenched from the lower mantle *P-T* conditions, bridgmanite, stishovite, and periclase were present in the solid phase, and hydrous melt (now, quenched crystals) coexisted in the liquid phase. A series of experimental results revealed that stishovite can incorporate more nitrogen than bridgmanite ($MgSiO_3$) and periclase (MgO). Nitrogen solubility in bridgmanite and periclase (MgO) increased with an increase in the FeO content. The nitrogen solubility in bridgmanite increased

with increasing experimental temperature. I suggest that bridgmanite and ferropericlase, the major minerals in the lower mantle, can form a nitrogen reservoir through the solidification of the magma ocean. Furthermore, the obtained results suggest that stishovite, formed by the transition of the SiO_2-rich oceanic crustal sedimentary rocks, can transport nitrogen to the lower mantle via the subducting slab. This thesis suggests that nitrogen was supplied to the lower mantle in the subduction zone approximately 4 billion years ago with the beginning of tectonic plate tectonics, forming a “hidden nitrogen” reservoir in the lower mantle.

Contents

1. Introduction

1.1. Origin of the Earth's atmosphere

Nitrogen is the fifth most abundant volatile element in the solar system, and molecular nitrogen (N_2) constitutes approximately 78 vol% of the present Earth's atmosphere. The Earth was formed by the accretion of planetesimals within a circumstellar disk (e.g., Rubie et al., 2015), and the early Earth's solar-type proto-atmosphere is believed to have been composed of hydrogen and helium. After the accretions, H_2O and CO_2 dominated the secondary Earth's atmosphere because of degassing from the magma ocean and impacts (e.g., Rubey. 1951; Elkins-Tanton, 2008; Abe and Matsui, 1988). Plate tectonics, oxidation processes of the crust and mantle, and their involvement in degassing processes led to the Earth's present nitrogen-rich atmosphere (e.g., Lammer et al., 2018).

Table 1.1 lists major components of rocky body planets' atmospheres. Mars and Venus have atmospheres composed mainly of CO_2. The Earth has significantly less CO_2 while also having a large amount of O_2, the second largest component of its atmosphere. This abundance is the result of carbonates and organic carbon in surface rocks as well as the existence of oxygen producing life forms. If all the carbon on the Earth's surface were released into the Earth's atmosphere and biogenetic oxygen is removed, CO_2 would occupy up to 99 vol% of the Earth's atmosphere, and its surface pressure would reach up to 80 atm. These conditions would then be comparable to those on Mars and Venus. The higher noble gas content in the Earth's atmosphere compared to the other rocky planets could have been caused by a late cometary contribution (e.g., Marty, 2012), but the origin of these differences in noble gas abundance between rock body planets is under debate.

Table 1.1. Volume ratio of gases in the rocky body planets' atmosphere.

	Venus	Earth	Mars
Surface pressure[1]	95 bar	1.01 bar	~6.36 mbar
Surface temperature (K)[2]	735	288	215
CO_2	96.5%[3]	0.04%	96%[4]
N_2	3.5%[3]	78.08%	1.89%[4]
O_2	<<[3]	20.95%	0.146%[4]
H_2O[5]	20-150 ppm	~4%	~210 ppm
^4He[5]	12^{+24}_{-8} ppm	5.24 ppm	—
Ne[5]	7 ± 3 ppm	18.18 ppm	2.5 ppm
Kr[5]	~25 ppb	1.14 ppm	0.3 ppm
Ar[5]	70 ± 25 ppm	9340 ppm	1.6%
Xe[5]	87 ppb	~1.9 ppb	0.08 ppm

1, 2: Reported by Fegley (1995) based on Schubert (1983), Warneck (1988), and Barth (1985).

3, 4: Estimated by Lammer et al. (2018) based on Oyama et al. (1980) and Mahaffy et al. (2013).

5: Reported by Fegley (1995) based on numerous previous studies.

Previous studies have indicated that nitrogen can have an impact on the early Earth's climate. Goldblatt et al. (2009), using a radiative-convective climate model, reported that the greenhouse effect of CO_2 was greater when the abundance of nitrogen was higher in the early Earth's atmosphere. The increase in the greenhouse effect is caused by the broadening of the absorption lines of greenhouse gases by increasing nitrogen concentration (Goldblatt et al., 2009). Wordsworth and Pierrehumbert (2013) reported that the early Earth would have been significantly warmed by H_2-N_2 collision-induced absorption in the infrared region. These suggestions might provide a solution to the faint young sun paradox that the whole Earth was not frozen in the Archean Earth despite the fainter Sun (Sagan and Mullen, 1972), although Goldblatt et al. (2009) mentioned that high nitrogen in the early Earth's atmosphere is not a single resolution to the faint young Sun paradox.

1.2. Chemical state of nitrogen in the biosphere and the Earth's interior

Nitrogen is an essential element of life. Nitrogen has various oxidation states; V, Ⅲ, Ⅱ, Ⅰ, 0, – Ⅰ, –Ⅲ, and combine with oxygen and hydrogen to form chemically active complex ions such as NO_3^-, N_2O, and NH_4^+. These chemical transformations occur through nitrogen fixation, nitrification, and denitrification. Figure 1.1 shows the changes in the oxidation state of nitrogen associated with these chemical changes. During fixation, atmospheric N_2 is converted into NH_4^+ by nitrogen-fixing bacteria. The Earth's atmosphere is the primary nitrogen inventory on Earth's surface. Nitrogen exists as chemically inert molecular nitrogen (N_2), which has a triple bond and geochemically behaves like noble gases. Nitrogen fixation plays a vital role in converting inert molecular nitrogen (N_2) into NH_4^+, which can be used by life on the Earth. Nitrification and denitrification also have an important impact on the nitrogen cycle in the biosphere, like nitrogen fixation, and a large amount of previous research on nitrogen flux in the Earth's surface has been conducted (e.g., Gruber and Galloway, 2008; Galloway et al., 2004; Galloway et al, 2008; Diaz et al, 2008; Duce et al., 2008; Johnston et al., 2009; Kuypers et al., 2018).

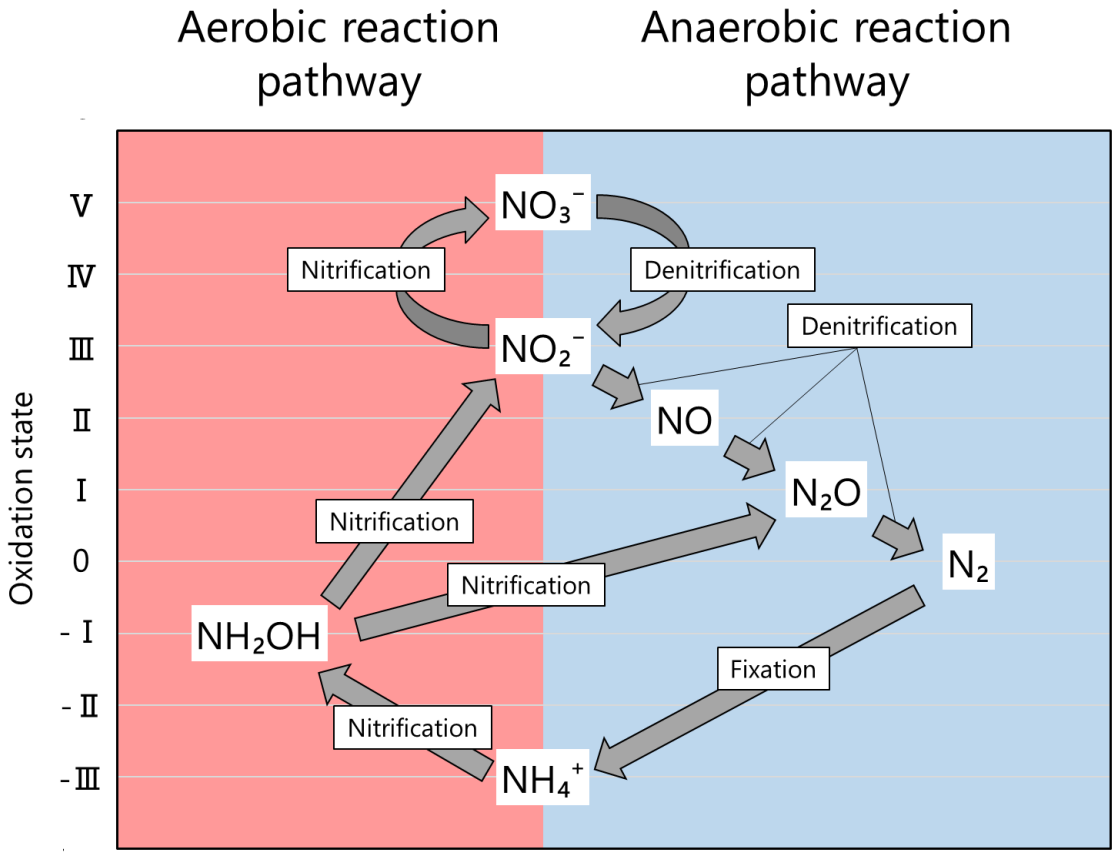

Figure 1.1 Changes in the oxidation state of nitrogen by nitrification, denitrification, and Fixation (modified from Canfield et al. (2010)).

Changes in the chemical state of nitrogen occur not only on the Earth's surface but also in the deep mantle. Oxygen fugacity is a critical parameter in controlling the physical and chemical properties of the mantle (e.g., Frost and McCammon 2008; Cline et al., 2018) and the chemical states of nitrogen change depending on the oxygen fugacity. Molecular nitrogen (N_2) is stable in oxygen fugacity corresponding to the shallow upper mantle; NH_3 or NH_4^+ is stable in oxygen fugacity corresponding to the lower mantle. The redox state in the shallow upper mantle is represented by fayalite-magnetite-quartz (FMQ) buffer, while the redox state in the deep part of the upper mantle and the lower mantle is represented by Fe-FeO buffer (e.g., Frost and McCammon et al., 2008). Frost et al. (2004) experimentally showed the chemical equilibrium of $Fe^{2+} \leftrightarrow Fe + Fe^{3+}$ by the coexistence of Fe-bearing bridgmanite under lower-mantle conditions. Smith et al. (2016) discovered metallic iron in super-deep diamonds originating from the lower mantle.

High-pressure experiments and thermodynamic calculations have shown that NH_4^+ can be incorporated into silicate minerals and silicate melts under reducing conditions (Watenphul et al., 2009; Watenphul et al., 2010; Li et al., 2013; Mikhail and Sverjensky, 2014; Li and Keppler, 2014). Nitrogen can also exist as N^{3-} in silicate minerals and silicate melts. Libourel et al. (2003) showed that nitrogen exists as N^{3-} in silicate melt from high-temperature experiments at atmospheric pressure and temperature at 1400 or 1425 °C under reducing conditions from IW–1.3 to IW–8.3. Li et al. (2013) suggested that nitrogen can exist as N^{3-} in silicate minerals such as clinopyroxene under Fe-FeO buffer. In this previous study by Li et al. (2013), high-pressure and high-temperature experiments were conducted using a piston-cylinder apparatus. Their experimental pressure conditions are from 1.5 to 3.5 GPa, and the experimental temperature ranges from 1100 °C to 1400 °C.

1.3. “Missing” nitrogen

As described before, nitrogen is a geochemically important element in discussing the volatile flux of the Earth’s surface and the early Earth’s climate. However, the geochemical behavior of nitrogen in the deep Earth remains controversial. Figure 1.2 shows the volatile abundances in the bulk Earth reported by Marty et al. (2012). In this figure, the bulk Earth, including the atmosphere, is composed of the Earth’s surface and the Earth’s mantle. The volatile abundances are normalized by the chemical compositions of the carbonaceous chondrites. Nitrogen, carbon, and hydrogen (water) contents in carbonaceous chondrites were based on Kerridge (1985) and Robert (2003). The noble gas contents in carbonaceous chondrites are based on Mazor et al. (1970) and Bogard et al. (1971). Volatile abundances on the Earth’s surface, which is considered to be composed of the atmosphere and the crust, are based on previous studies (Robert, 2003; Michael, 1988; Taylor and McLennan, 1985; Hirschmann and Dasgupta, 2009; Ozima and Podosek, 2002). Volatile abundances in the mantle are based on Marty et al. (2012).

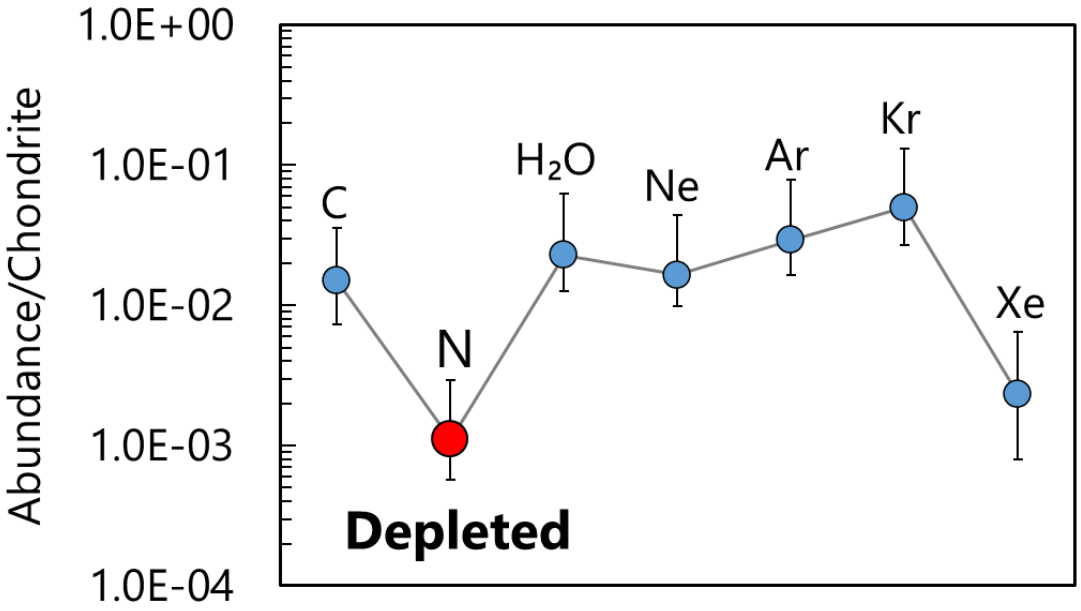

Figure 1.2. Volatile abundances in the bulk Earth normalized by chondrite compositions (modified from Marty et al. (2012)).

Xenon is depleted compared to other volatiles in the bulk silicate Earth, including the atmosphere, as shown in Figure 1.2, which is called “missing” xenon. Jephcoat (1998) implied that Xe was incorporated into the Earth’s core because Xe formed a condensed solid structure at high pressure and room temperature. Nishio-Hamane et al. (2010) conducted high-pressure and high-temperature experiments to inspect the reaction between iron and Xe under the condition corresponding to the outer core. To date, no reaction has been reported between iron and Xe under

high pressure and high temperature.

Compared to other volatile elements, nitrogen is also depleted by one order of magnitude in the bulk silicate Earth, including the atmosphere (Marty, 2012). This is referred to as "missing" nitrogen or "lost" nitrogen (e.g., Marty et al., 2012; Kaminsky and Wirth, 2017; Zedgenizov and Litasov, 2017). The causes of nitrogen depletion, compared to the terrestrial volatile inventory, have not been identified. According to Marty (2012), the C/N mass ratio of the bulk silicate Earth is estimated to be 311, which is much higher than the value of 24 for CI chondrites estimated by Kerridge (1985). In contrast, Bergin et al. (2015) estimated the C/N mass ratio of BSE to be 49.0 ± 9.3. This is partly because Bergin et al. (2015) estimated the bulk Earth's carbon content from the CO_2/Nb and CO_2/Ba ratios, which are different from the CO_2/noble gas ratio (e.g., Marty and Zimmermann, 1999). Recently, Marty et al. (2020) reported a high C/N mass ratio of 160–220 in the bulk silicate Earth. However, the C/N mass ratio in the bulk silicate Earth is still controversial, which means that whether "missing" nitrogen occurs in the bulk silicate Earth is not conclusive.

One hypothesis explaining the "missing" nitrogen is the loss of the early Earth's atmosphere by meteorite impact (e.g., Schlichting et al., 2015; Sakuraba et al., 2019). However, the late addition of impacting materials such as meteorites and comets are likely to have delivered nitrogen to the proto-Earth (e.g., Grewal et al., 2019a; Chen et al., 2019), which has made it difficult to explain "missing" nitrogen solely through atmospheric dissipation.

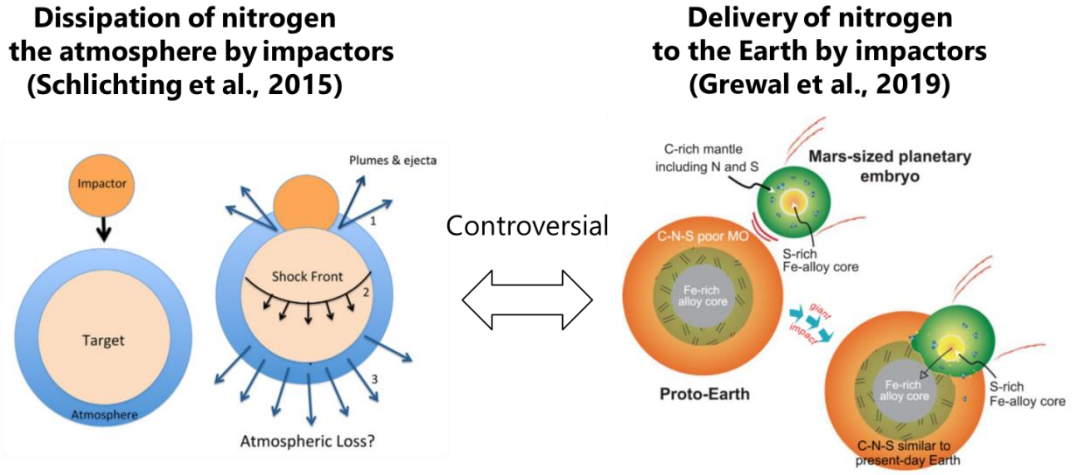

Figure 1.3. Schematics of the comparison between dissipation of nitrogen and delivery of nitrogen by impacts in previous studies (Schlichting et al., 2015; Grewal et al., 2019a).

A second hypothesis explaining the "missing" nitrogen is the existence of nitrogen reservoirs in the deep Earth. As shown in the previous chapter, nitrogen should exist as NH_3 or NH_4^+, not N_2, under reduced conditions such as the deep part of the upper mantle and the lower mantle. The correlation between N_2 and Ar abundances reported by Marty et al. (1995) is not necessarily correct. Zerkle and Mikhail (2017) suggested their underestimation of nitrogen content in the mantle because nitrogen exists as NH_3 and NH_4^+, which are compatible under the reducing mantle. In the next chapter, I will introduce previous studies reporting that the upper mantle, the mantle transition zone, and the lower mantle can be important reservoirs.

1.4. Possibility of nitrogen reservoir in the deep mantle

1.4.1. Structures and chemical composition of the Earth's mantle

In this chapter, I explain the structure of the Earth's interior before discussing nitrogen storage of the Earth's mantle. The Earth's mantle consists of four layers: upper mantle (depth<410 km), mantle transition zone (410–660 km), lower mantle (660–2700 km), and D" layer (2700–2900 km). The most abundant minerals in the upper mantle, the upper part of the mantle transition zone, the lower part of the mantle transition zone, and the lower mantle are olivine, wadsleyite, ringwoodite, and bridgmanite, respectively. Such a layered structure of the mantle has been clarified by seismological studies and is now widely accepted as the PREM model (Dziewonski and Anderson, 1981). The D" layer has been explained by the appearance of the post-perovskite phase found in high-pressure and high-temperature experiments using laser-heated diamond anvil cells (Murakami et al., 2004).

Ringwood et al. (1962) proposed a pyrolite model composed of MORB and dunite with a 1:4 ratio (wt.%) as the chemical composition of the upper mantle (see Table 1.2). The pyrolite model has been examined from various perspectives and is widely accepted (e.g., Jagoutz et al., 1979; Palme and Nickel, 1985; Hart and Zindler, 1986; Allègre et al., 1995; McDonough and Sun, 1995).

Table 1.2. Chemical composition of the pyrolite model (Ringwood, 1979)

	SiO_2	TiO_2	Al_2O_3	FeO	MnO	MgO	CaO	Na_2O	K_2O	P_2O_5	Cr_2O_3	NiO	Total
wt.%	45.1	0.2	3.3	8.0	0.15	38.1	3.1	0.4	0.03	0.02	0.4	0.2	100

However, whether the chemical composition of the lower mantle is pyrolitic or not is still controversial. The Mg/Si ratio (mol) of the pyrolite model is 1.26, which is notably higher than those of chondrites, the building blocks of the early Earth. Mg/Si ratio (mol) of carbonaceous chondrite, enstatite chondrite, and ordinary chondrite are 1.05-1.07, 0.93-0.96, and 0.73-0.88, respectively (Wasson and Kallemeyn, 1988). Murakami et al. (2012) and Mashino et al. (2020) suggested that the chemical composition of the lower mantle is rich in silicon compared to the pyrolitic lower mantle from high-pressure Brillouin scattering measurements of sound velocities. Experimental conditions were limited in these studies; additional experiments at higher pressure and higher temperatures corresponding to the lower mantle are expected in the future.

The pyrolitic Si-poor Earth's lower mantle can be caused by the existence of Si in the core. Allègre et al. (1995) estimated that the core contains approximately 7.3 wt.% silicon. Sakamaki et al. (2016) suggested silicon as a candidate light element to reduce Vp and the density of iron in good agreement with PREM. Ferropericlase occupies approximately 15 vol% of the pyrolitic lower mantle. On the other hand, Kaminsky (2012) reported that ferropericlase occupies up to 50-56% of inclusions in super-deep diamonds originating from the lower mantle. This discrepancy is likely caused by the

composition of the lower mantle that differs from that of the pyrolite model (Kaminsky, 2012). Constraints on the chemical composition of the lower mantle from natural samples are strong, but they do not necessarily reflect the whole lower mantle composition. Litvin (2014) reported that stishovite coexists with ferropericlase as inclusions in super-deep diamonds originating from the lower mantle, which contradicts the Mg-rich lower mantle reported by Kaminsky (2012). Wang et al. (2015) calculated the densities and elastic-wave velocities for several possible lower-mantle compositions with varying amounts of ferropericlase along a mantle geotherm. They found that the pyrolitic 8:2 volume fraction of bridgmanite and ferropericlase is consistent with the velocity and density of the PREM model in the lower mantle.

1.4.2. Formation of a nitrogen reservoir in the deep mantle through the solidification of magma ocean and nitrogen reservoir in the deep mantle inferred by natural samples

One of the hypotheses explaining the "missing" nitrogen is the possibility of a nitrogen reservoir in the deep Earth, as described before. Nitrogen behavior in the deep Earth remains unclear, but the solidification of the magma ocean is suggested as one of the formation processes of nitrogen reservoirs in the deep Earth (Li et al., 2013; Dalou et al., 2017; Yoshioka et al., 2018; Grewal et al., 2019b; Speelmanns et al., 2019). During the core formation process, including the magma ocean, nitrogen is thought to dissolve into liquid iron because of its siderophile behavior (Hashizume et al., 1997; Roskosz et al., 2013; Speelmanns et al., 2018). However, Dalou et al. (2017) reported a high C/N ratio in the bulk silicate Earth (BSE) that could not be explained solely by the core formation process because carbon is more siderophile than nitrogen under oxygen fugacity from IW−0.4 to IW−3.5. If a significant nitrogen reservoir was formed in the Earth's core, then nitrogen would not be depleted relative to carbon in the BSE, which conflicts with nitrogen depletion compared to carbon in the BSE, as reported by Marty et al. (2012). Additionally, the outer core's density cannot be explained solely by approximately 2.0 wt.% nitrogen, which can explain the bulk sound velocity of the outer core from first-principle molecular dynamic simulations (Bajgain et al., 2019). Therefore, the Earth's core might not be a major nitrogen reservoir. Li et al. (2013) determined the nitrogen solubilities in forsterite and enstatite at approximately 10 ppm and 100 ppm, respectively, by conducting high-pressure experiments under Fe-FeO buffer and suggested that the deep upper mantle can be a nitrogen reservoir through the solidification of the magma ocean. Yoshioka et al. (2018) reported that nitrogen solubility in bridgmanite is 21.5±18.1 ppm from high-pressure experiments using a multi-anvil apparatus under reduced conditions close to the Fe-FeO buffer. Presently, Yoshioka et al. (2018) conducted the only study on nitrogen solubility in bridgmanite, which occupies about 80 vol% of the lower mantle in the pyrolite model (e.g., Hirose et al., 2017). Carbon solubilities in mantle minerals were also determined by high-pressure and high-temperature experiments (Keppler et al., 2003, Shcheka et al., 2006). Keppler et al. (2003) reported carbon solubility up to 0.54 ppm in olivine, and Shcheka et al. (2006) reported that carbon solubilities in wadsleyite, ringwoodite, and bridgmanite are below the SIMS detection limit (i.e., below 30–200 ppb by weight). Figure 1.4 compares nitrogen solubilities and carbon solubilities in mantle minerals based on Keppler et al. (2003), Shcheka et al. (2006), Li et al. (2013), and Yoshioka et al. (2018). N/C ratio of solubilities in mantle minerals is high, and these experimental data strongly suggest that the Earth's mantle is the important nitrogen reservoir that can cause "missing" nitrogen.

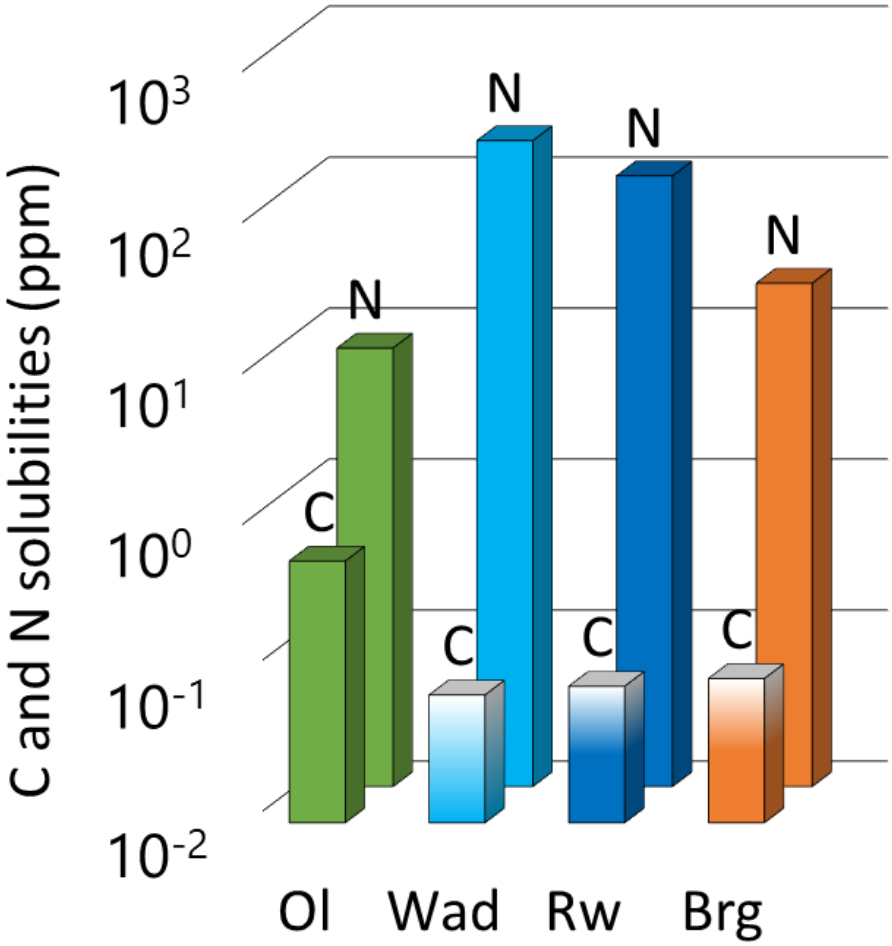

Figure 1.4. Comparison of carbon solubilities and nitrogen solubilities in mantle minerals based on Keppler et al. (2003), Shcheka et al. (2006), Li et al. (2013), and Yoshioka et al. (2018). Carbon solubilities in wadsleyite, ringwoodite, and bridgmanite are below the detection limit of SIMS (Shcheka et al., 2006).

Recently, nitrides such as cubic boron nitride, titanium nitride, and iron nitride have been discovered as inclusions of ophiolites derived from the upper mantle and super-deep diamonds originating in the lower mantle (e.g., Dobrzhinetskaya et al., 2009; Dobrzhinetskaya et al., 2014; Kaminsky and Wirth, 2017). It is important to investigate these natural samples originating from the deep Earth to directly determine the mantle's chemical composition, although such information can be local in the Earth's interior. Representative nitrides from natural samples are introduced below (Figure 1.5).

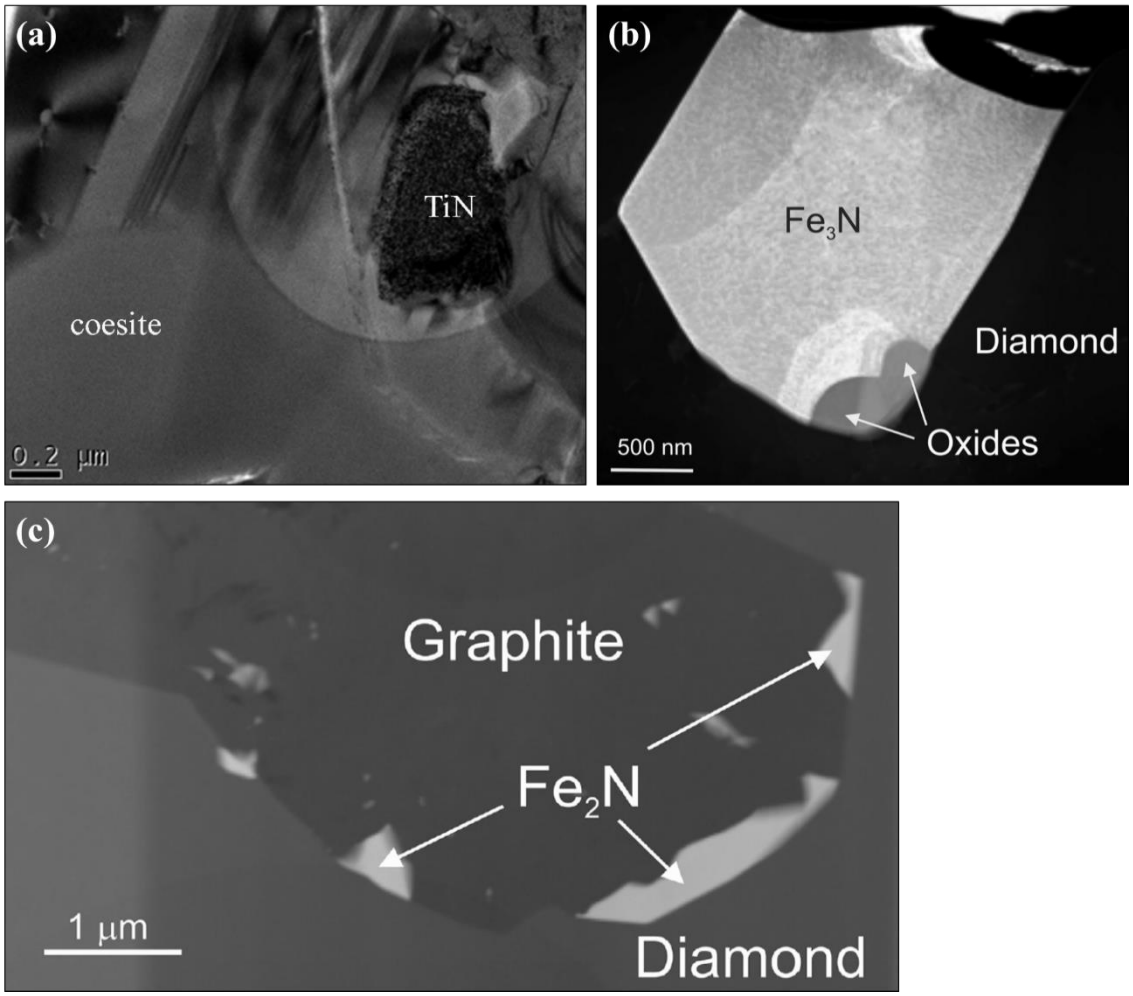

Figure 1.5. Nitrides discovered from the ophiolite and super-deep diamonds. (a) Titanium nitride discovered from ophiolite (Dobrzhinetskaya et al., 2014), (b) Iron nitride (Fe_3N, Kaminsky and Wirth, 2017), (c) Iron nitride (Fe_2N, Kaminsky and Wirth, 2017).

1.4.3. Nitrogen abundance in the bulk silicate Earth inferred by high-pressure experiments

Li et al. (2013), Yoshioka et al. (2018), and Speelmanns et al. (2019) suggested that the nitrogen reservoir in the deep mantle was formed in the magma ocean. Mantle minerals can be hosts of nitrogen in the deep Earth. Li et al. (2013) reported that nitrogen solubilities in forsterite and enstatite were up to 10 ppm and 100 ppm, respectively. Yoshioka et al. (2018) reported nitrogen solubility in bridgmanite as 21.5 ± 18.1 ppm. Figure 1.6 shows nitrogen solubilities in mantle minerals based on the pyrolite model. In the upper mantle and the mantle transition zone, almost all of the nitrogen solubilities in mantle minerals were clarified under various *P-T* conditions. However, nitrogen solubilities in the lower-mantle minerals were determined at only 24 GPa and 1600 °C. Furthermore, nitrogen solubilities in ferropericlase, which occupies 15 vol% in the lower mantle, have not been clarified.

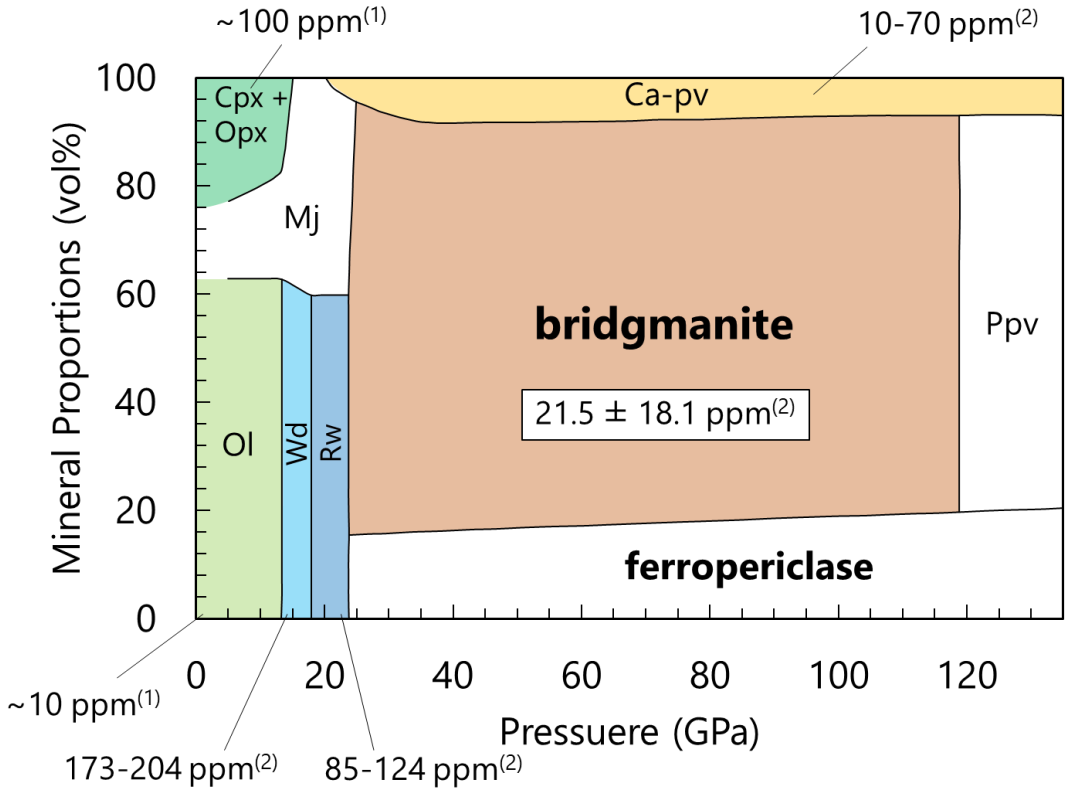

Figure 1.6. Nitrogen solubilities in mantle minerals in the pyrolite model (modified from hirose et al. (2017)) based on (1) Li et al. (2013) and (2) Yoshioka et al. (2018). Cpx: clinopyroxene, Opx: orthopyroxene, Mj: majorite, Ol: olivine, Wd: wadsleyite, Rw: ringwoodite, Ca-pv: $CaSiO_3$ perovskite, Ppv: post-perovskite.

1.4.4. Formation of deep nitrogen reservoir via subducting slabs

The mass of nitrogen outgassing from the Earth's interior is essential information for discussing the formation process of nitrogen reservoirs. Sano et al. (2001) reported that nitrogen outgassing fluxes from the subduction zone, mid-ocean ridge, and hot spot based on $\delta^{15}N$–$N_2/^{36}Ar$ were 1.68×10^7 kg/year, 6.16×10^7 kg/year, and 1.15×10^5 kg/year, respectively. The mass of nitrogen outgassing from the lower mantle (hot spot) is two orders of magnitude lower than those of the subduction zone and mid-ocean ridge. This implies that nitrogen reserved in the lower mantle is difficult to be released into the atmosphere. Sano and Williams (1996) estimated that the masses of carbon outgassing from the subduction zone, mid-ocean ridge, and hot spot are 3.72×10^7 kg/year, 1.80×10^7 kg/year, and 3.48×10^5 kg/year, respectively. From these nitrogen and carbon fluxes from the Earth's interior, the N/C ratios from the deep Earth can be obtained and are listed in Table 1.3. N/C ratios in outgassing of subduction and hot spot are approximately one order of magnitude lower than that from the mid-ocean ridge. Compared to carbon, the formation of a nitrogen reservoir in the lower mantle via subducting slabs can effectively deplete nitrogen.

Table 1.3. Mass of nitrogen and carbon outgassing from the Earth's interior.

	Subduction zone (kg/year)	Mid-ocean ridge (kg/year)	Hot spot (kg/year)
N outgassing[1]	1.68×10^7	6.16×10^7	1.15×10^5
C outgassing[2]	3.72×10^7	1.80×10^7	3.48×10^5
N/C	0.45	3.42	0.33

1. Estimated based on Sano et al. (2001).

2. Estimated based on Sano et al. (1996).

The Earth is the only planet in the solar system with plate tectonics (Korenaga et al., 2013). In subduction zones, various volatile elements are transported into the deep Earth. Such a volatile cycle via subduction has remained a very important research topic in geochemistry. Mysen (2019) suggested that a nitrogen reservoir in the mantle can be formed in the mantle via subducting slabs. Sediments and continental crusts in subducting slabs can be rich in nitrogen. Nitrogen in sediments originates from organic materials, and potassium ion (K^+) in continental crusts can be substituted for ammonium ions (NH_4^+) (e.g., Goldblatt et al., 2009). The nitrogen concentrations of sediments and upper crusts are 560 ppm and 150 ppm, respectively (Johnson and Goldblatt, 2015). Under anoxic conditions at about 150 °C, amino acids in organic materials decompose and released nitrogen is incorporated into clay minerals, micas, and feldspars as ammonium ions (NH_4^+) by substituting for potassium ion (K^+). (Williams et al., 1992). Busigny et al. (2003) reported that the mass of sedimentary nitrogen recycled via subduction is 7.6×10^8 kg/year based on the correlation between nitrogen and potassium contents. Additionally, the flux of nitrogen subducted by metagabbros is $4.2\ (\pm 2.0) \times 10^8$ kg/year based on the $\delta^{15}N$–Cu correlation (Busigny et al., 2011). The amount of nitrogen flux into the deep mantle via subduction is one order of magnitude higher than the outgassing flux of nitrogen reported by Marty et al. (1995) and Sano et al. (2001). Subduction of nitrogen originating from organic materials in sediments is also inferred from the nitrogen isotope ratio $\delta^{15}N$ (Marty and Dauphas, 2003; Halama et al., 2010). Marty and Dauphas (2003) reported that $\delta^{15}N$ of deep mantle material sampled from mantle plumes (Kola Devonian magmatic province, Iceland, Loihi Seamount, Hawaii, Society Islands) is higher than that of the atmosphere ($\delta^{15}N = 0$) by up to 8 ‰, which was caused by subducted post-Archean sediments, which are abundant in ^{15}N. Thus, geochemical observations strongly suggest that a large amount of nitrogen is transported via subduction, forming a nitrogen reservoir in the deep Earth extending to the lower mantle.

As previously discussed, a large amount of nitrogen is transported into the deep mantle via subducting slabs. High-pressure and high-temperature experiments indicated that nitrogen can be transported into the deep upper mantle by various NH_4-bearing minerals, as listed in Table 1.4.

Table 1.4. NH_4-minerals synthesized by high-pressure and high-temperature experiments.

Minerals	Chemical composition	*P-T* synthesis conditions
NH_4-Cymrite[1]	$NH_4AlSi_3O_8 \cdot H_2O$	~7.8 GPa, 800 °C
NH_4-Si-wadeite[1]	$((NH_4)_2Si_4O_9)$	~10 GPa, 700 °C
NH_4-Hollandite[1]	$NH_4AlSi_3O_8$	~12.8 GPa, 700 °C
NH_4-Diopside[2]	$CaMgSi_2O_6$-$(NH_4)M^{3+}Si_2O_6$, M = Cr or Al	12.8 GPa, 750 °C
NH_4-Phengite[3]	$NH_4(Mg_{0.5}Al_{1.5})(Al_{0.5}Si_{3.5})O_{10}(OH)_2$	~4 GPa, 700 °C
NH_4-Muscovite[4]	$NH_4(Mg, Fe^{2+})Si_4O_{10}(OH)_2$	6.3 GPa, 1000 °C
NH_4-Smectite[5]	—	~2.5 GPa, 500 °C
NH_4-Tobelite[5]	$NH_4Al_2(AlSi_3O_{10})(OH)_2$	~7.7 GPa, 700 °C
Buddingtonite[5]	$NH_4AlSi_3O_8$	~7.7 GPa, 700 °C

1. Watenphul et al. (2009), 2. Watenphul et al. (2010), 3. Yang et al. (2017), 4. Sokol et al. (2018), 5. Cedeño et al. (2019).

To date, many NH_4-bearing silicate minerals have been synthesized under conditions corresponding to cold slabs subducting down to the deep upper mantle (Watenphul et al., 2009; Watenphul et al., 2010; Sokol et al., 2018; Cedeño et al., 2019). Sediments and continental crusts in subducting slabs can be rich in nitrogen (e.g., Johnson and Goldblatt, 2015), and these minerals can introduce a significant amount of nitrogen into the deep upper mantle. However, the experimental conditions reported in these recent studies are limited to conditions in the deep upper mantle (< 13 GPa). Nitrogen behaviors in the mantle transition zone (> 13 GPa) and the lower mantle (> 24 GPa) remain unknown.

1.5. Purpose of this study

As already mentioned, the formation of a nitrogen reservoir in the lower mantle remains unclear. In particular, there are no reports on nitrogen solubilities in ferropericlase, despite it being the second most abundant mineral in the lower mantle. The purpose of this thesis is to determine a nitrogen carrier into the lower mantle and experimentally reveal the nitrogen capacity in the lower mantle by investigating nitrogen solubilities in lower-mantle minerals.

2. Methods

2.1. Starting materials

Four different starting materials were prepared: a powdered mixture of MgO and SiO_2 (quartz) for the ideal bridgmanite composition ($MgSiO_3$), a powdered mixture of Al_2O_3, MgO, $Mg(OH)_2$, and SiO_2 (quartz) for Al-bearing hydrous bridgmanite composition ($MgSi_{0.9}Al_{0.1}H_{0.1}O_3$), a powdered mixture of MgO, SiO_2 (quartz), and Fe_2SiO_4 for Fe-bearing bridgmanite composition ((Mg, Fe)SiO_3), and powdered MgO (see Table 2.1). ^{15}N–substituted ammonium nitrate ($^{15}NH_4{}^{15}NO_3$, SHOKO SCIENCE Corp.) was used as a nitrogen source to distinguish sample-derived nitrogen from nitrogen in resin and atmospheric or instrumental nitrogen. Contamination from atmospheric ^{15}N is negligible because the natural abundance of ^{15}N is more than two orders of magnitude lower than that of the atmospheric ^{14}N. Furthermore, the depth profiles of ^{15}N concentration in stishovite and bridgmanite were constant, suggesting that ^{15}N contamination was negligible (see Figure 2.9). The starting materials and $^{15}NH_4{}^{15}NO_3$ were enclosed in a Pt sample capsule (see Figure 2.3). The mass ratio of the starting materials to the nitrogen source was almost 5:1 for each experiment (molar ratio of starting materials to the nitrogen source was also almost 5:1). The starting material was separated from $^{15}NH_4{}^{15}NO_3$ by gold foil with a thickness of 30 μm in Run no. OS3083. In other runs, the starting material and $^{15}NH_4{}^{15}NO_3$ were mixed.

Table 2.1. Chemical compositions of starting materials.

	Chemical composition	SiO_2 (wt.%)	Al_2O_3 (wt.%)	MgO (wt.%)	$Mg(OH)_2$ (wt.%)	Fe_2SiO_4 (wt.%)	total
a	$MgSiO_3$	59.85	0	40.15	0	0	100.00
b	$MgSi_{0.9}Al_{0.1}H_{0.1}O_3$	53.87	5.08	38.15	2.90	0	100.00
c	$(Mg_{0.85}Fe_{0.15})SiO_3$	52.87	0	32.59	0	14.54	100.00
d	$(Mg_{0.9}Fe_{0.1})SiO_3$	55.13	0	35.03	0	9.84	100.00
e	$(Mg_{0.95}Fe_{0.05})SiO_3$	57.45	0	37.55	0	5.00	100.00
f	MgO	0	0	100	0	0	100.00

Fayalite (Fe_2SiO_4) was synthesized using an electric furnace installed at The University Museum, The University of Tokyo (Figure 2.1). The redox state of iron in fayalite is Fe^{2+}, which is in the range of the Fe-FeO buffer used for this research. The starting materials for fayalite were composed of powdered SiO_2 and Fe_2O_3 with a chemical formula equivalent to Fe_2SiO_5. The heating duration was 72 h at 1100 °C. During heating, the gas flux ratio of CO_2 to H_2 was 9:5. The recovered fayalite was identified using a desktop X-ray diffractometer (MiniFlexII, Rigaku). XRD of the synthesized fayalite used as the stating materials is shown in Figure 2.2.

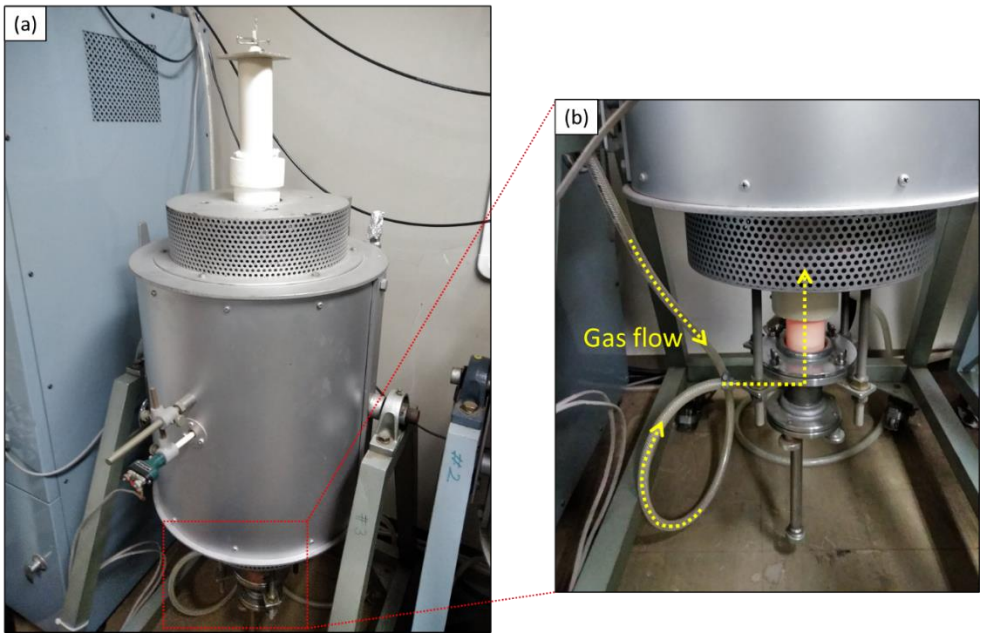

Figure 2.1. Electric furnace for the synthesis of Fe_2SiO_4 installed at The University Museum, The University of Tokyo (Mikouchi Lab).

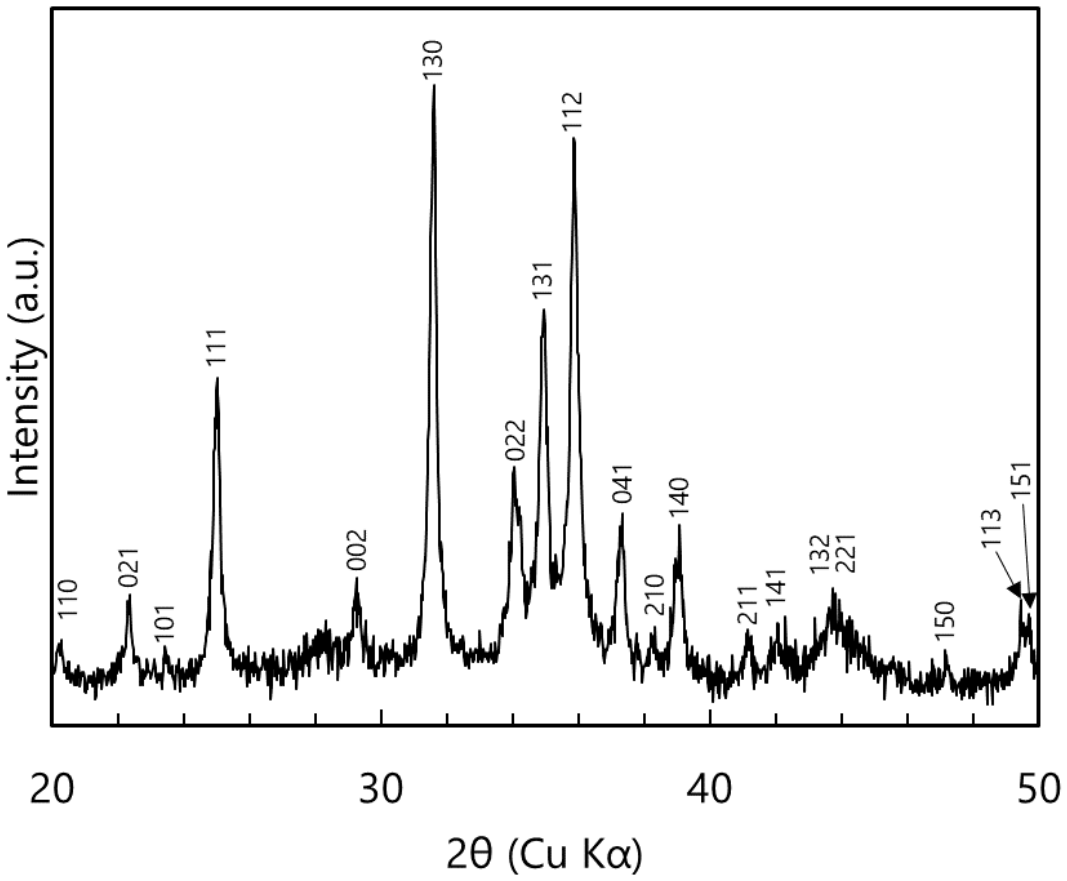

Figure 2.2. XRD pattern obtained from fayalite used for starting materials in this research.

2.2. High-pressure experiments using multi-anvil apparatus

High-pressure and high-temperature experiments were conducted using a Kawai-type 2000-ton multi-anvil apparatus (Orange-2000) and a Kawai-type 3000-ton multi-anvil apparatus (Orange-3000) installed at the Geodynamics Research Center, Ehime University (GRC), Japan. Orange-2000 was used only for Run no. OS3083 and all other experiments were conducted using Orange-3000. All experiments were conducted at 28 GPa and temperatures from 1400 °C to 1700 °C. The Ehime University calibrated the relationship between pressure and load in advance. The heating duration for all experiments was 2 h. I used tungsten carbide anvils (Tungaloy F-grade and Fujilloy F08) with 4 mm truncated edge length (TEL). Figure 2.3 shows the cell assembly used in this study. The platinum sample capsule was surrounded by Fe-FeO buffer (iron wüstite buffer) to reproduce the oxygen fugacity corresponding to the lower mantle condition (Frost et al., 2004; Frost and McCammon, 2008; Smith et al., 2014). We used 150 mesh iron powder and iron oxide (FeO) powders with 8 μm or 200 mesh for Fe-FeO buffer (Fe:FeO = 2:1 (wt.%)). Then, 20–50 μl of water was added to 0.5 g of Fe-FeO buffer. The platinum capsule was enclosed in a gold outer capsule. The two gold capsules were insulated from the Re heater with a thickness of 25 μm using a magnesia sleeve. The temperature was measured using a W-Re (W3%Re-W25%Re) thermocouple inserted in the octahedron and attached to the gold capsules. Hydrogen fugacity in the inner and outer capsules was assumed to be equal because of the high hydrogen permeability of platinum compared to that of gold. $^{15}NH_4{}^{15}NO_3$ decomposes into $^{15}N_2O$ and H_2O at high temperatures. $^{15}NH_3$ is formed in the ^{15}N-H-O fluid under fO_2 conditions in an inner platinum capsule.

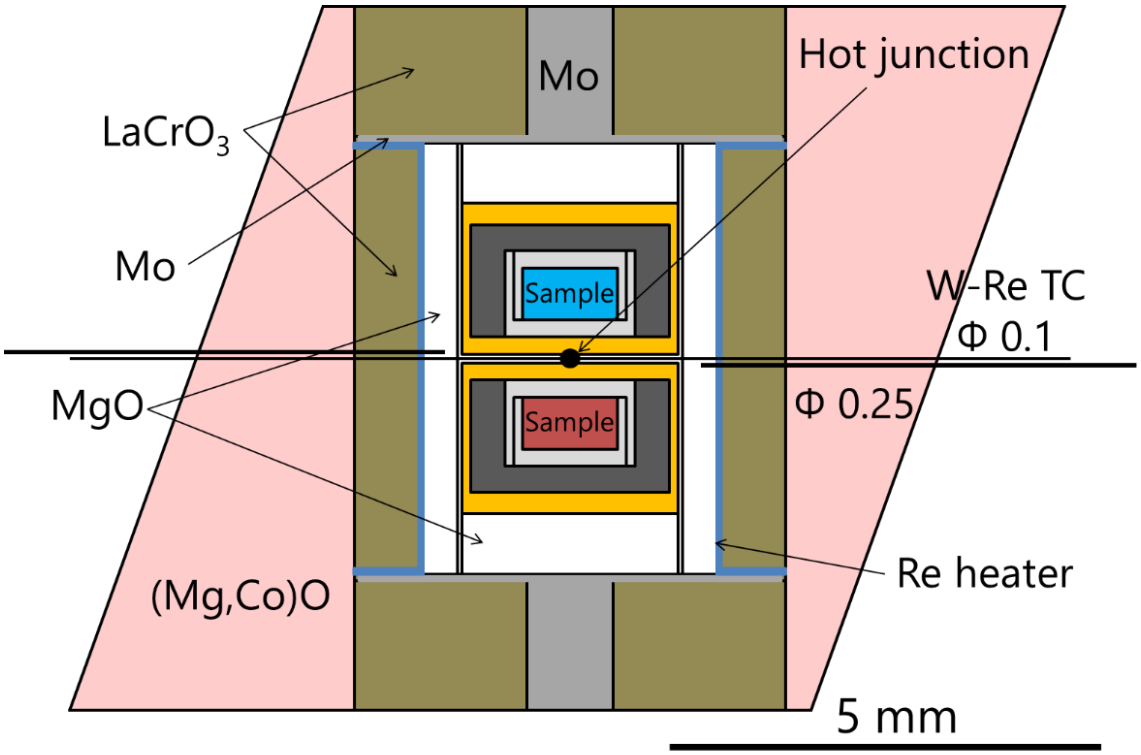

Figure 2.3. Cell assembly used in high-pressure and high-temperature experiments using the multi-anvil apparatus. A $LaCrO_3$ sleeve plays a thermal insulator. A platinum sample capsule was made by combining two platinum tubes with 0.1 mm wall thickness, and outer diameters of 1.3 mm and 1.5 mm, respectively, by welding each end of the capsules. A gold capsule was made from a gold tube with 0.1 mm wall thickness and 2.5 mm outer diameter.

Nitrogen solubilities in bridgmanite ($MgSiO_3$) and stishovite (SiO_2) in Al-bearing and Al-free systems were investigated at 1400 °C, 1500 °C, 1620 °C, and 1700 °C. These experimental conditions are plotted in Figure 2.4. Nitrogen solubilities in periclase (MgO) were investigated at 1400 °C, 1500 °C, 1600 °C, and 1700 °C. These experimental conditions range from the slab geotherm and mantle geotherm, which enable us to discuss nitrogen behavior in the lower mantle. For the Fe-bearing system, all experimental conditions were fixed at 28 GPa and 1620 °C, but the Fe content of the starting materials was changed, as shown in chapter 3.1.

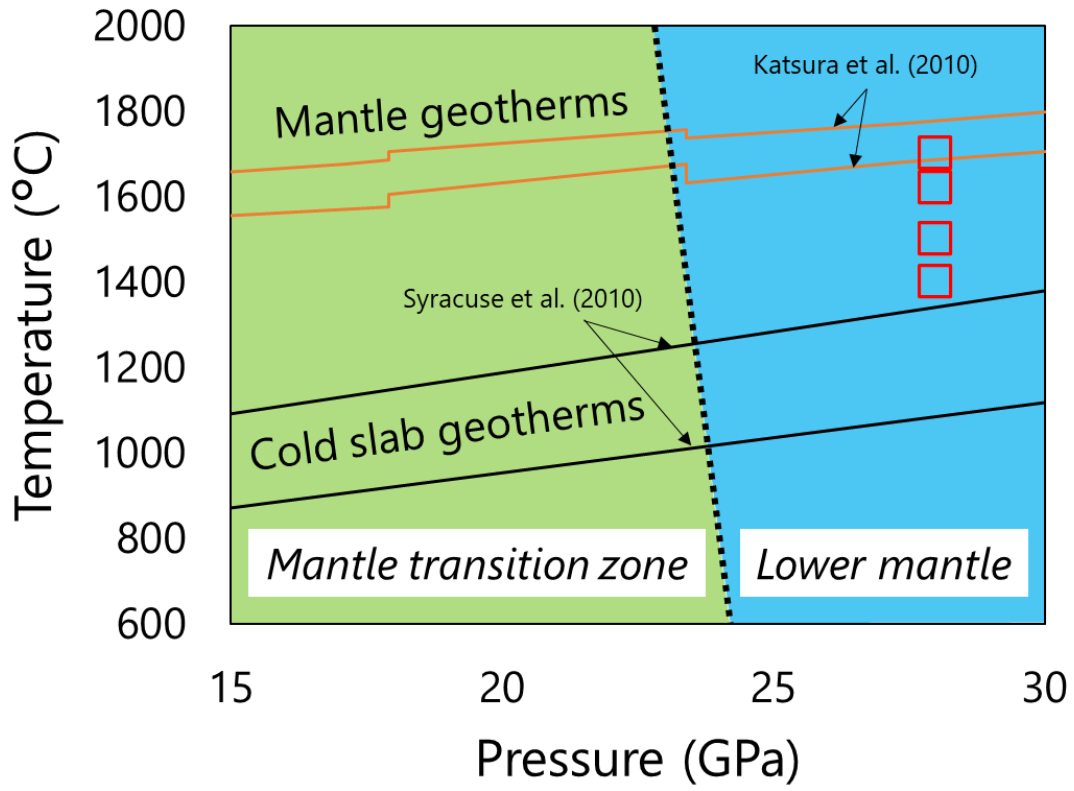

Figure 2.4. Mantle geotherms, slab geotherms, and experimental conditions for the investigation of nitrogen solubilities in bridgmanite ($MgSiO_3$) and stishovite (SiO_2) in Al-bearing system and Al-free system. Red squares represent experimental conditions in the present study.

2.3. FE-SEM-EDS

The chemical compositions of the quenched minerals were analyzed using FE-SEM (JSM-7000F; JEOL) under 15 kV and 87.4-130.4 μA before and after SIMS analysis. In discussing the relationship between Fe content or Al content and nitrogen solubilities in minerals, chemical compositions determined after Secondary Ion Mass Spectrometry (SIMS) analysis were used.

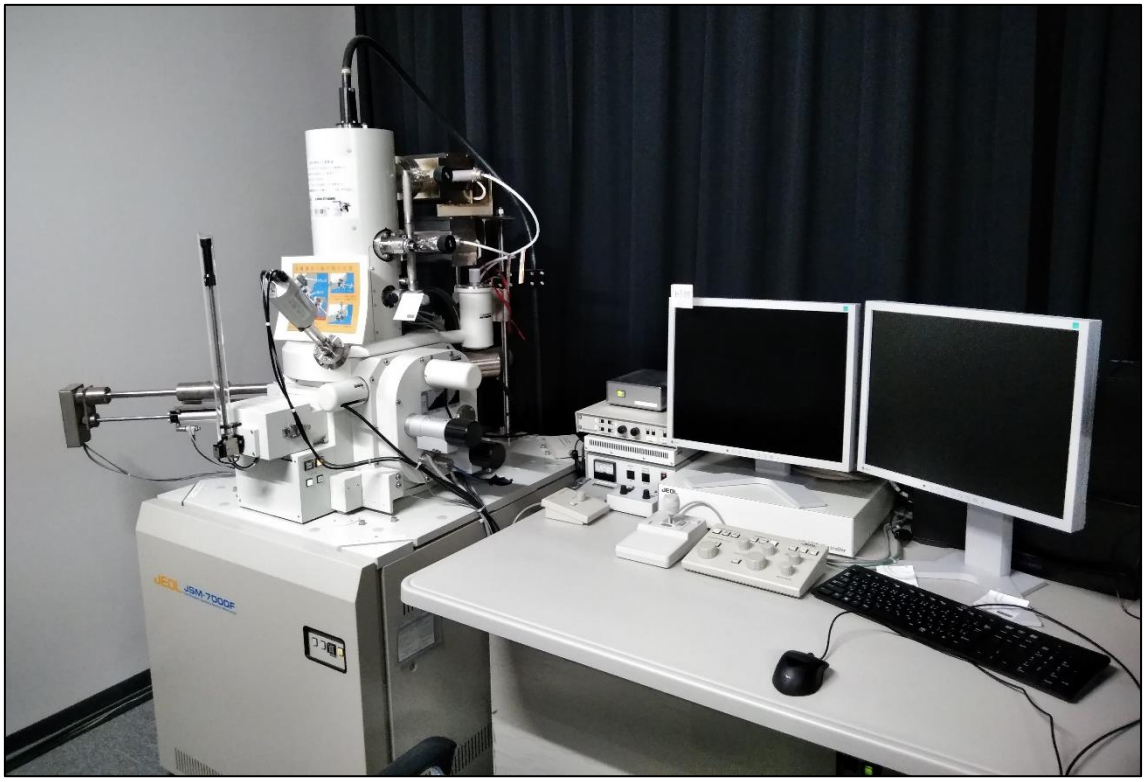

Figure 2.5. FE-SEM-EDS installed at Department of Earth & Planetary Science, The University of Tokyo.

All samples recovered from high pressure and high temperature were mounted in resin (petropoxy 154, Maruto Instrument Corp) for SEM analysis. The surfaces of the mounted samples were polished using sandpapers and corundum paste. Prior to SEM analysis, the surfaces of the samples were coated with carbon.

2.4. FE-EPMA

The chemical compositions of the quenched minerals determined were redetermined using FE-EPMA (JXA-8530F; JEOL) to make correction to the Mg/Si ratios of bridgmanite determined using FE-SEM-EDS. Six species of standards; garnet, enstatite, augite, plagioclase, San Carlos olivine, and JB-1 were used for FE-EPMA analysis.

Figure 2.6. EPMA installed at Department of Earth & Planetary Science, The University of Tokyo.

Surface of the mounted samples were polished using corundum paste and was coated with carbon.

2.5. Raman spectroscopy

To determine the mineral phases, Raman spectra were obtained using a micro-Raman spectrometer (Figure 2.7) using an Ar ion laser of 514.5 nm and 6 mW power for excitation. The beam size was approximately 2 μm in diameter. The exposure time was 30 s.

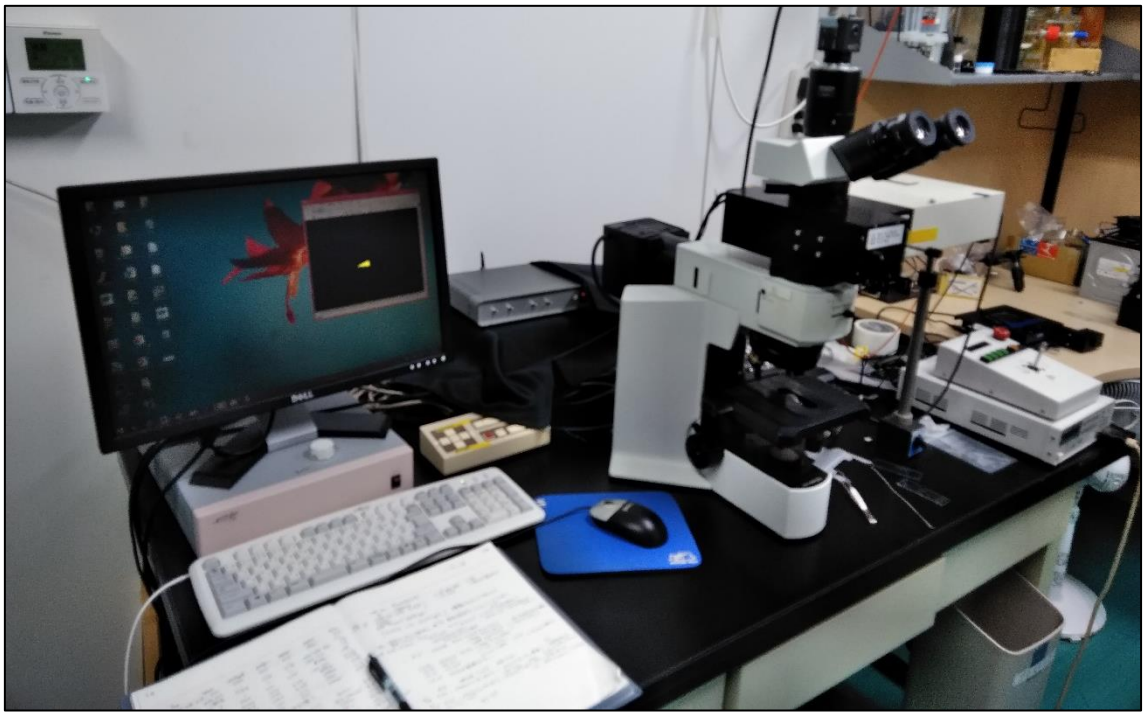

Figure 2.7. Laser Raman microprobe installed at Geochemical Research Center, The University of Tokyo.

Before obtaining the Raman spectra, the carbon coating on the surfaces of the samples was removed through polishing with corundum paste.

2.6. NanoSIMS

Secondary Ion Mass Spectrometry (SIMS) was used for the quantitative analysis of nitrogen. Nitrogen in diamonds has been detected as CN^- in previous studies (e.g., Smart et al., 2011). Recently, Li et al. (2013) and Füri et al. (2018) reported the possibility of detecting nitrogen as $^{15}N^{16}O^-$ from silicate minerals and silicate glasses that contain oxygen in their structures. In this study, nitrogen was detected as $^{15}N^{16}O^-$ using NanoSIMS (CAMECA, Figure 2.8) installed at the Atmosphere and Ocean Research Institute (AORI), The University of Tokyo, Japan. NanoSIMS has a magnetic sector mass analyzer with seven parallel detectors, and it can detect up to seven ion species simultaneously as secondary ions. In the analysis, a Cs^+ primary ion beam with 2 nA was used, and an e-gun was used at 500–800 nA to avoid charge-up. The diameter of the primary ion beam was 2 μm, and the raster was 5 μm ×5 μm or 10 μm ×10 μm. Count durations in $^{18}OH^-$, $^{30}Si^-$, $^{30}SiH^-$, $^{28}SiH_2^-$, and $^{15}N^{16}O^-$ were 2 s, 2 s, 2 s, 10 s, and 10 s, respectively. The analysis time for the recovered sample was 600 s, and those for $^{14}N^+$–implanted standards were 1000 s or 1500 s. The surfaces of the samples were coated with gold.

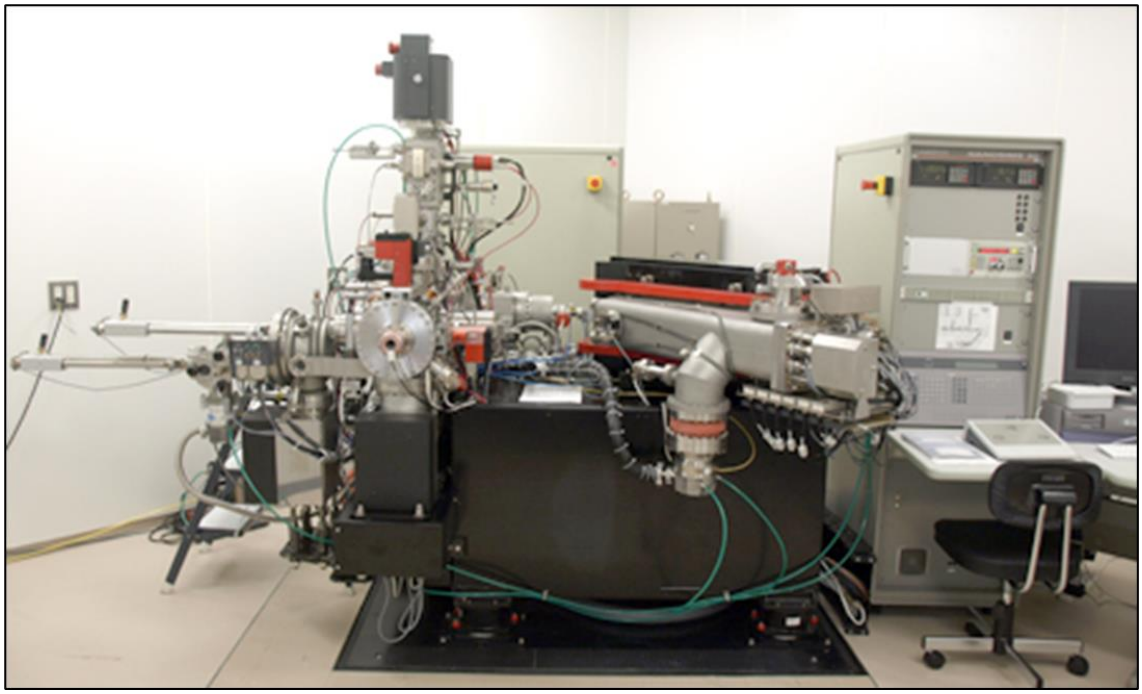

Figure 2.8. NanoSIMS installed at Atmosphere and Ocean Research Institute, The University of Tokyo.

The respective nitrogen contents of stishovite and bridgmanite recovered from the run products were compared by observing the $^{15}N^{16}O^-/^{30}Si^-$ ratio. Because of the insufficient mass resolution of the NanoSIMS (mass resolving power $M/\Delta M \fallingdotseq 4{,}000$), the $^{15}N^{16}O^-$ and $^{29}SiH_2^-$ ions cannot be separated. Therefore, we exclusively calculated the $^{15}N^{16}O^-$ ion counts by subtracting the

potential $^{29}SiH_2^-$ ion counts from $^{15}N^{16}O^-$ ion counts detected by NanoSIMS. The potential $^{29}SiH_2^-$ ion counts were estimated from the $^{28}SiH_2^-$ ion counts based on the natural $^{29}Si/^{28}Si$ isotopic ratio (5.06×10^{-2}). Figure 2.9 shows the time-dependence of the representative ion counts. In stishovite, the ion counts of $^{15}N^{16}O^-$ were higher than those of $^{28}SiH_2^-$, indicating that the contribution of the $^{29}SiH_2^-$ to $^{15}N^{16}O^-$ was negligible. In contrast, in bridgmanite, the ion counts of $^{15}N^{16}O^-$ were much lower than those of $^{28}SiH_2^-$. The estimated $^{29}SiH_2^-$ ion counts were at most 65.1% of the original $^{15}N^{16}O^-$ ion counts. Therefore, in bridgmanite, we had to use high-resolution SIMS to directly detect $^{15}N^{16}O^-$ ion counts as illustrated in chapter 3.8.

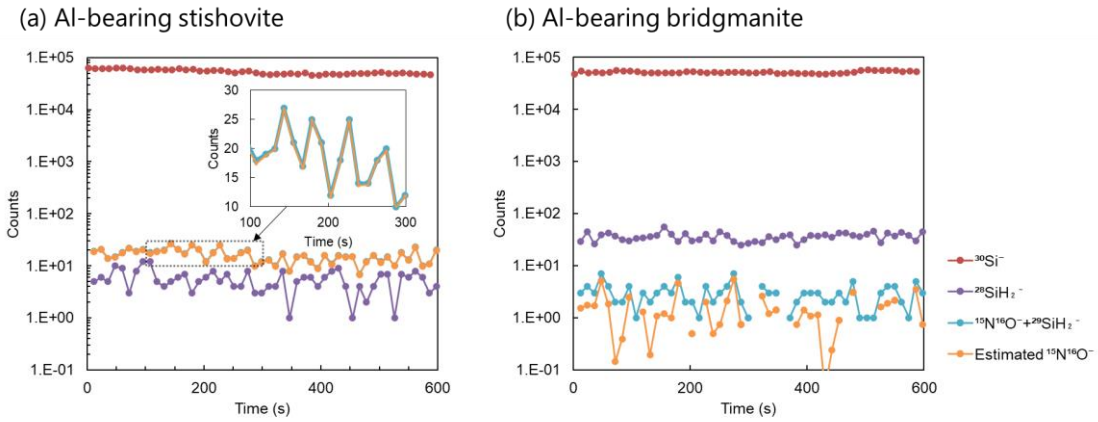

Figure 2.9. Ion mass counts. (a): Al-bearing stishovite (St1 in OT2259). The inset shows enlarged trends for ion counts of $^{15}N^{16}O^-$ + $^{29}SiH_2^-$ and estimated $^{15}N^{16}O^-$. These two values coincide. (b): Al-bearing bridgmanite (Brg2 in OT2259).

2.7. Nitrogen standards for stishovite and periclase

I prepared $^{14}N^{+}$-implanted standard samples to estimate nitrogen concentrations in stishovite and periclase at the National Institute for Materials Science (NIMS). $^{14}N^{+}$ ions were implanted into quartz glass plates and periclase single crystal plates at 132 keV with doses of 2.44×10^{14} and 3.66×10^{15} ions/cm^2, respectively, using an ion Implanter (RD-200l, Nissin Electric Co. Ltd.). The volume and depth of the post-bombardment craters of quartz glass plates after NanoSIMS analysis were measured using a confocal laser scanning microscope (Olympus Corp., Figure 2.10). The post-bombardment formed holes on the sample surface after SIMS analysis through primary ion irradiation.

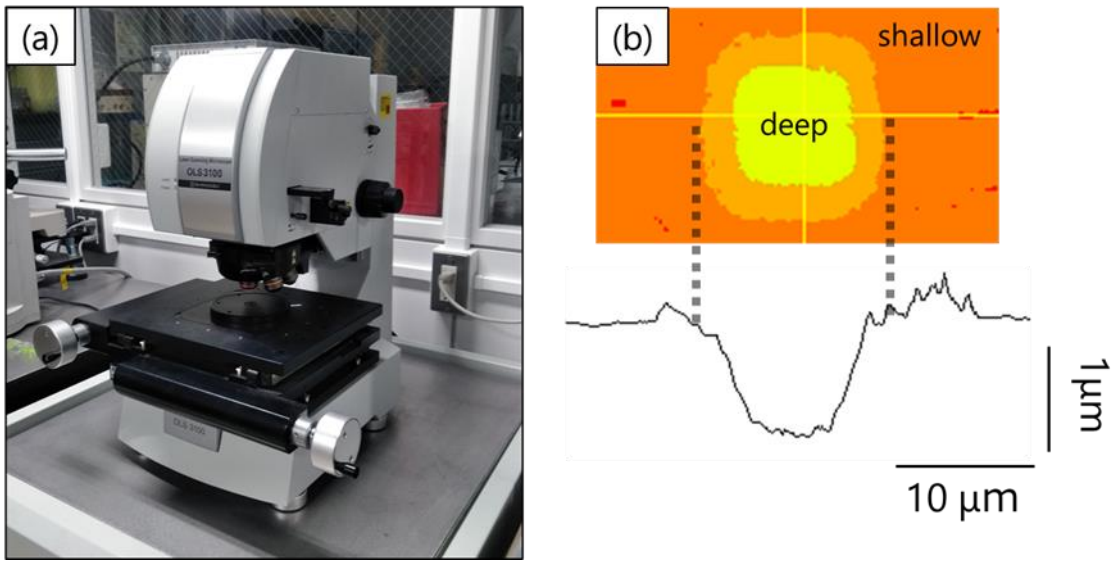

Figure 2.10. (a) A confocal laser scanning microscope installed at Geochemical Research Center, The University of Tokyo. (b) Example of analysis results.

2.8. TRIM calculation

I used TRIM calculations to simulate the ion range in $^{14}N^{+}$-implanted plates such as quartz glass and MgO single crystals. The results of TRIM simulation on quartz glass and MgO single crystals at an accelerating voltage of 132 keV are shown in Figure 2.11 and Figure 2.12, respectively.

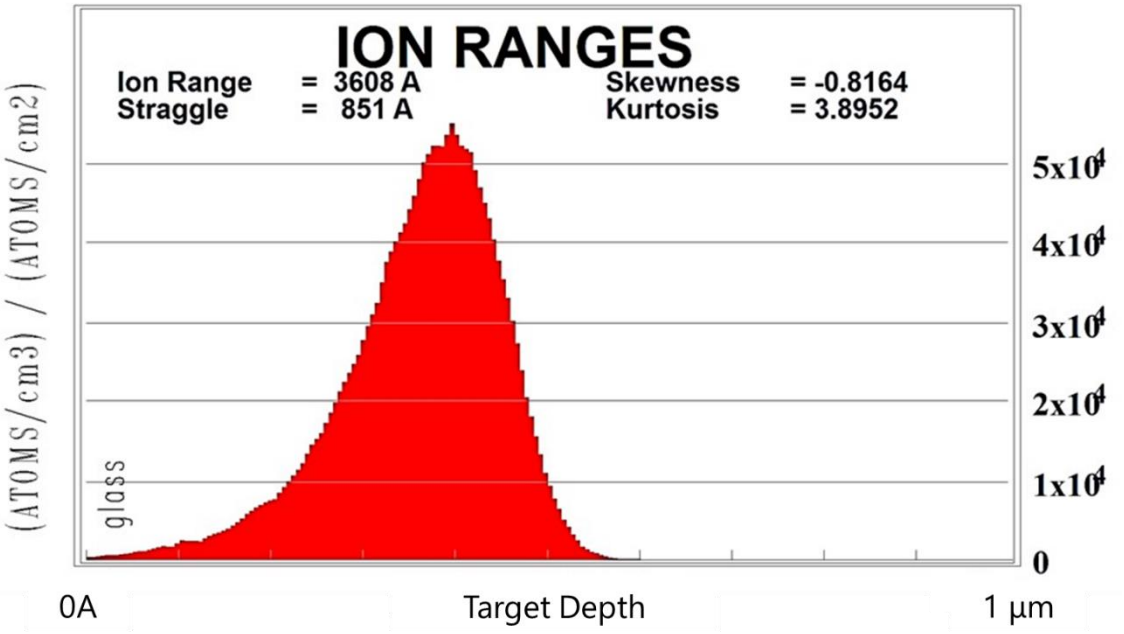

Figure 2.11. Results of TRIM simulation in quartz glass with accelerating voltage of 132 keV.

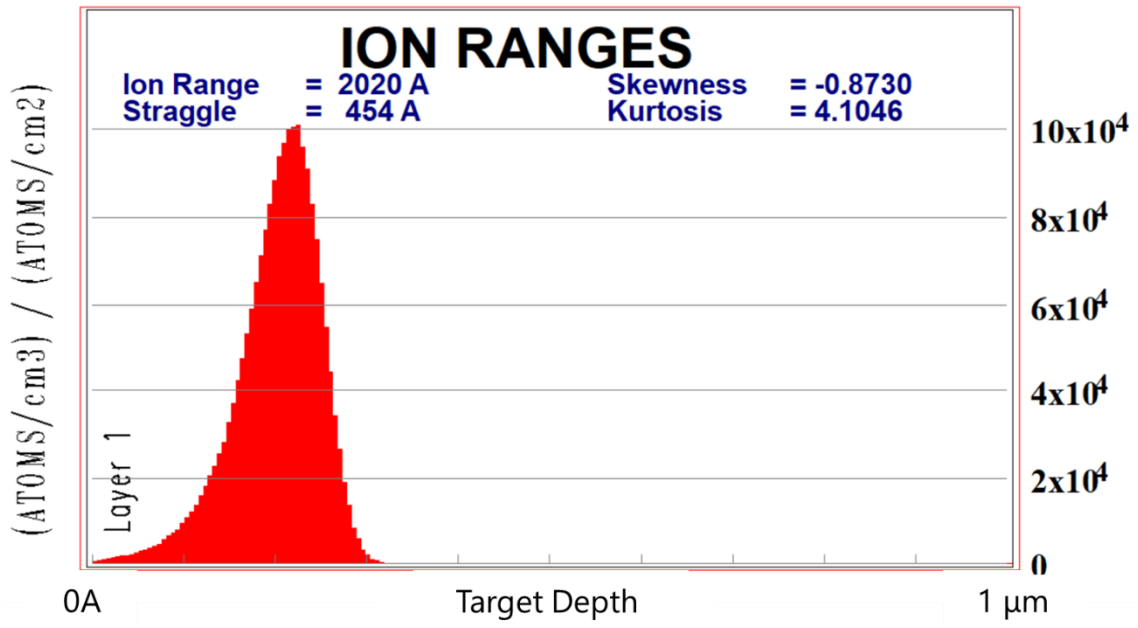

Figure 2.12. Results of TRIM simulation in MgO single crystal with accelerating voltage of 132 keV.

In contrast, it was difficult to determine the pit depths on the MgO single crystal plates using a confocal laser scanning microscope because the plates were more hydrated, and their surfaces had become rough (see Figure 2.13).

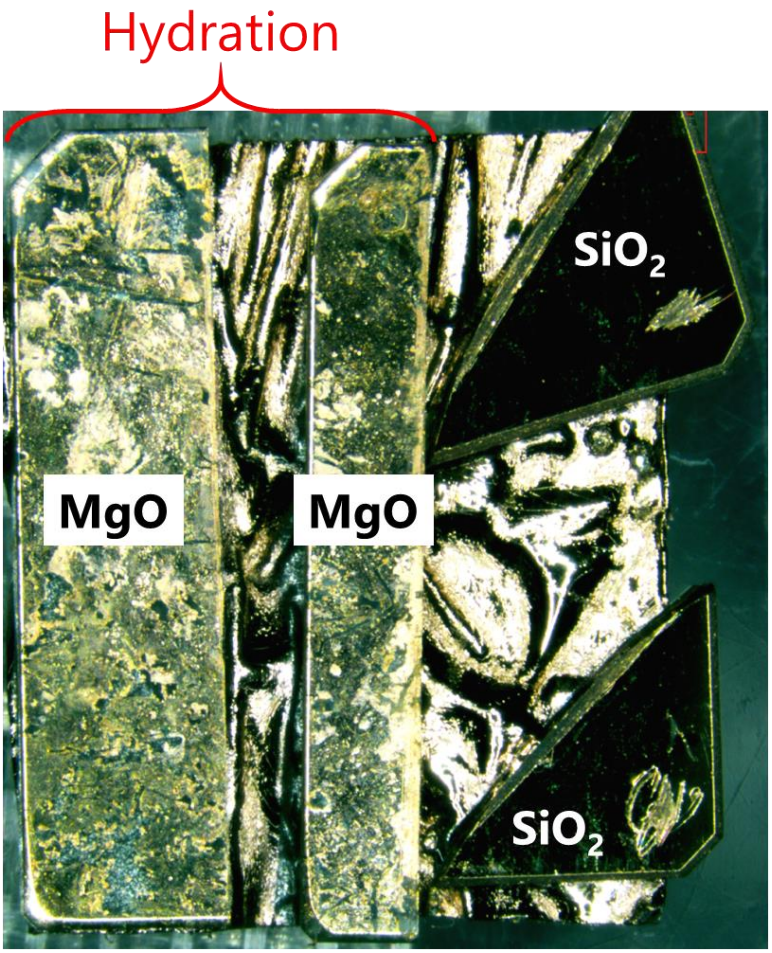

Figure 2.13. Hydration of $^{14}N^{+}$−implanted MgO single crystal plates.

2.9. High-resolution SIMS

Quantitative analysis of nitrogen in bridgmanite was conducted using a high-resolution SIMS (1280 HR2, CAMECA) installed at Centre de Recherches Pétrographiques et Géochimiques, France. The recovered samples were polished, and gold coating or carbon coating was performed. The primary ion beam was a 10 keV Cs^+ with a current of ~10 nA. For charge compensation, a normal-incidence electron gun was used during the analysis. The mass resolution (M/ΔM) was ≈ 13000, and the raster size was 10 μm × 10 μm. Samples were pre-sputtered with 5 μm × 5 μm raster for 180 s to minimize surface contamination. Spot analyses of negatively charged ions were conducted at different mass stations (Mass of 30, 31, and 32). For nitrogen abundance measurements, the $^{15}N^{16}O^-$ molecular ion was analyzed for 25 cycles. Count times for detecting $^{27}Al^-$, $^{30}Si^-$, $^{14}N^{16}O^-$, $^{15}N^{16}O^-$, and $^{16}O_2^-$ were 4 s, 4 s, 6 s, 20 s, and 4 s, respectively, and the total analysis time was approximately 30 min. Nitrogen concentrations were obtained from the secondary ion intensity ratio $^{15}N^{16}O^-/^{16}O_2^-$ for bridgmanite using a calibration line obtained from eight synthetic basaltic glasses with known nitrogen contents (Füri et al., 2018).

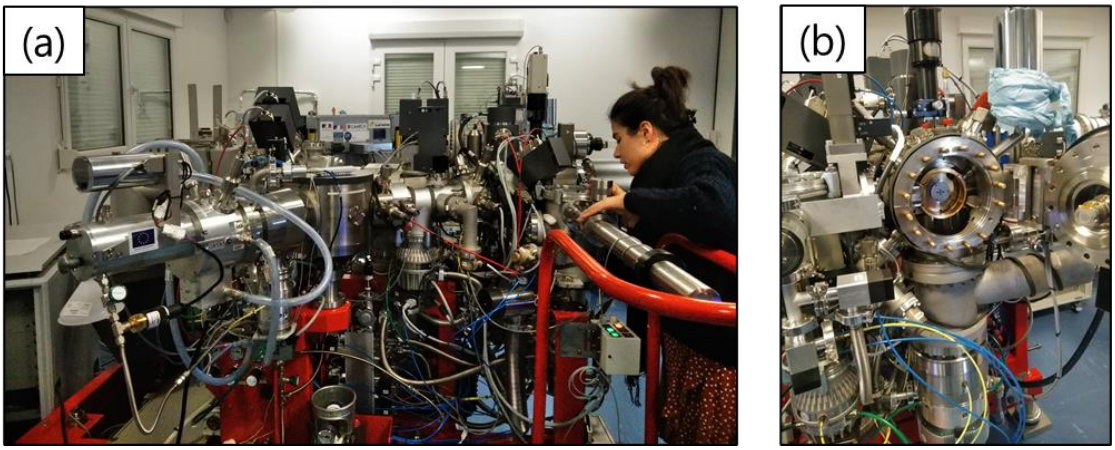

Figure 2.14. (a) High-resolution SIMS (1280 HR2) installed at Centre de Recherches Pétrographiques et Géochimiques, and (b) a sample chamber of the SIMS.

We succeeded in separating $^{15}N^{16}O^-$ ions and $^{29}SiH_2^-$ ions, as shown in Figure 2.15 and directly estimated the ion counts of $^{15}N^{16}O^-$ ions.

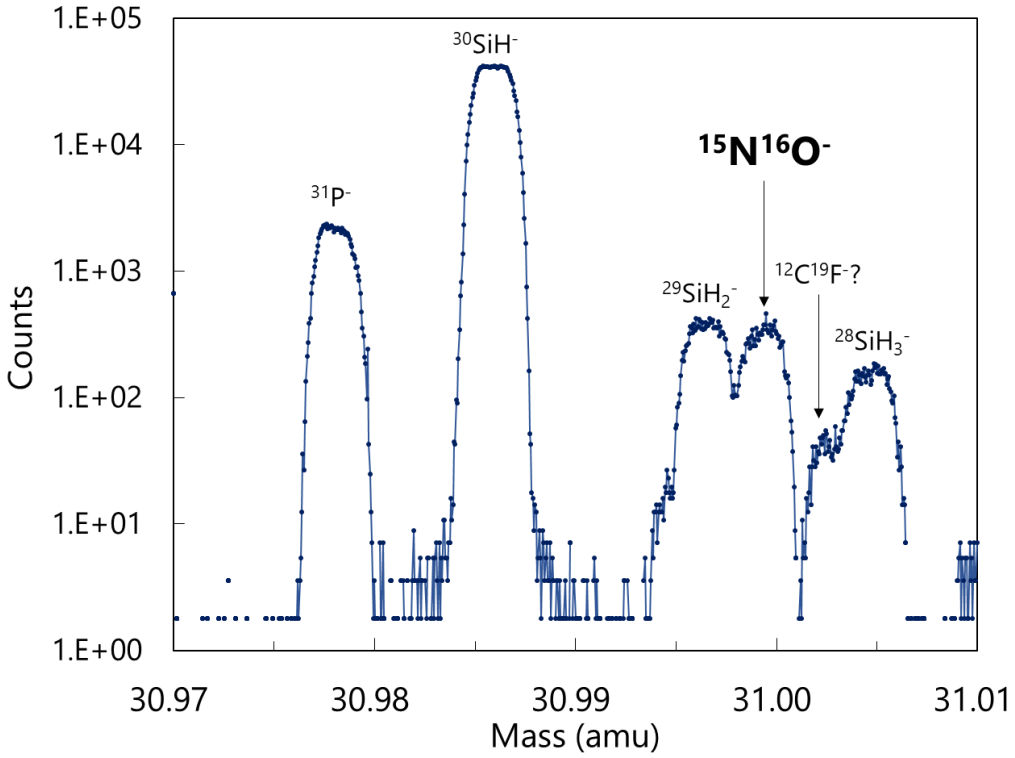

Figure 2.15. Mass spectrum obtained by high-resolution SIMS (1280 HR2).

3. Results

3.1. Calibration line for nitrogen analysis of stishovite by NanoSIMS analysis

I will show the depth profiles of ^{14}N in silica glass plates and make a calibration line for quantitative analysis of stishovite using NanoSIMS. The depth profile of ^{14}N in the standard samples was obtained by combining the SIMS analysis time with the depth at the bottom measured using a confocal laser scanning microscope. This estimation was based on the assumption that the depth of the post-bombardment crater is proportional to the analysis time. The volumes of the post-bombardment craters were estimated using a confocal laser scanning microscope.

3.1.1. Depth profiles of nitrogen in the quartz glass plate (doses of implanted nitrogen: 3.66×10^{15} atoms/cm^2)

Figure 3.1 shows depth profiles of ^{14}N in the quartz glass plate (doses of implanted nitrogen: 3.66×10^{15} atoms/cm^2). Four different spots on this quartz glass plate were analyzed using NanoSIMS. In estimating the average of $^{14}N^{16}O^-/^{28}Si^-$ ratio, baselines and averaging ranges were determined. The baselines were obtained by last counts of $^{14}N^{16}O^-$ and $^{28}Si^-$. The averaging area starts at 1/10 of the top of the counts of $^{14}N^{16}O^-$ and ends at a depth of around 0.5 μm to avoid crater edge effects. The obtained averages of $^{14}N^{16}O^-/^{28}Si^-$ ratio can be converted into $^{14}N^{16}O^-/^{30}Si^-$ based on the $^{30}Si^-/^{28}Si^-$ isotopic ratio (3.36×10^{-2}). As shown in Figure 3.1, the depths corresponding to the peak in $^{14}N^{16}O^-/^{28}Si^-$(= 0.32–0.39 μm) were in agreement with those calculated by TRIM (= 0.36 μm, see Figure 2.11).

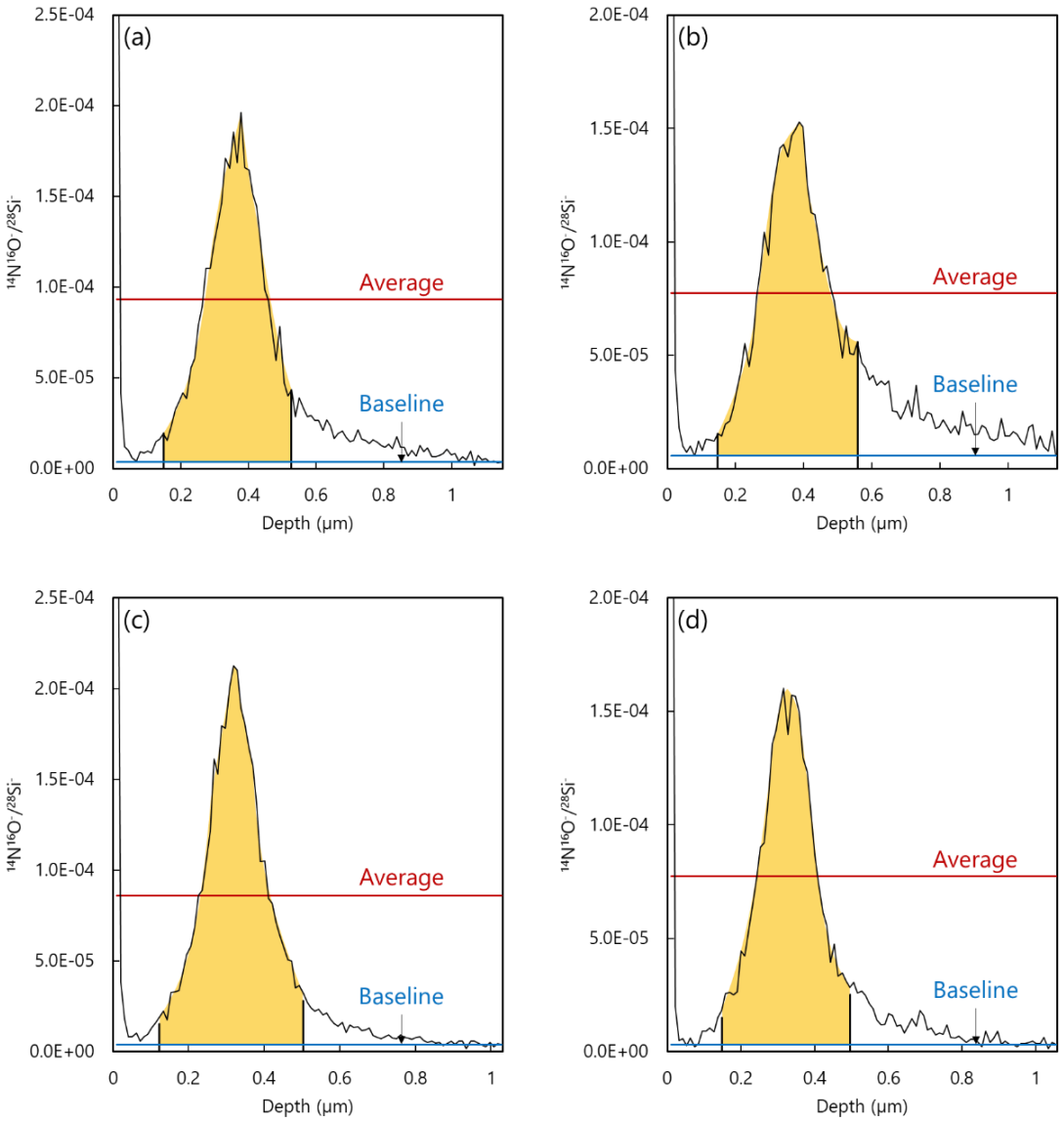

Figure 3.1. Depth profiles of $^{14}N^{16}O^-/^{28}Si^-$ in quartz glass plates (Dose: 3.66×10^{15} atoms/cm^2). Yellow sections are averaging area.

3.1.2. Depth profiles of nitrogen in the quartz glass plate (doses of implanted nitrogen: 2.44×10^{14} atoms/cm^2)

Figure 3.2 shows depth profiles of ^{14}N in quartz glass plates (doses of implanted nitrogen: 2.44×10^{14} atoms/cm^2). Six different spots on this quartz glass plate were analyzed using NanoSIMS. To estimate the average value of $^{14}N^{16}O^-/^{28}Si^-$ ratio, the averaging range was determined in the same way as for quartz glass plates whose doses was 3.66×10^{15} atoms/cm^2. The baselines were not determined because the counts of $^{14}N^{16}O^-$ reached zero.

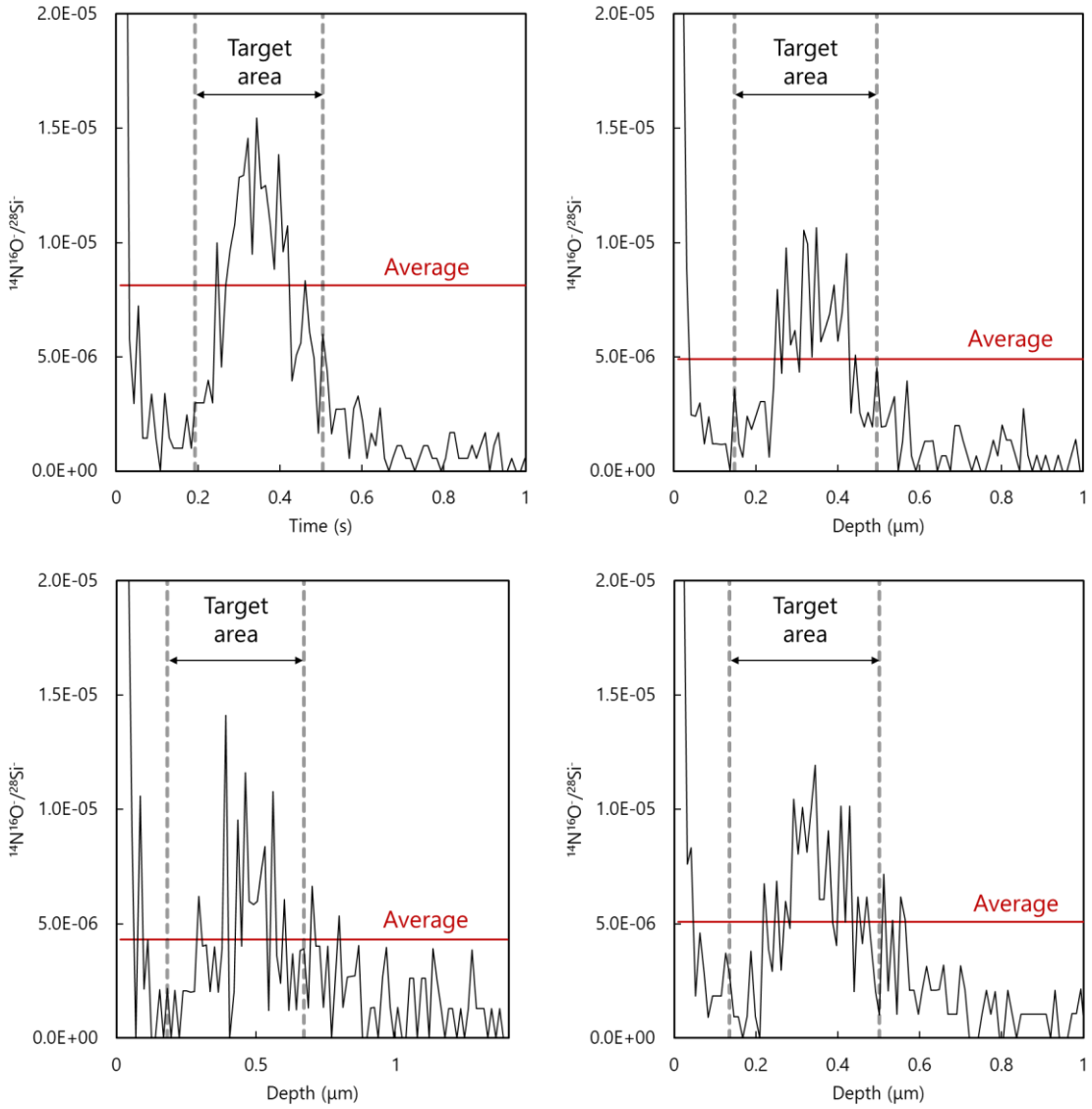

Figure 3.2. Depth profiles of nitrogen in quartz glass plates (Dose: 2.44×10^{14} atoms/cm^2).

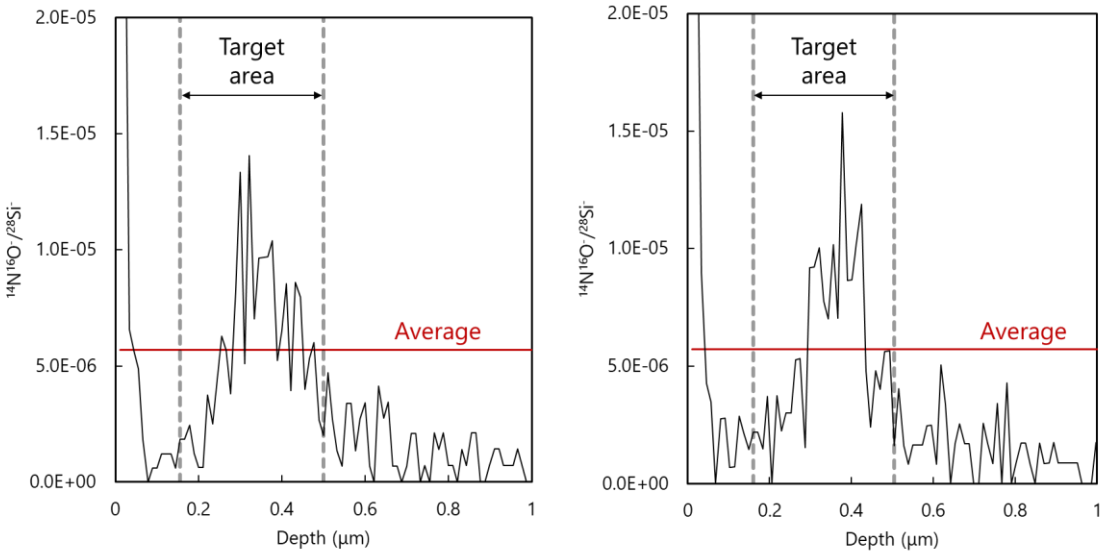

Figure 3.2 (Continued.)

3.1.3. Estimation of nitrogen concentration in the post-bombardment craters analyzed by SIMS

Table 3.1 shows the amount of ^{14}N implanted in quartz glasses, cross-sectional area of the post-bombardment craters at the depth of the TRIM peak, ^{14}N abundance in the post-bombardment craters, and volume of post-bombardment craters. ^{14}N abundance in craters was determined by multiplying the amount of ^{14}N implanted to quartz glasses and the cross-sectional area of craters at the TRIM peak depth (= 0.36 μm in this research, see Figure 2.12). The cross-sectional areas of craters at the depth of the TRIM peak were determined using the confocal laser scanning microscope. ^{14}N content in the crater was obtained from multiplying the amount of ^{14}N implanted to quartz glasses by the cross-sectional area of the post-bombardment craters at the depth of the TRIM peak, assuming that the crater shape is a cylinder. We can estimate ^{14}N concentration from ^{14}N abundance in craters (atoms) and volume of craters (cm^3).

Table 3.1. ^{14}N abundance in the post-bombardment craters and volume of the craters.

	Amount of ^{14}N implanted to quartz glasses ($atoms/cm^2$)	Cross-sectional area of craters at the depth of TRIM peak (cm^2)	^{14}N abundance in craters (atoms)	Volume of craters (cm^3)
(a)	3.66E+15	7.7E-07	2.8E+09	3.3E-11
(b)	3.66E+15	7.3E-07	2.7E+09	3.2E-11
(c)	3.66E+15	8.0E-07	2.9E+09	3.1E-11
(d)	3.66E+15	8.4E-07	3.1E+09	3.0E-11
(a)	2.44E+14	8.4E-07	2.0E+08	3.3E-11
(b)	2.44E+14	7.4E-07	1.8E+08	2.6E-11
(c)	2.44E+14	7.1E-07	1.7E+08	4.1E-11
(d)	2.44E+14	8.2E-07	2.0E+08	3.1E-11
(e)	2.44E+14	8.0E-07	1.9E+08	2.6E-11
(f)	2.44E+14	8.1E-07	2.0E+08	2.9E-11

3.1.4. Obtained calibration line for stishovite

By combining the obtained average values of $^{14}N^{16}O^{-}/^{30}Si^{-}$ ratio with the average values of ^{14}N content in silica glass plates, a calibration line for quantitative analysis of nitrogen in stishovite through NanoSIMS analysis was obtained. Figure 3.3 presents the calibration line for the nitrogen analysis in stishovite using NanoSIMS. The calibration line was obtained from the least-squares method using the origin and the results of the two $^{14}N^{+}$−implanted silica standards.

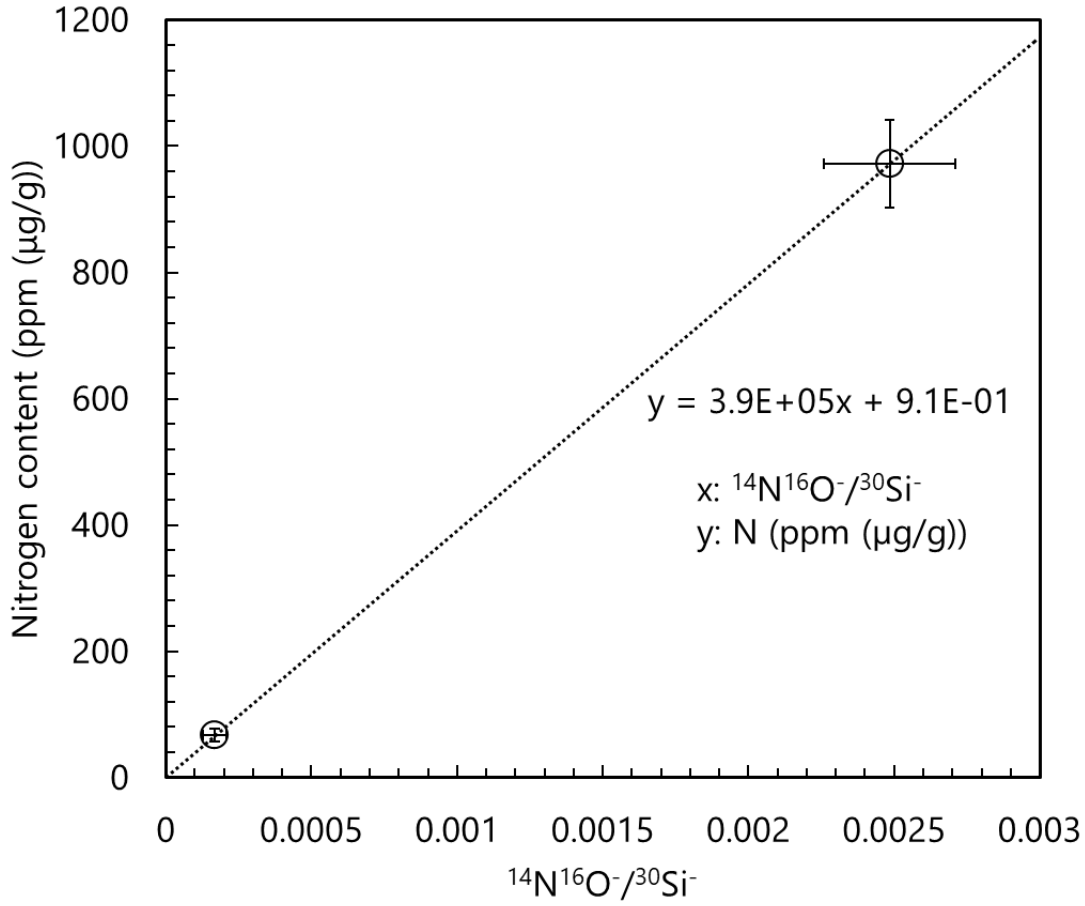

Figure 3.3. Calibration line for quantitative analysis of stishovite by NanoSIMS. The error indicates the standard deviation.

3.2. Depth profiles of nitrogen in MgO single crystal plates and calibration line for periclase in NanoSIMS analysis

I will show the depth profiles of ^{14}N in MgO single crystal plates and how to make the calibration line quantitative analysis of periclase by NanoSIMS. However, these standards were not analyzed on the day when periclase samples recovered from high-pressure experiments were analyzed. Therefore, errors in nitrogen solubilities in the periclase cannot be determined clearly. The depth at which the nitrogen count was maximum in the SIMS analysis was estimated by the TRIM simulation (see Figure 2.12). The depths of the post-bombardment craters of MgO single crystal plates after NanoSIMS were estimated from the TRIM simulation. In estimating the depth, I regarded that the depths of the peak in $^{14}N^{16}O^-/^{28}Si^-$ agreed with those calculated by TRIM. As shown in Figure 2.11 and Figure 3.1, the depth corresponding to the peak in $^{14}N^{16}O^-/^{28}Si^-$ can be estimated by TRIM.

3.2.1. Depth profiles of nitrogen in the MgO single crystal plate (doses of implanted nitrogen: 3.66×10^{15} atoms/cm^2)

Figure 3.4 shows depth profiles of ^{14}N in the MgO single crystal plate (doses of implanted nitrogen: 3.66×10^{15} atoms/cm^2). Seven different spots on this MgO single crystal were analyzed using NanoSIMS, and the averaging ranges of the $^{14}N^{16}O^-/^{18}O^-$ ratio were determined. The averaging area starts at 1/10 of the top of the counts of $^{14}N^{16}O^-$ and ends at 1/10 of the top of the counts of $^{14}N^{16}O^-$.

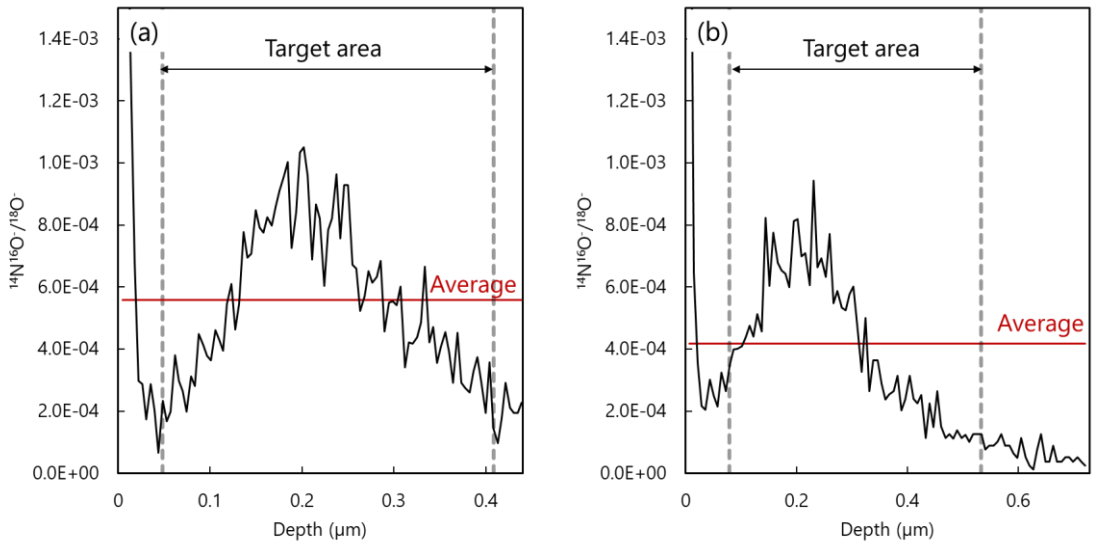

Figure 3.4. Depth profiles of nitrogen in MgO single crystal plates (Dose: 3.66×10^{15} atoms/cm^2).

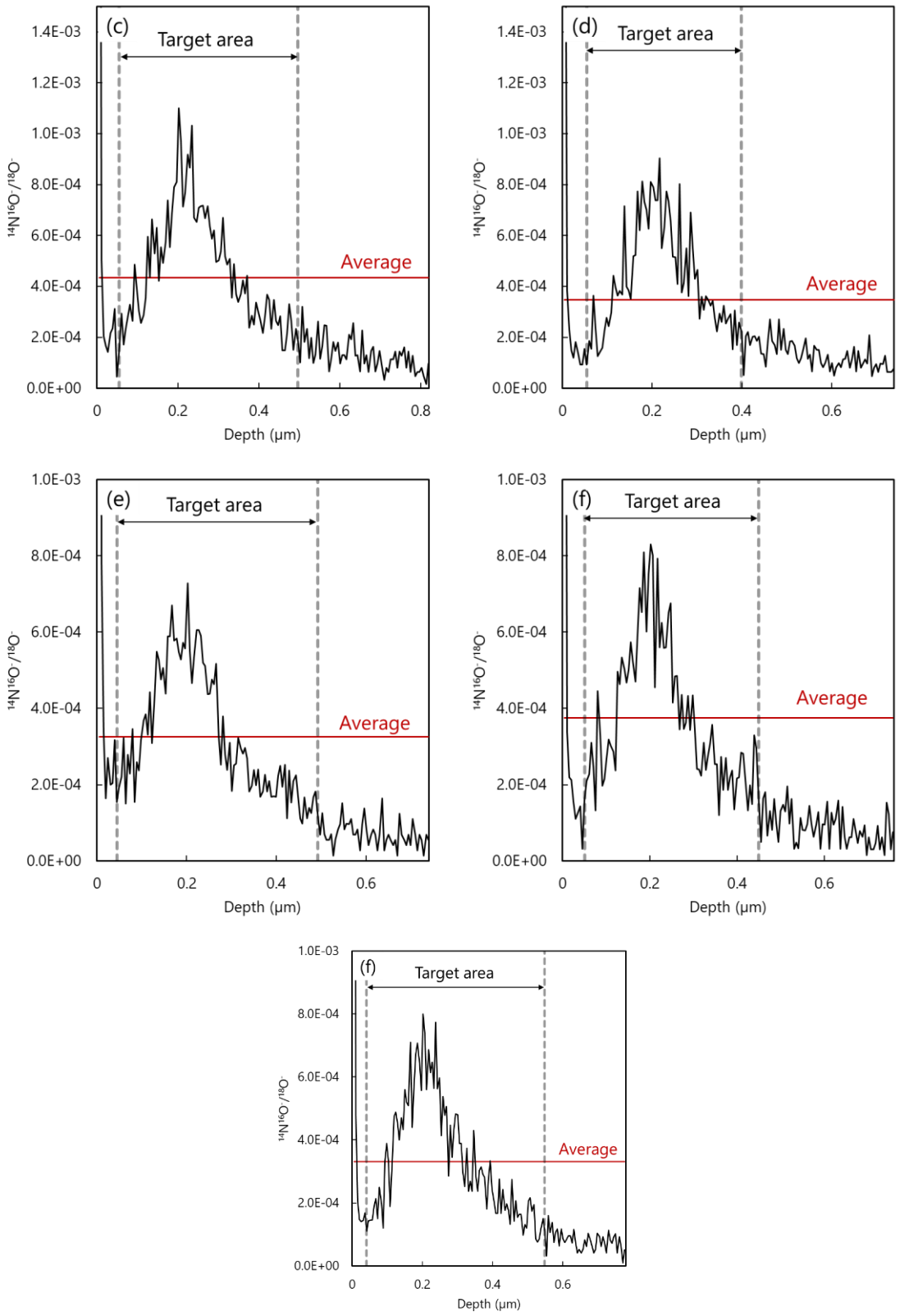

Figure 3.4 (Continued.)

3.2.2. Depth profiles of nitrogen in the MgO single crystal plate (doses of implanted nitrogen: 2.44×10^{14} atoms/cm^2)

Figure 3.5 shows depth profiles of ^{14}N in MgO single crystal plates (doses of implanted nitrogen: 2.44×10^{15} atoms/cm^2). Five different spots on this MgO single crystal were analyzed using NanoSIMS. In estimating the average of $^{14}N^{16}O^-/^{18}O^-$ ratio, averaging ranges were determined. The averaging area starts at 1/10 of the top of the counts of $^{14}N^{16}O^-$ and ends at 1/10 of the top of the counts of $^{14}N^{16}O^-$.

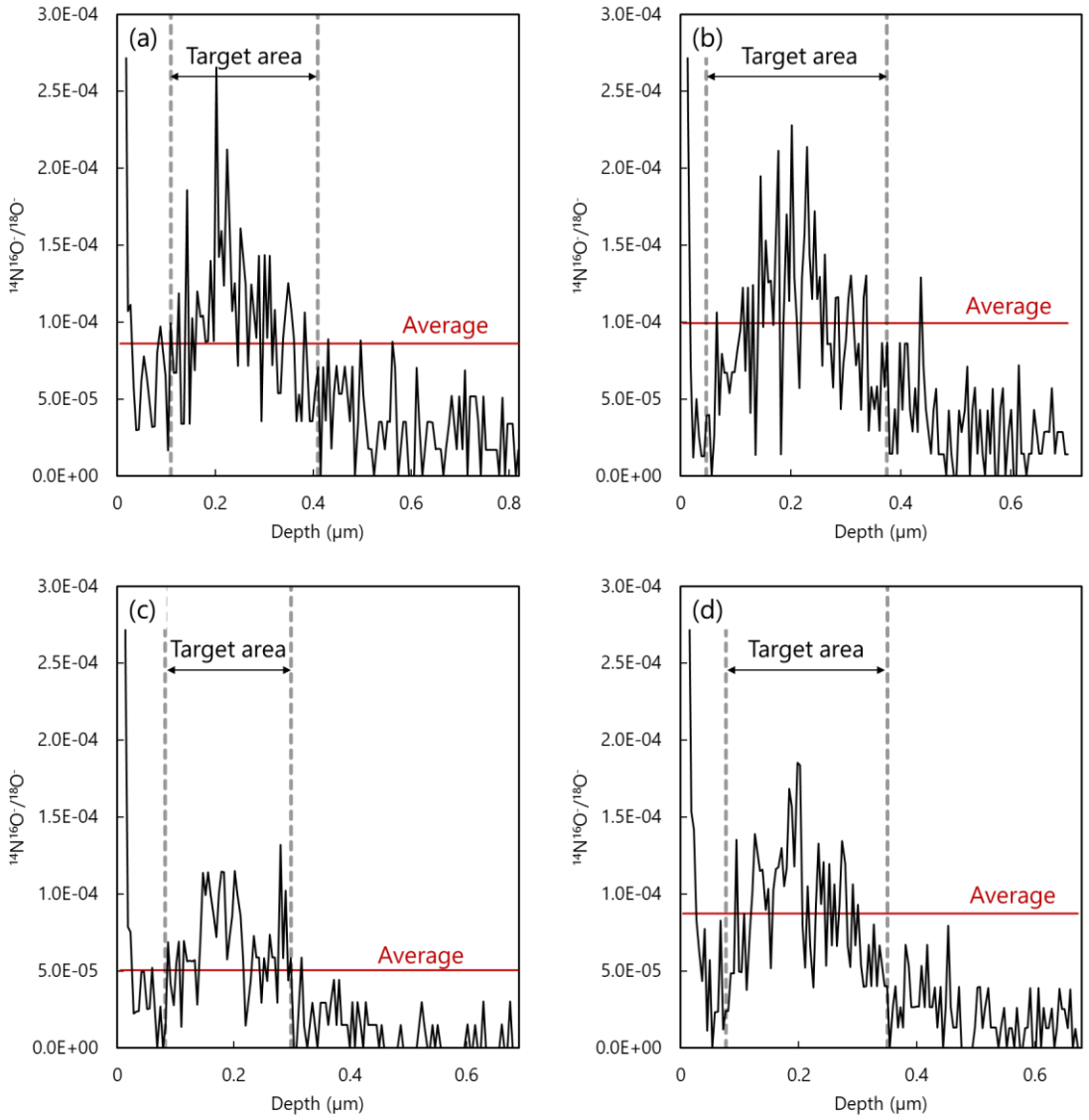

Figure 3.5. Depth profiles of nitrogen in MgO single crystal plates (Dose: 2.44×10^{14} atoms/cm^2).

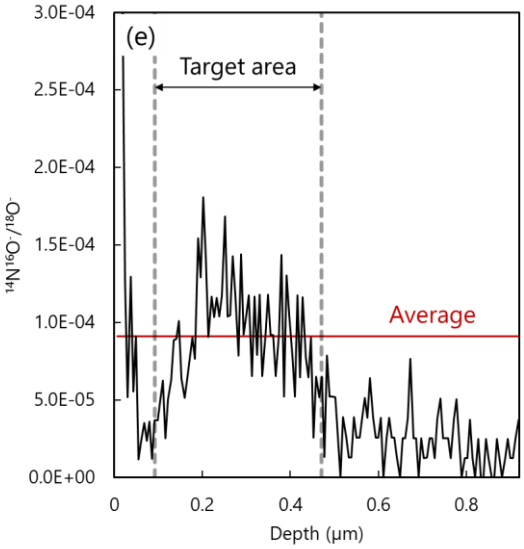

Figure 3.5 (Continued.)

3.2.3. Calibration line for periclase

Figure 3.6 shows the calibration line obtained for the nitrogen analysis in the periclase using NanoSIMS. The shapes of the craters were assumed to be cylindrical when estimating the volume of the post-bombardment craters of MgO single crystal plates. The calibration line was obtained from the least squares method as a straight line through the origin using the results of the two $^{14}N^{+}$–implanted MgO single crystal standards.

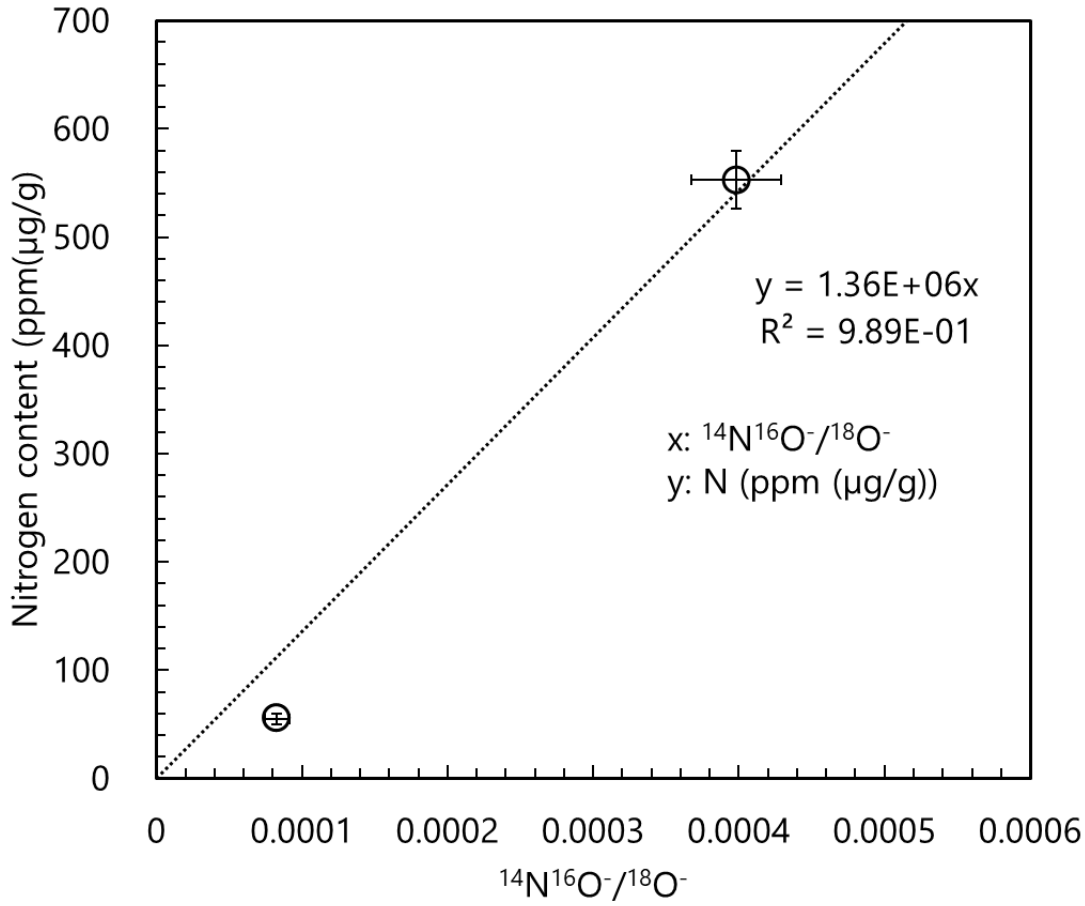

Figure 3.6. Calibration line for quantitative analysis of nitrogen in periclase by NanoSIMS.

3.3. Mg/Si ratio corrected by FE-EPMA

All recovered samples were analyzed using SEM-EDS, but the Mg/Si ratios of bridgmanite ($MgSiO_3$) samples deviated from the stoichiometric composition (Mg/Si = 1). Therefore, Mg/Si ratios of bridgmanite were corrected by FE-EPMA. I analyzed four representative bridgmanite samples; Brg2 in OS3083 (28 GPa, 1700 °C, Al-free system), Brg2 in OS3083 (28 GPa, 1700 °C, Al-free system), Brg1 in OT2427 (28 GPa, 1620 °C, Al-free system), and Brg6 in OT2651 (28 GPa, 1620 °C). Table 3.2 shows these representative bridgmanite compositions determined by FE-EPMA and comparison of Mg/Si ratios between FE-EPMA and SEM-EDS.

Table 3.2. Representative bridgmanite compositions redetermined by FE-EPMA and comparison of Mg/Si ratios between FE-EPMA and SEM-EDS.

	MgO	Al_2O_3	SiO_2	FeO	Total (wt.%)	Mg/Si (EPMA)	Mg/Si (SEM)
Brg2_OS3083	39.80	b. d.	62.88	0.48	103.20	0.94	1.17
Brg2_OS3083	38.21	b. d.	59.99	0.39	98.59	0.95	1.17
Brg2_OS3083	39.01	b. d.	61.21	0.46	100.68	0.95	1.17
Brg2_OS3083	38.86	b. d.	61.15	0.54	100.60	0.95	1.17
Brg2_OS3083	38.58	b. d.	60.76	0.26	99.64	0.95	1.17
Brg2_OS3083	37.80	b. d.	60.45	0.51	98.76	0.93	1.17
Brg2_OS3083	38.49	b. d.	60.69	0.43	99.61	0.95	1.17
Al-Brg2_OS3083	38.70	1.89	59.63	0.11	100.33	0.97	1.16
Al-Brg2_OS3083	37.77	1.49	58.61	0.05	97.92	0.96	1.16
Al-Brg2_OS3083	38.42	1.68	59.02	0.07	99.19	0.97	1.16
Al-Brg2_OS3083	38.56	1.77	59.64	0.09	100.07	0.96	1.16
Al-Brg2_OS3083	37.67	1.79	57.52	0.06	97.04	0.98	1.16
Al-Brg2_OS3083	36.64	5.53	57.12	0.37	99.66	0.96	1.16
Al-Brg2_OS3083	38.62	1.56	60.08	0.09	100.35	0.96	1.16
Al-Brg2_OS3083	37.06	5.36	57.09	0.49	100.00	0.97	1.16
Al-Brg2_OS3083	38.37	1.82	58.76	b. d.	98.95	0.97	1.16
Al-Brg2_OS3083	36.69	5.57	56.70	0.51	99.47	0.96	1.16
Al-Brg2_OS3083	37.84	1.16	59.00	0.04	98.04	0.96	1.16
Al-Brg2_OS3083	36.13	3.76	56.22	0.62	96.73	0.96	1.16
AlFe-Brg1_OT2427	33.31	5.46	52.70	7.89	99.36	0.94	1.09
AlFe-Brg1_OT2427	32.15	5.50	53.11	9.26	100.02	0.90	1.09
AlFe-Brg1_OT2427	32.39	5.67	52.04	8.76	98.86	0.93	1.09
AlFe-Brg1_OT2427	32.85	5.36	53.43	8.22	99.86	0.92	1.09
Brg6_OT2651	34.86	b. d.	59.26	4.57	98.69	0.88	1.11
Brg6_OT2651	34.29	b. d.	57.75	4.20	96.24	0.89	1.11
Brg6_OT2651	34.77	b. d.	58.23	4.44	97.51	0.89	1.11
Brg6_OT2651	35.10	b. d.	58.47	4.04	97.74	0.89	1.11
Brg6_OT2651	34.97	b. d.	59.01	3.93	97.96	0.88	1.11

*b. d.: Below detection limit of FE-EPMA.

As shown in Figure 3.7, I compared Mg/Si ratios of bridgmanite determined by FE-EPMA and those determined by SEM-EDS. Using this calibration line, chemical composition of bridgmanite was recalculated.

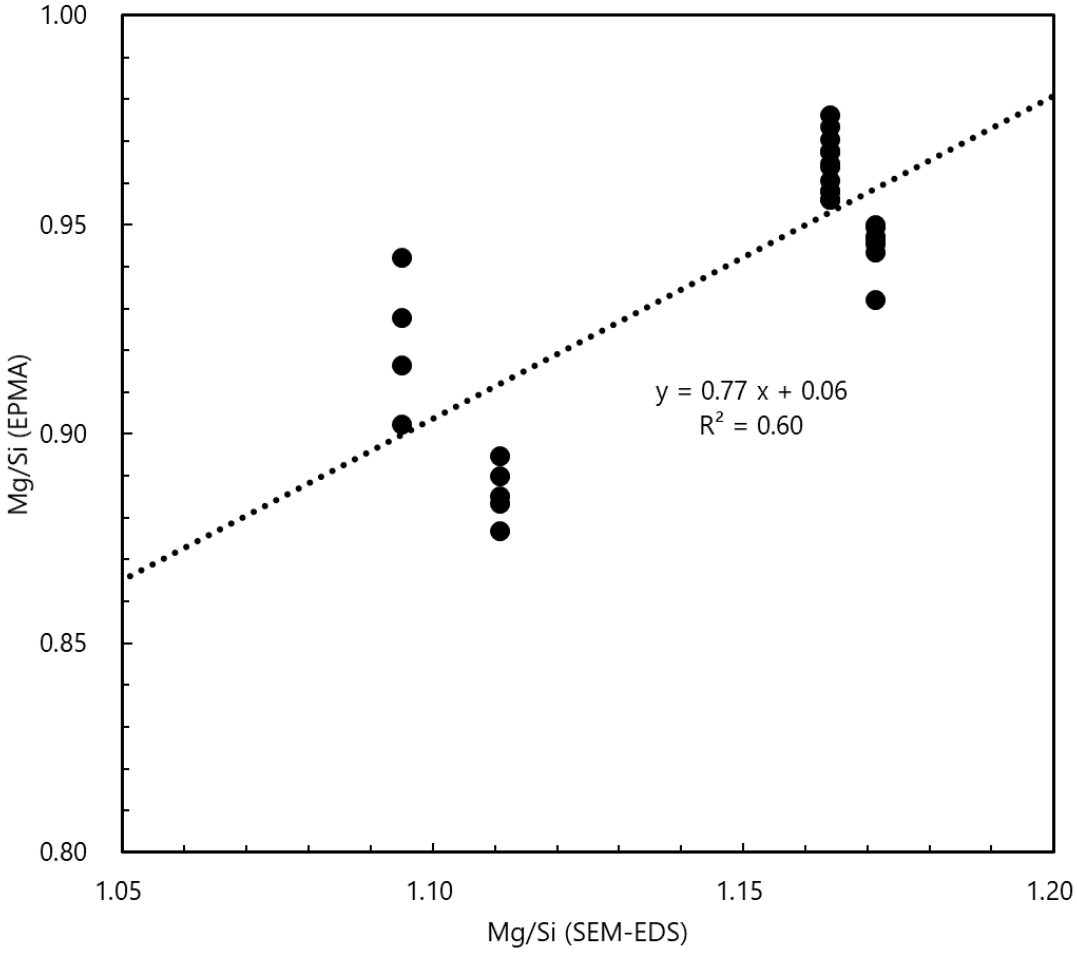

Figure 3.7. Calibration line for of the Mg/Si ratio of bridgmanite determined by SEM-EDS.

3.4. Details of samples recovered from high-pressure and high-temperature experiments

Table 3.3 lists experimental conditions and run products of high-pressure and high-temperature experiments using multi-anvil high-pressure apparatus. In all the run products, hydrous melt (now, quenched crystals) coexisted with crystals because ^{15}N–substituted ammonium nitrate ($^{15}NH_4{}^{15}NO_3$) released water under high temperature.

Table 3.3. Experimental conditions and run products in recovered samples.

Run.no	Starting materials*	Pressure (GPa)	Temperature (°C)	Run duration (min)	Run products
OT2259	a, b	28	1400	120	Brg, St, L
OT2258	a, b	28	1500	120	Brg, St, L
OT2293	a, b	28	1620	120	Brg, St, L
OS3083	a, b	28	1700	120	Brg, St, L
OT2427	b	28	1620	120	Brg**, St, L
OT2474	b	28	1500	120	Brg, St, L
OT2515	b	28	1400	120	Brg, St, L, Hydrous phase***
OT2649	c	28	1620	120	Brg, St, L
OT2650	d	28	1620	120	Brg****, St, L
OT2651	e	28	1620	120	Brg, St, L
OT2476	f	28	1700	120	Fe-bearing per, L
OT2516	f	28	1600	120	Per, L
OT2610	f	28	1500	120	Per, Fe-bearing per, L
OT2611	f	28	1400	120	Per, L

Brg: bridgmanite, St: stishovite, Per: periclase, L: liquid (hydrous melt, now quenched crystals).

*Detailed chemical compositions of starting materials are listed in Table. a: $MgSiO_3$, b: $MgSi_{0.9}Al_{0.1}H_{0.1}O_3$, c: $(Mg_{0.85}Fe_{0.15})SiO_3$, d: $(Mg_{0.9}Fe_{0.1})SiO_3$, e: $(Mg_{0.95}Fe_{0.05})SiO_3$, f: MgO

** The former bridgmanite was vitrified after the high *P-T* experiments.

***Minor Al-bearing hydrous phases co-existed.

****No peaks in Raman spectra but speculated to be Fe-bearing bridgmanite from the chemical composition.

Figure 3.8–Figure 3.18, Figure 3.20–Figure 3.22, and Figure 3.24–Figure 3.27 show backscattered electron (BSE) images of recovered cell assemblies and samples. Each outer gold capsule included an inner platinum capsule surrounded by Fe-FeO buffer. Run products from OT2258 (1500 °C), OT2259 (1400 °C), OT2293 (1620 °C), OS3083 (1700 °C), and OT2649 (1620 °C), whose starting material was equivalent to the chemical compositions of bridgmanite, mainly consisted of bridgmanite and hydrous melt, including minor stishovite. Single crystals of stishovite and bridgmanite, measured by SIMS, were larger than 40 μm. These grain sizes were sufficiently large to be analyzed using secondary ionization mass spectrometry (SIMS). The chemical composition of quenched hydrous melts in all recovered samples was MgO-rich (e.g., Si/Mg ratio = 0–0.25 in OS3083). Run products started from chemical compositions equivalent to periclase (for example, OT2516 (1600 °C) and OT2610 (1500 °C)) mainly consisted of periclase and hydrous melt. Nitrogen contents in stishovite and periclase were analyzed using NanoSIMS. Nitrogen contents in bridgmanite were analyzed using a high-resolution SIMS (1280 HR2, CAMECA). Details of nitrogen solubilities are listed in Tables Table 3.4. The nitrogen concentration ranges of stishovite, bridgmanite, and periclase were 40–400 ppm, 2–16 ppm, and 0.1–130 ppm, respectively.

In OT2258 (1500 °C), OT2259 (1400 °C), OT2293 (1620 °C), and OS3083 (1700 °C), two inner platinum capsules in a cell assembly contained an Al-free sample and an Al-bearing sample (Fig. Figure 3.8−Figure 3.15). I recovered Fe-free and Al-bearing bridgmanite samples from OS3083, OT2427, and OT2515, but some bridgmanite samples contained FeO with concentrations up to approximately 6.8 wt.% in Al-bearing samples (1400 °C (OT2258), 1500 °C (OT2259), and 1620 °C (OT2293, OT2427)). In OT2427 (1620 °C), OT2474 (1500 °C), and OT2515 (1400 °C), both inner platinum capsules contained Al-bearing samples. FeO contamination from the Fe-FeO buffer might result from gaps between platinum double capsules or iron diffusion through the capsule. The outer gold capsules and inner platinum capsules partially melted after the runs because of the coexistence of iron and water, but no Fe-FeO leaked out from the outer gold capsules. The coexistence of Fe and FeO after the run indicates that the oxygen fugacity conditions in OT2258, OT2259, OT2293, OS3083, OT2427, OT2474, and OT2515 corresponded to that of oxygen fugacity in the lower mantle. Therefore, it can be assumed that hydrogen was generated in the outer gold capsules and permeated through the inner platinum capsule. The hydrous melt in the inner platinum capsule is expected to contain $^{15}NH_3$ under a coexisting hydrogen environment in OT2258, OT2259, OT2293, OS3083, OT2427, OT2474, and OT2515. Analytical errors in NanoSIMS were estimated from the square root of $^{15}N^{16}O^-$ counts. I also monitored $^{14}N^{16}O^-$ in high-resolution SIMS analysis, but considering the natural abundance of ^{15}N, ^{15}N derived from atmospheric contamination is smaller than the analytical error.

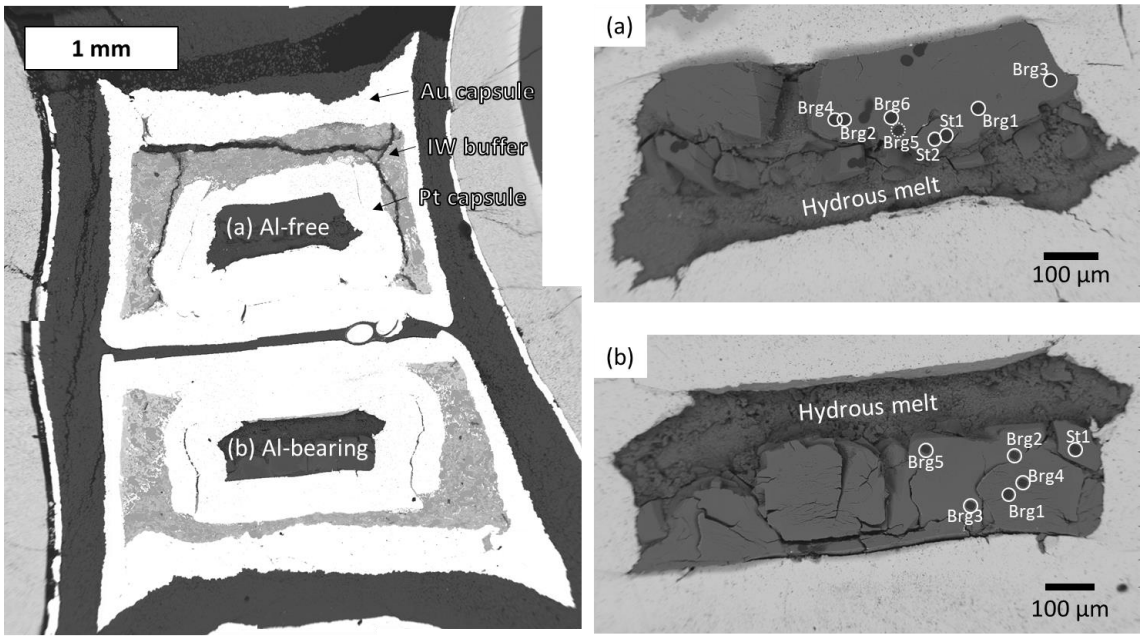

Figure 3.8. BSE images of recovered sample from 28 GPa, 1400 °C (OT2259). The left figure is a whole BSE image of the recovered sample. The right figures are the BSE images of the two samples obtained after NanoSIMS analysis; (a) Al-free system and (b) Al-bearing system. Circles correspond to the analysis points. St, stishovite; Brg, bridgmanite. The dotted circles are not discussed in this thesis because these analysis points are located in cracks or grain boundaries.

Table 3.4. Chemical composition of run products and nitrogen concentrations of stishovite in the Al-free system (OT2259).

	MgO	SiO_2	FeO	total (wt.%)	^{15}N (ppm)
St1	b. d.	100	b. d.	100	90.1(38)
St2	b. d.	100	b. d.	100	37.6(39)
Brg1	38.5	61.5	b. d.	100	—
Brg2	39.2	60.8	b. d.	100	—
Brg3	38.9	61.1	b. d.	100	—
Brg4	38.8	61.3	b. d.	100	—
Brg6	38.4	61.6	b. d.	100	—

*b. d.: Below detection limit of SEM-EDS.

Table 3.5. Chemical composition of run products and nitrogen concentrations of stishovite in the Al-bearing system (OT2259).

	MgO	Al_2O_3	SiO_2	FeO	total (wt.%)	^{15}N (ppm)
St1	b. d.	1.74	98.3	b. d.	100	23.1(18)
Brg1	38.1	b. d.	61.9	b. d.	100	—
Brg2	33.6	5.44	54.2	6.75	100	—
Brg3	37.1	1.77	61.2	b. d.	100	—
Brg4	34.1	4.83	55.1	5.98	100	—
Brg5	37.2	3.87	59.0	b. d.	100	—

*b. d.: Below detection limit of SEM-EDS.

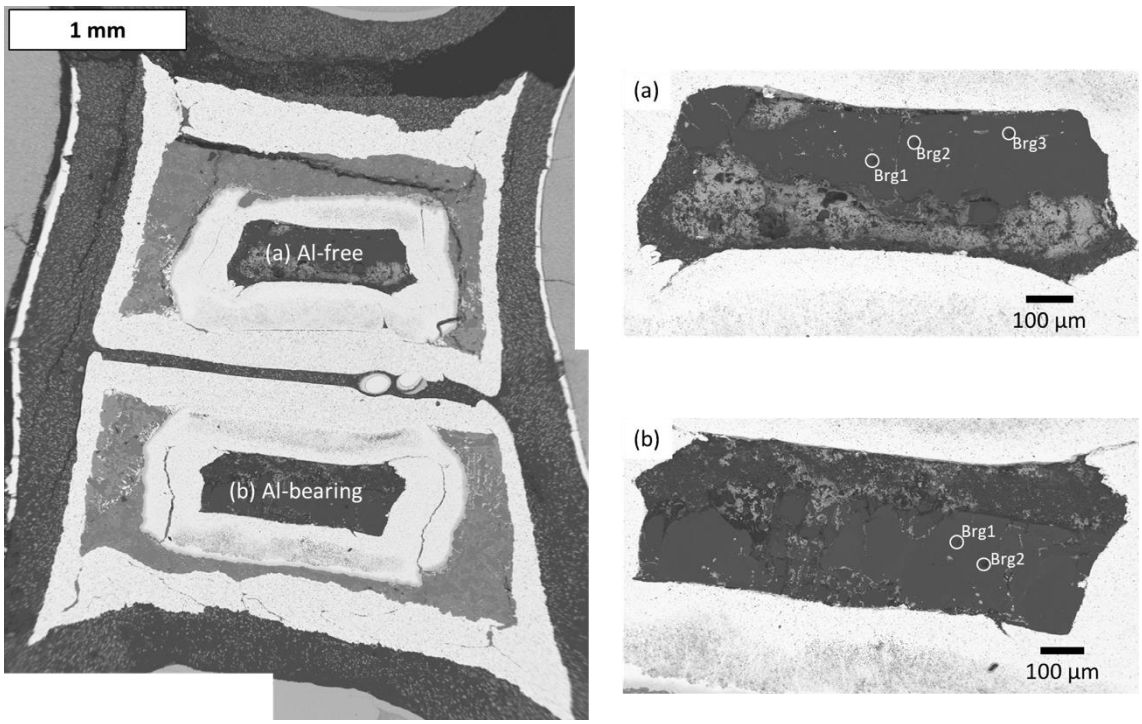

Figure 3.9. BSE images of recovered sample from 28 GPa, 1400 °C (OT2259). The left figure is a whole BSE image of the recovered sample. The right figures are the BSE images of two samples obtained by FE-SEM after high-resolution SIMS analysis; (a) Al-free system and (b) Al-bearing system. Circles correspond to analysis points. Brg, bridgmanite.

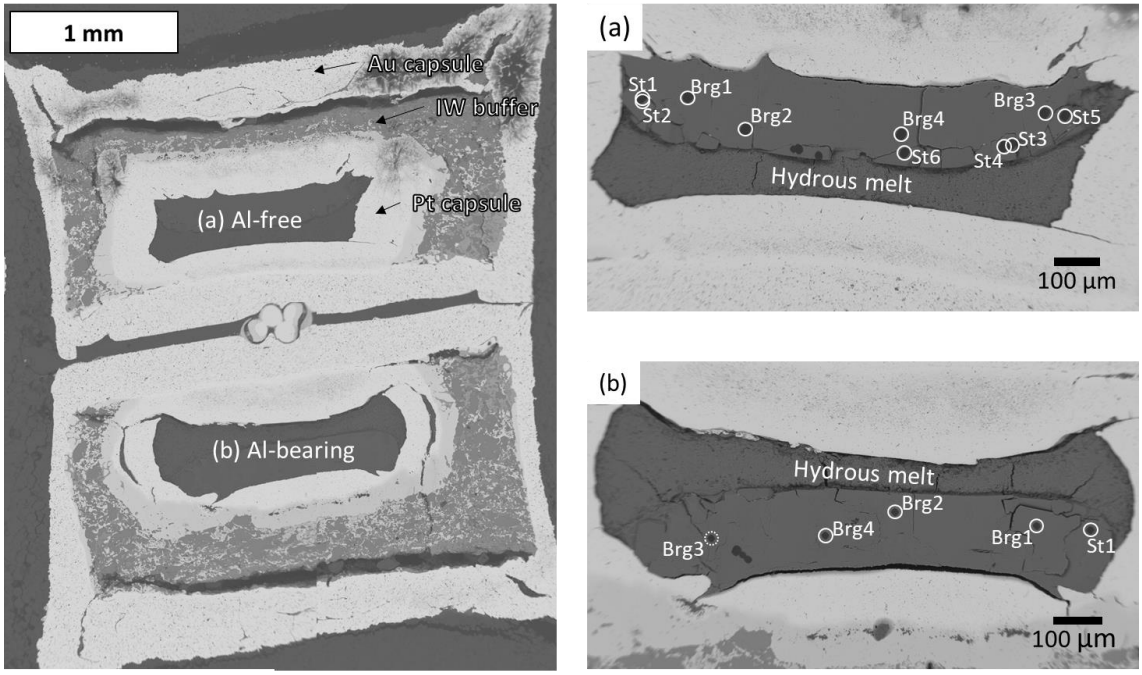

Figure 3.10. BSE images of recovered sample from 28 GPa, 1500 °C (OT2258). The left figure is a whole BSE image of the recovered sample. The right figures are the BSE images of two samples obtained by FE-SEM after NanoSIMS analysis; (a) Al-free system and (b) Al-bearing system. Circles correspond to analysis points. St, stishovite; Brg, bridgmanite. The dotted circles are not discussed in this paper because these analysis points are located in cracks or grain boundaries.

Table 3.6. Chemical composition of run products and nitrogen concentrations of stishovite in Al-free system (OT2258).

	MgO	SiO_2	FeO	total (wt.%)	^{15}N (ppm)
St1	0.78	99.2	b. d.	100	166(7)
St2	0.78	99.2	b. d.	100	160(6)
St3	b. d.	100	b. d.	100	99.0(52)
St4	b. d.	100	b. d.	100	102(5)
St5	b. d.	100	b. d.	100	153(5)
St6	b. d.	100	b. d.	100	149(6)
Brg1	39.1	60.9	b. d.	100	—
Brg2	38.3	61.7	b. d.	100	—
Brg3	38.6	61.4	b. d.	100	—
Brg4	38.9	61.1	b. d.	100	—

*b. d.: Below detection limit of SEM-EDS.

Table 3.7. Chemical composition of run products and nitrogen concentrations of stishovite in Al-bearing system (OT2258).

	MgO	Al_2O_3	SiO_2	FeO	total (wt.%)	^{15}N (ppm)
St1	b. d.	2.97	97	b. d.	100	40.3(23)
Brg1	35.7	3.15	57.5	3.68	100	—
Brg2	33.2	4.63	55.3	6.84	100	—
Brg4	37.9	2.07	60.1	b. d.	100	—

*b. d.: Below detection limit of SEM-EDS.

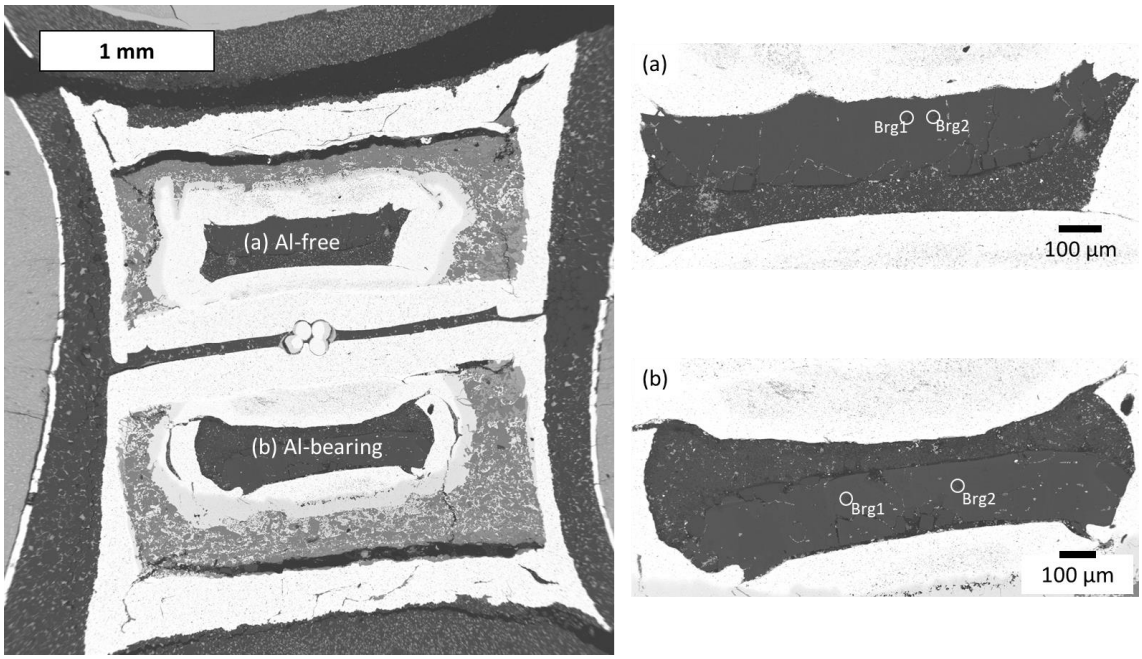

Figure 3.11. BSE images of recovered sample from 28 GPa, 1500 °C (OT2258). The left figure is a whole BSE image of the recovered sample. The right figures are the BSE images of the two samples obtained by FE-SEM after high-resolution SIMS analysis; (a) Al-free system and (b) Al-bearing system. Circles correspond to analysis points. Brg, bridgmanite.

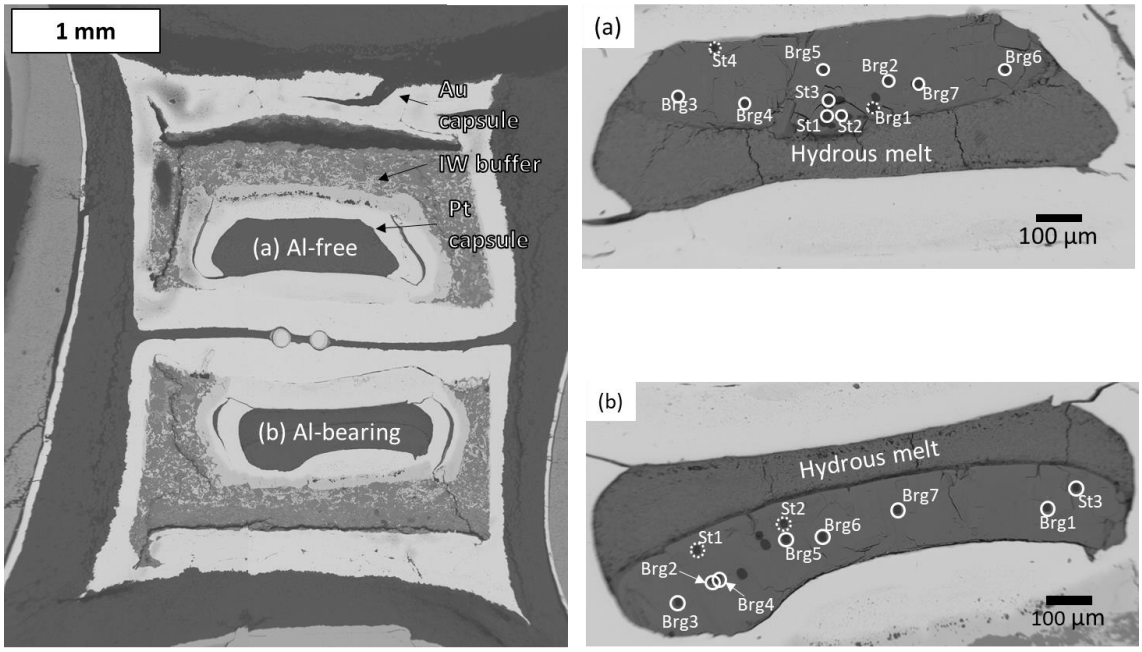

Figure 3.12. BSE images of recovered sample from 28 GPa, 1620 °C (OT2293). The left figure is a BSE image of the recovered sample. The right figures are the BSE images of two samples obtained by FE-SEM after NanoSIMS analysis; (a) Al-free system and (b) Al-bearing system. Circles correspond to analysis points. St, stishovite; Brg, bridgmanite. The dotted circles are not discussed in this paper because these analysis points are located in cracks or grain boundaries.

Table 3.8. Chemical composition of run products and nitrogen concentrations of stishovite in Al-free system (OT2293).

	MgO	SiO_2	FeO	total (wt.%)	^{15}N (ppm)
St1	b. d.	100	b. d.	100	157(6)
St2	b. d.	100	b. d.	100	120(2)
St3	b. d.	100	b. d.	100	63.7(37)
Brg2	39.3	60.8	b. d.	100	—
Brg3	36.5	63.5	b. d.	100	—
Brg4	36.4	63.6	b. d.	100	—
Brg5	36.9	63.1	b. d.	100	—
Brg6	39.2	60.8	b. d.	100	—
Brg7	38.8	61.2	b. d.	100	—

*b. d.: Below detection limit of SEM-EDS.

Table 3.9. Chemical composition of run products and nitrogen concentrations of stishovite in Al-bearing system (OT2293).

	MgO	Al_2O_3	SiO_2	FeO	total (wt.%)	^{15}N (ppm)
St3	b. d.	2.64	97.4	b. d.	100	131(4)
Brg1	34.6	3.21	57.8	4.4	100	—
Brg2	39.2	2.1	58.7	b. d.	100	—
Brg3	34.3	4.51	55.9	5.28	100	—
Brg4	37.7	2.9	58.1	1.32	100	—
Brg5	33.7	4.46	55.5	6.36	100	—
Brg6	38.0	1.57	58.7	1.66	100	—
Brg7	37.9	1.59	58.7	1.78	100	—

*b. d.: Below detection limit of SEM-EDS.

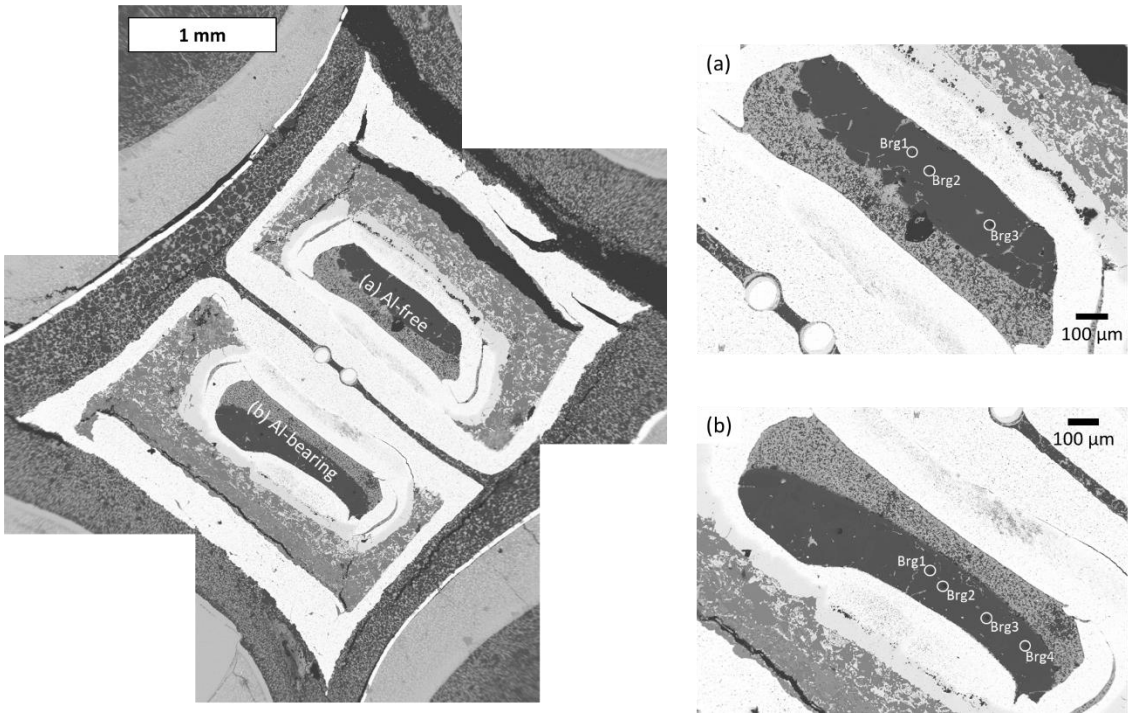

Figure 3.13. BSE images of recovered sample from 28 GPa, 1620 °C (OT2293). The left figure is a whole BSE image of the recovered sample. The right figures are the BSE images of the two samples obtained by FE-SEM after high-resolution SIMS analysis; (a) Al-free system and (b) Al-bearing system. Circles correspond to analysis points. Brg, bridgmanite.

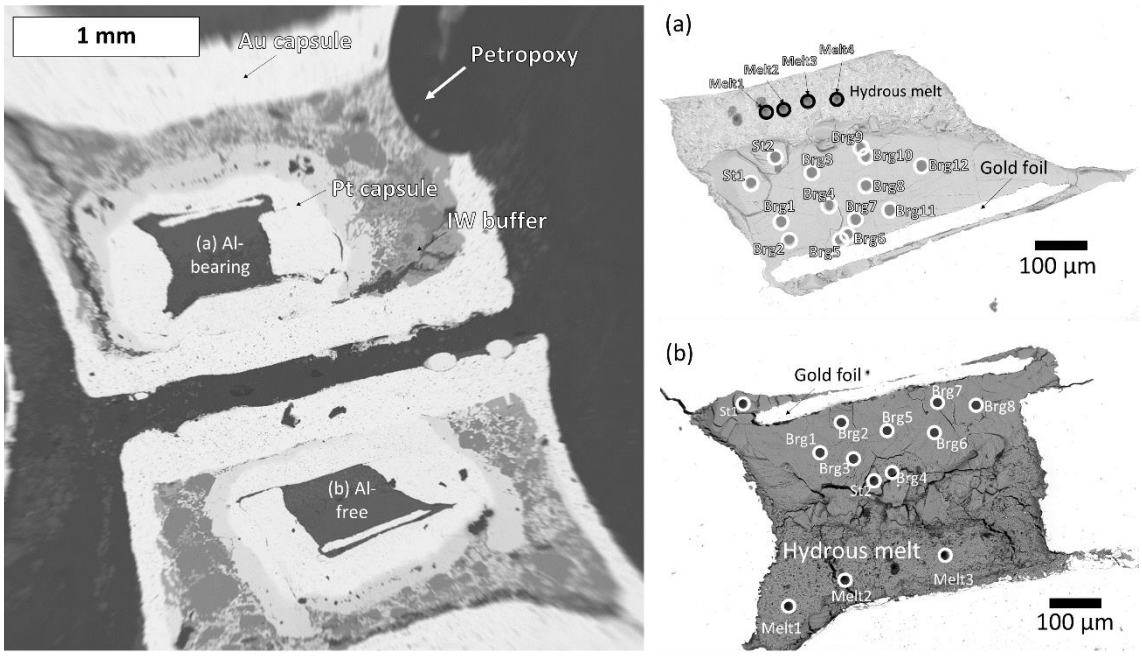

Figure 3.14. BSE images of recovered sample from 28 GPa, 1700 °C (OS3083). The left figure is a whole BSE image of recovered sample. The right figures are the BSE images of the two samples obtained by FE-SEM after NanoSIMS analysis; (a) Al-free system and (b) Al-bearing system. Circles correspond to analysis points. St, stishovite; Brg, bridgmanite.

Table 3.10. Chemical composition of run products and nitrogen concentrations of stishovite in Al-free system (OS3083).

	MgO	SiO_2	FeO	total (wt.%)	^{15}N (ppm)
St1	b. d.	100	b. d.	100	277(4)
St2	b. d.	100	b. d.	100	404(4)
Brg1	37.1	62.9	b. d.	100	—
Brg2	36.9	63.1	b. d.	100	—
Brg3	37.1	62.9	b. d.	100	—
Brg4	37.4	62.6	b. d.	100	—
Brg5	36.7	63.3	b. d.	100	—
Brg6	36.4	63.6	b. d.	100	—
Brg7	36.7	63.3	b. d.	100	—
Brg8	38.0	62.0	b. d.	100	—
Brg9	34.2	60.8	4.94	100	—
Brg10	—	—	—	—	—
Brg11	36.0	64.0	b. d.	100	—
Brg12	37.4	62.6	b. d.	100	—
melt1	30.4	17.3	52.3	100	—
melt2	42.1	9.2	48.7	100	—
melt3	25.7	15	59.3	100	—
melt4	35.3	38	26.7	100	—

*b. d.: Below detection limit of SEM-EDS.

Table 3.11. Chemical composition of run products and nitrogen concentrations of stishovite in Al-bearing system (OS3083).

	MgO	Al_2O_3	SiO_2	FeO	total (wt.%)	^{15}N (ppm)
St1	b. d.	3.71	96.3	b. d.	100	174(4)
St2	b. d.	3.22	96.8	b. d.	100	98.1(41)
Brg1	38.0	3.63	58.3	b. d.	100	—
Brg2	37.3	5.03	57.7	b. d.	100	—
Brg3	39.5	1.96	58.6	b. d.	100	—
Brg4	11.9	3.93	54.9	29.2	100	—
Brg5	39.1	1.57	59.4	b. d.	100	—
Brg6	36.8	4.89	58.4	b. d.	100	—
Brg7	—	—	—	—	—	—
Brg8	38.8	2.19	59.1	b. d.	100	—
melt1	69	10.9	16	4.18	100	—
melt2	95.1	4.86	0	b. d.	100	—
melt3	67.5	7.72	9.15	15.6	100	—

*b. d.: Below detection limit of SEM-EDS.

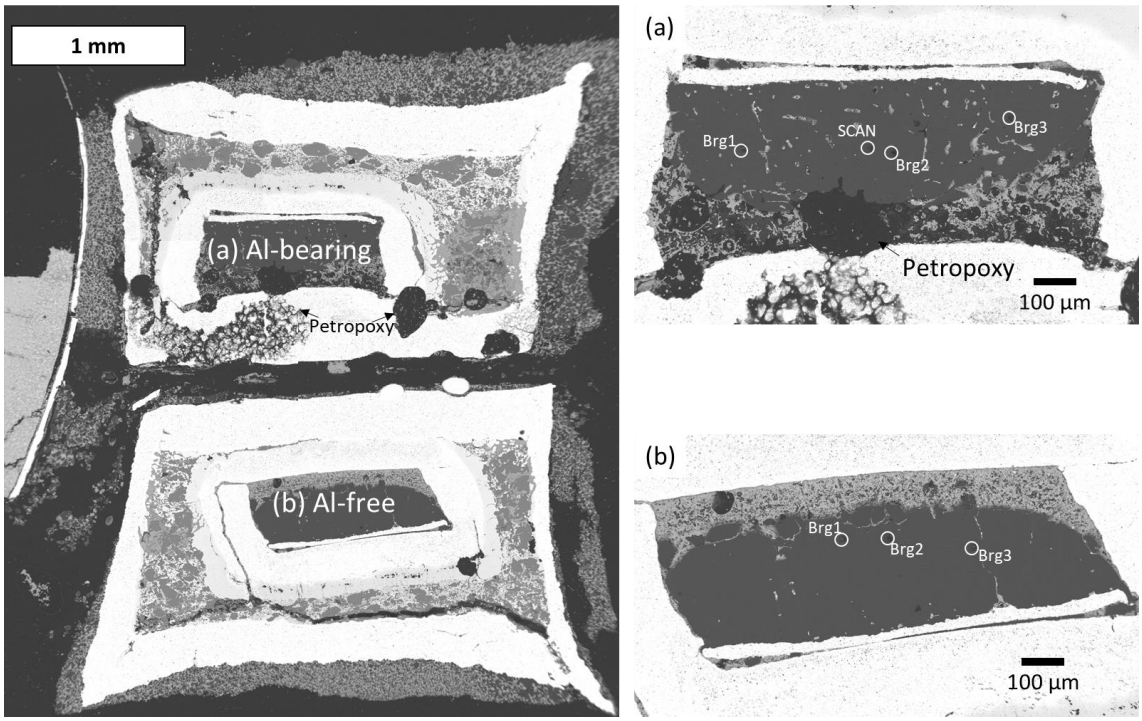

Figure 3.15. BSE images of recovered sample from 28 GPa, 1700 °C (OS3083). The left figure is a whole BSE image of the recovered sample. The right figures are the BSE images of the two samples obtained by FE-SEM after high-resolution SIMS analysis; (a) Al-free system and (b) Al-bearing system. Circles correspond to analysis points. Brg, bridgmanite.

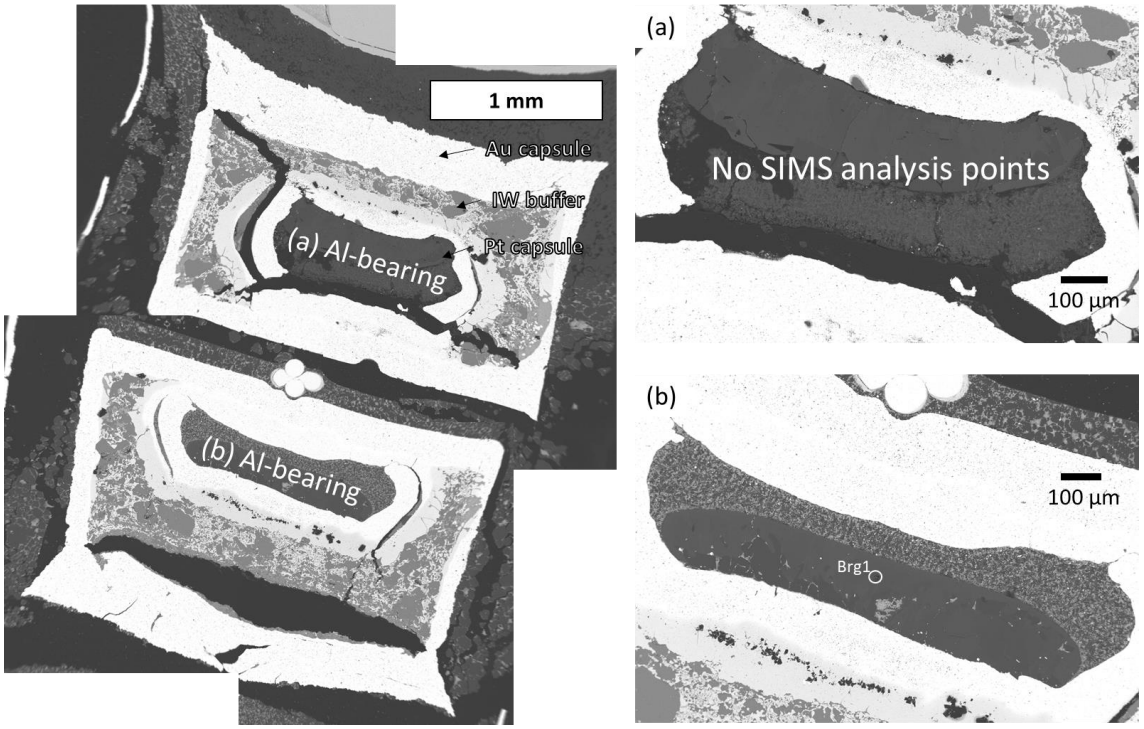

Figure 3.16. BSE images of recovered sample from 28 GPa, 1620 °C (OT2427). The left figure is a whole BSE image of the recovered sample. The right figures are the BSE images of the two samples obtained by FE-SEM after high-resolution SIMS analysis; both (a) and (b) are Al-bearing system. Circles correspond to analysis points. Brg, bridgmanite.

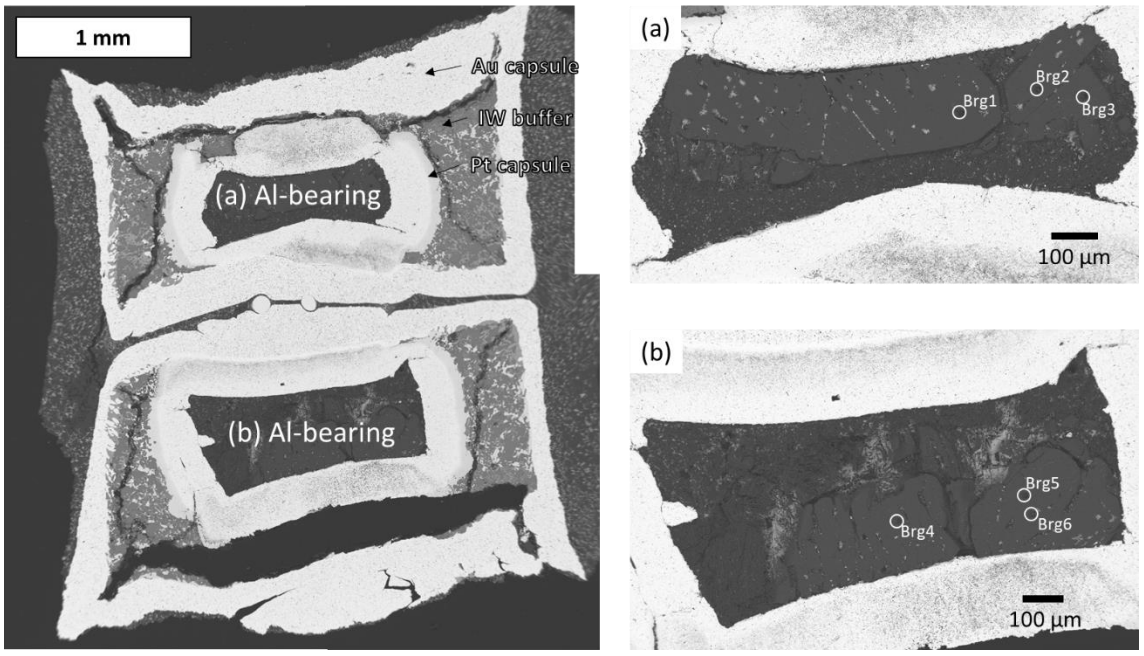

Figure 3.17. BSE images of recovered sample from 28 GPa, 1500 °C (OT2474). The left figure is a whole BSE image of the recovered sample. The right figures are the BSE images of the two samples obtained by FE-SEM after high-resolution SIMS analysis; both (a) and (b) are Al-bearing system. Circles correspond to analysis points. Brg, bridgmanite.

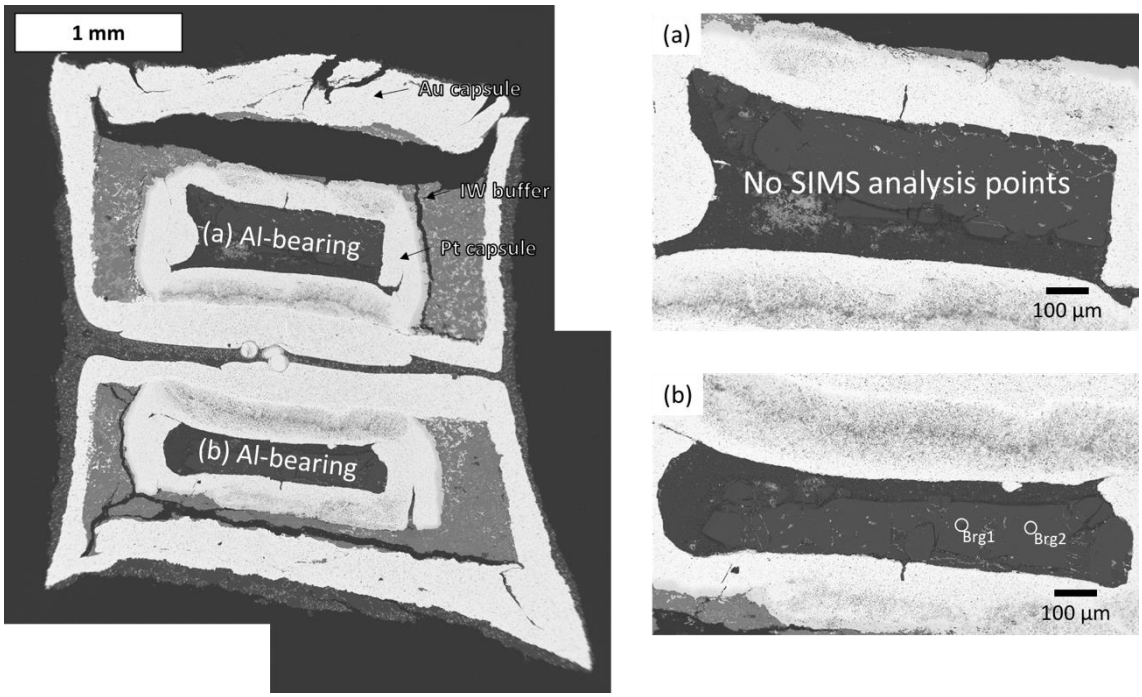

Figure 3.18. BSE images of recovered sample from 28 GPa, 1400 °C (OT2515). The left figure is a whole BSE image of the recovered sample. The right figures are the BSE images of the two samples obtained by FE-SEM after high-resolution SIMS analysis; both (a) and (b) are Al-bearing system. Circles correspond to analysis points. Brg, bridgmanite.

In OT2649 (the starting material: $(Mg_{0.85}Fe_{0.15})SiO_3$), OT2650 (the starting material: $(Mg_{0.9}Fe_{0.1})SiO_3$), and OT2651(the starting material: $(Mg_{0.95}Fe_{0.05})SiO_3$), both inner platinum capsules in a cell assembly contained Fe-bearing starting materials (see Table 2.1). In OT2650 and OT2651, the recovered samples were found to be contaminated with iron originating from the Fe-FeO buffer; Fe contents in Fe-bearing bridgmanite were higher than those in the starting materials. In OT2650 and OT2651, magnesiowüstite formed by excessive iron contamination from the Fe-FeO buffer was found. FeO contamination from the Fe-FeO buffer might result from gaps between platinum double capsules or iron diffusion through the capsule. The outer gold capsules and inner platinum capsules partially melted after the runs because of the coexistence of iron and water, and Fe-FeO leaked out from the gold capsules. Therefore, the redox states of OT2649, OT2650, and OT2651 did not necessarily simulate lower mantle oxygen fugacity. Later EDS analysis showed that pure metallic iron (Fe) remained and that FeO contained no Mg in the Fe-FeO buffer after the run, except for OT2650.

In Figure 3.19, stishovite is located next to Brg5, but the nitrogen solubilities in Brg5-7 were similar. The presence of stishovite containing high nitrogen concentrations adjacent to the bridgmanite did not affect the SIMS analysis of bridgmanite. I also monitored $^{14}N^{16}O^-$, but considering the natural abundance of ^{15}N, the concentration of ^{15}N originating from atmospheric contamination is smaller than the analytical errors and negligible.

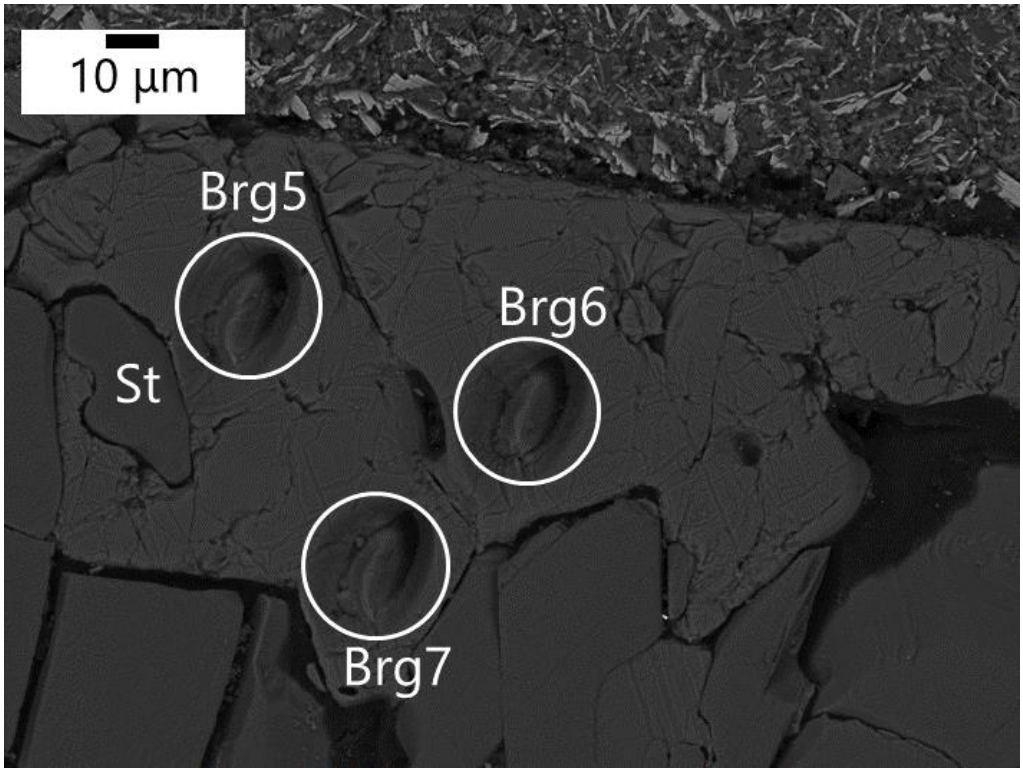

Figure 3.19. A stishovite grain of the same size as the diameter of the primary beam of high-resolution SIMS in OT2650.

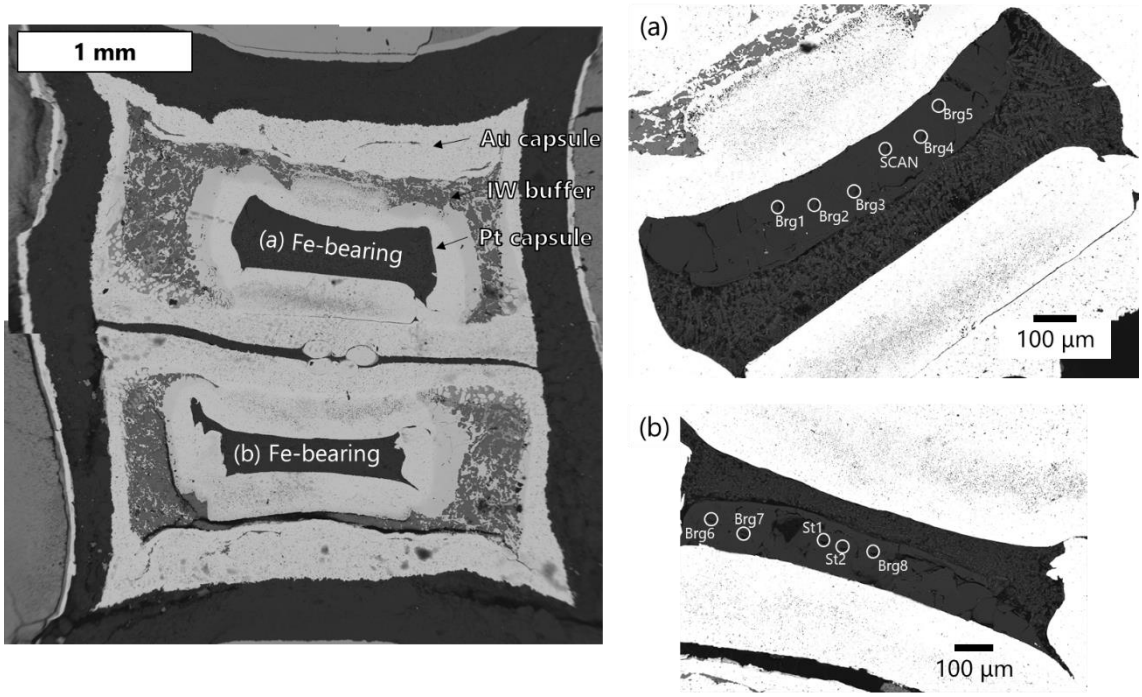

Figure 3.20. BSE images of recovered sample from 28 GPa, 1620 °C (OT2649). The left figure is a whole BSE image of the recovered sample before high-resolution SIMS analysis. The right figures are the BSE images of the two samples obtained by FE-SEM after high-resolution SIMS analysis; both (a) and (b) are Fe-bearing system. Circles correspond to analysis points. St, stishovite; Brg, bridgmanite.

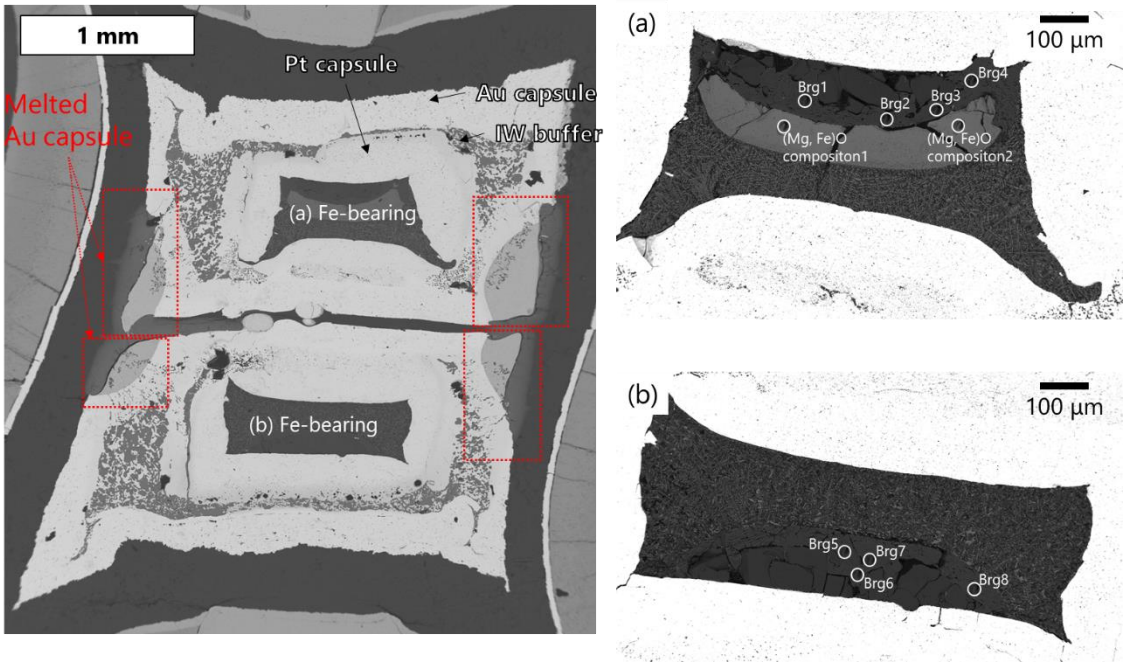

Figure 3.21. BSE images of recovered sample from 28 GPa, 1620 °C (OT2650). The left figure is a BSE image of the recovered sample before high-resolution SIMS analysis. Right figures are the BSE images of the two samples obtained by FE-SEM after high-resolution SIMS analysis; both (a) and (b) are Fe-bearing system. Circles correspond to analysis points. Brg, bridgmanite.

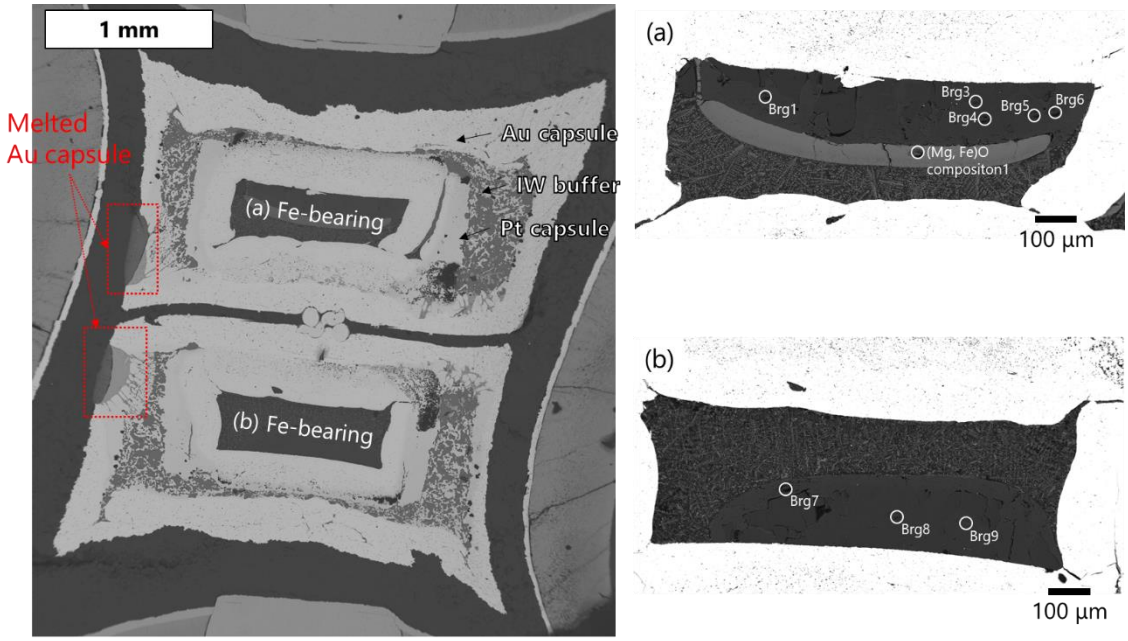

Figure 3.22. BSE images of recovered sample from 28 GPa, 1620 °C (OT2651). The left figure is a whole BSE image of the recovered sample before high-resolution SIMS analysis. The right figures are the BSE images of the two samples obtained by FE-SEM after high-resolution SIMS analysis; both (a) and (b) are Fe-bearing system. Circles correspond to analysis points. Brg, bridgmanite.

In OT2476 (1700 °C), OT2516 (1600 °C), OT2610 (1500 °C), and OT2611 (1400 °C), both the inner platinum capsules contained MgO powder. In OT2476, and OT2610 for estimating nitrogen solubilities in periclase, FeO contamination was found in the samples. FeO contamination from the Fe-FeO buffer might result from gaps between platinum double capsules or iron diffusion through the capsule. The outer gold capsules and inner platinum capsules partially melted after the runs because of the coexistence of iron and water, but no Fe-FeO leaked out from the gold capsules except for OT2476. For this reason, the redox state of OT2476 did not necessarily reproduce the lower mantle oxygen fugacity. EDS analysis showed that pure metallic iron (Fe) remained and that FeO contained no Mg in the Fe-FeO buffer after the run, except for OT2476. The coexistence of Fe and FeO after the run indicates that the oxygen fugacity condition in OT2516, OT2610, and OT2611 corresponded to that of oxygen fugacity in the lower mantle. Therefore, hydrogen can be assumed to have been generated in the outer gold capsules, permeating the inner platinum capsule. The hydrous melt in the inner platinum capsule is expected to contain $^{15}NH_3$ under a hydrogen coexisting environment in OT2516, OT2610, and OT2611. Analytical errors in NanoSIMS were estimated from the square root of $^{15}N^{16}O^-$ counts.

In OT2611, nitrogen solubilities in the periclase cannot be determined because the mass of $^{15}N^{16}O^-$ at 30.99502352 u interferes with the masses of $^{12}C^{19}F^-$ at 30.99840322 u. The overlap between these masses makes it difficult to separate the mass spectra using NanoSIMS, whose mass resolution is not sufficiently high for this purpose.

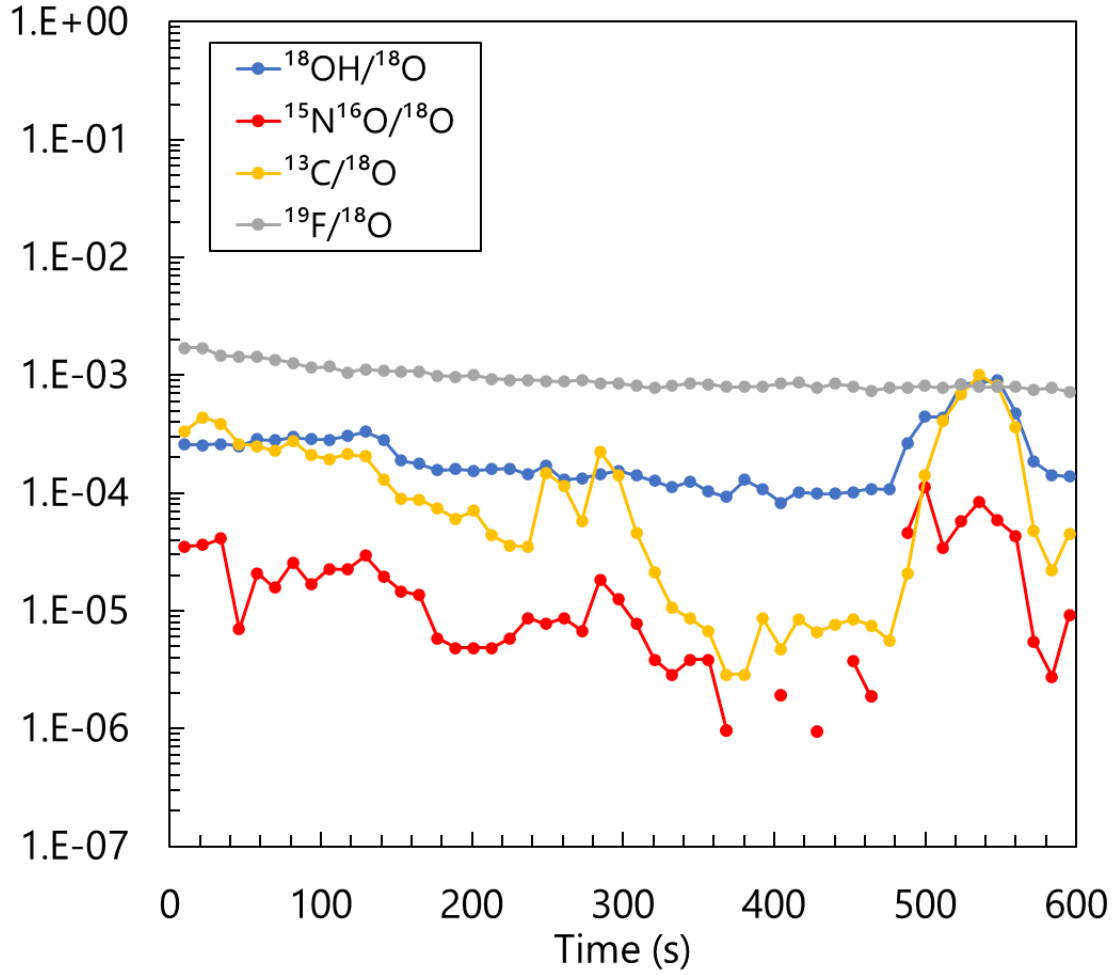

Figure 3.23. Ion counts of Per19 in OT2611 obtained from NanoSIMS.

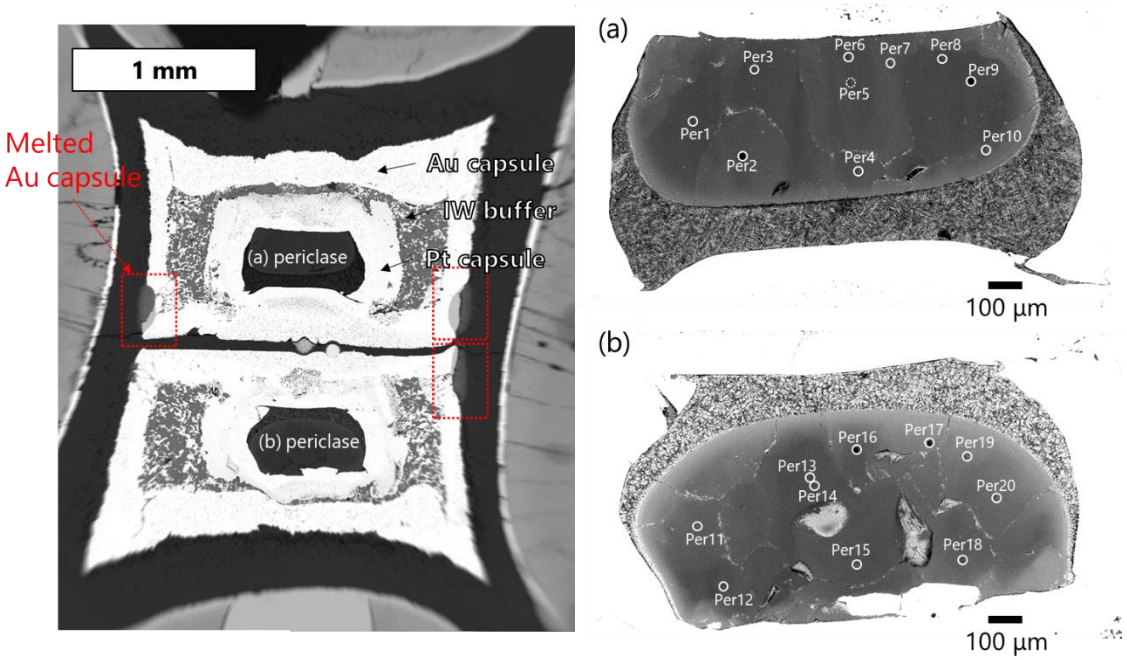

Figure 3.24. BSE images of recovered sample from 28 GPa, 1700 °C (OT2476). The left figure is a whole BSE image of the recovered sample before NanoSIMS analysis. The left figures are the BSE images of the two samples obtained by FE-SEM after NanoSIMS analysis; both (a) and (b) were started from MgO composition. However, all run products were contaminated from Fe-FeO buffer and were bearing FeO. Circles correspond to analysis points. Per, periclase.

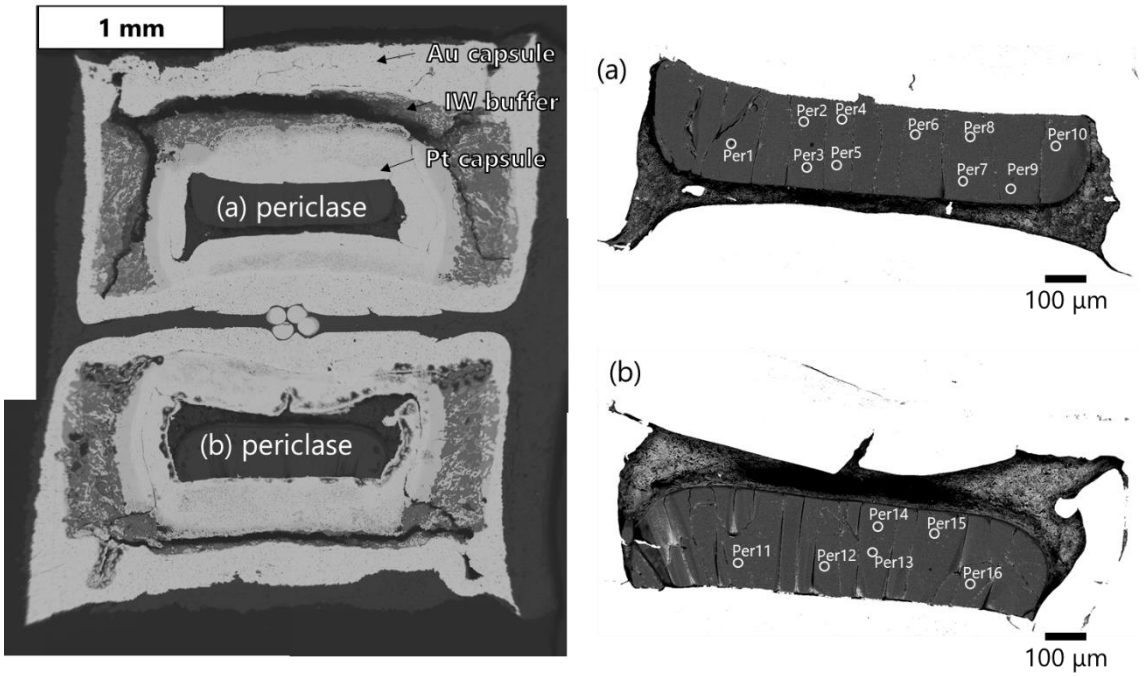

Figure 3.25. BSE images of recovered sample from 28 GPa, 1600 °C (OT2516). The left figure is a whole BSE image of the recovered sample before NanoSIMS analysis. The right figures are the BSE images of the two samples obtained by FE-SEM after NanoSIMS analysis; both (a) and (b) were started from MgO composition. Circles correspond to analysis points. Per, periclase.

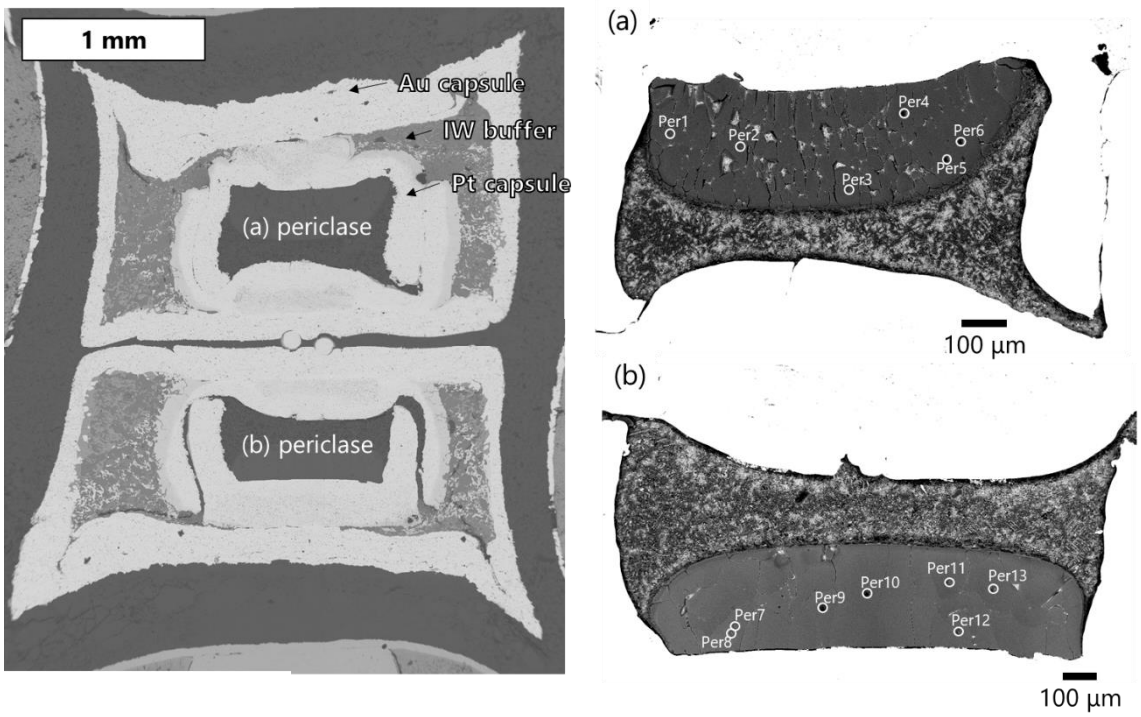

Figure 3.26. BSE images of recovered sample from 28 GPa, 1500 °C (OT2610). The left figure is a whole BSE image of the recovered sample before NanoSIMS analysis. The right figures are the BSE images of the two samples obtained by FE-SEM after NanoSIMS analysis; both (a) and (b) were started from MgO composition. Circles correspond to analysis points. Per, periclase.

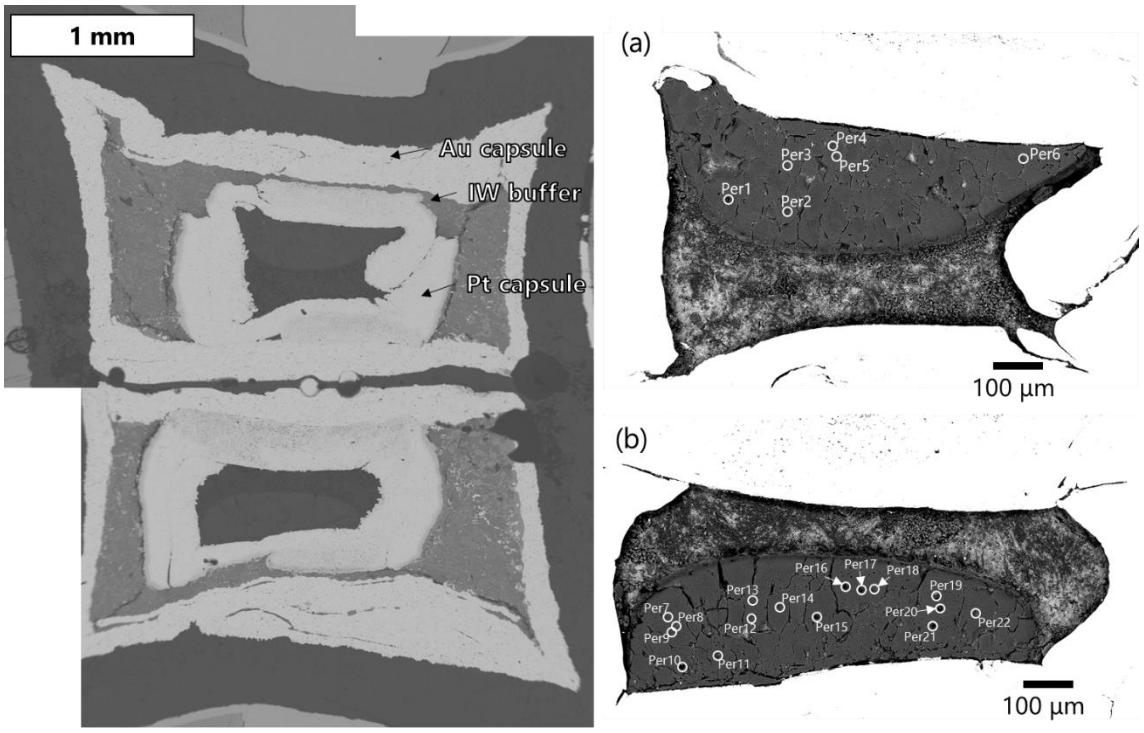

Figure 3.27. BSE images of recovered sample from 28 GPa, 1500 °C (OT2611). The left figure is a whole BSE image of the recovered sample. The right figures are the BSE images of the two samples obtained by FE-SEM-EDS after NanoSIMS analysis; both (a) and (b) were started from MgO composition. Circles correspond to analysis points. Some of analysis points were bearing FeO contaminated from Fe-FeO buffer. Per, periclase.

3.5. Raman spectra

Raman spectra were measured for all run products to identify stishovite and bridgmanite. The identification of stishovite and bridgmanite was based on Raman shifts reported in previous studies (Hemley et al. 1986; Gillet et al., 2000). In almost all of the run products starting from bridgmanite composition, clear Raman shifts were obtained, which were identified with bridgmanite, as shown in Figure 3.28.

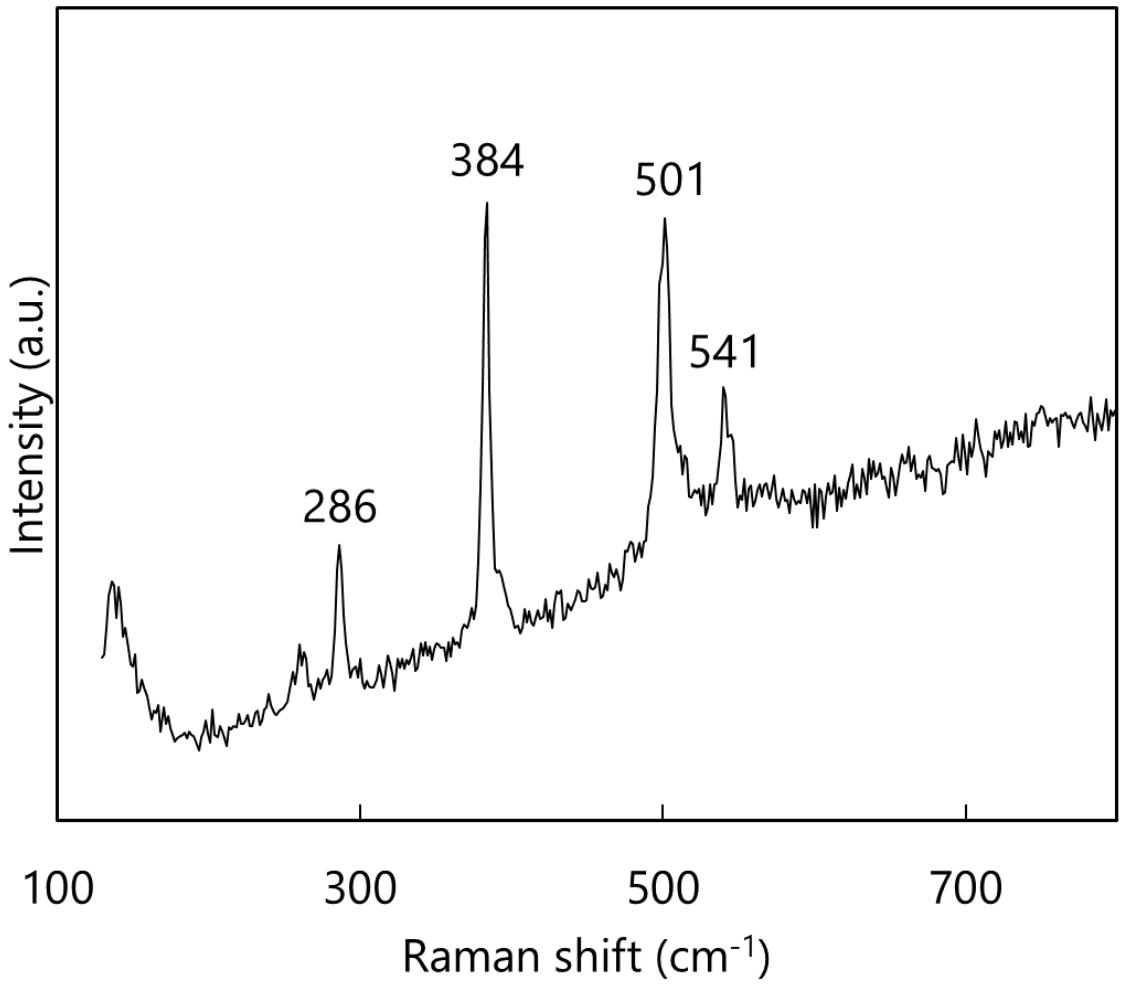

Figure 3.28. Raman spectrum of an Al-free bridgmanite (OS3083).

In OT2258, OT2259, and OT2427, vitrified grains with a bridgmanite composition were found, and in OT2427, only vitrified grains were identified (see Figure 3.29). In OT2650, Raman peaks assignable to bridgmanite were not observed in the crystals of the bridgmanite composition. However, as shown in the other experimental results, the pressure and temperature conditions of OT2427 and OT2650 were high enough to form bridgmanite, but it was not quenched. I discuss nitrogen solubilities in bridgmanite using these data points in this thesis.

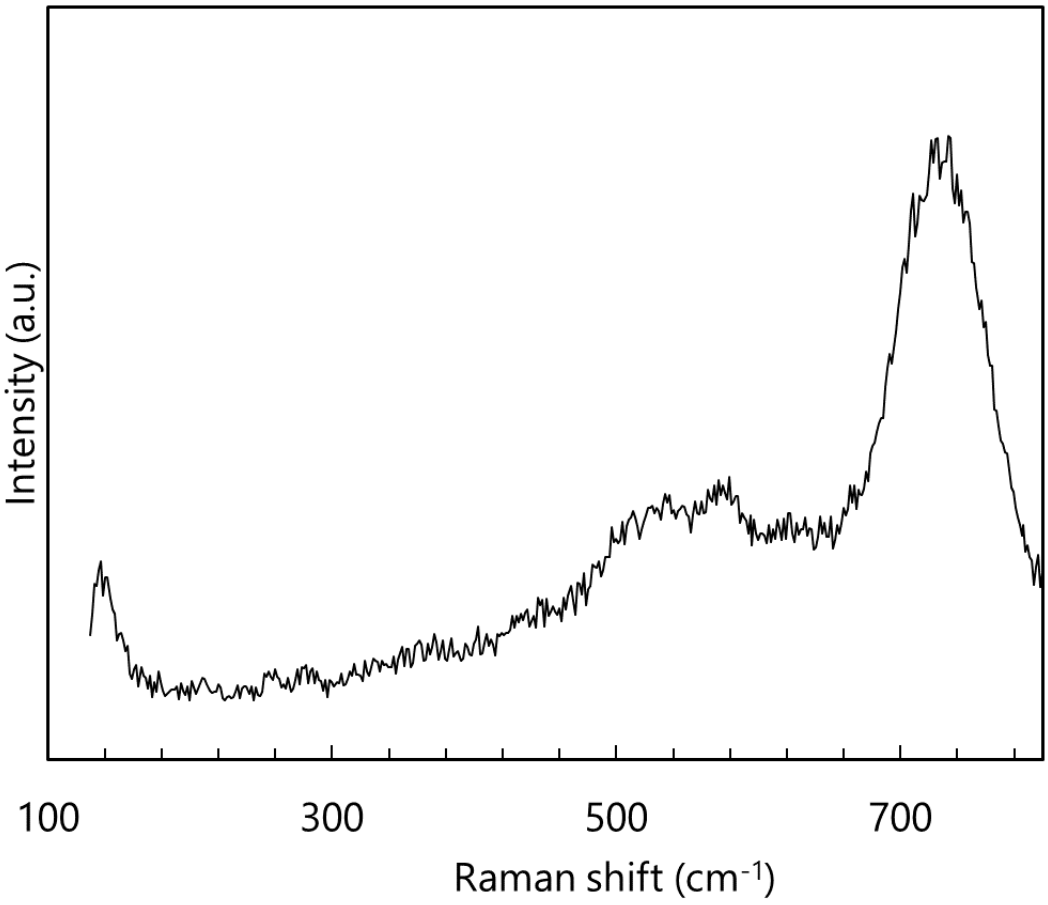

Figure 3.29. Raman spectrum of the former bridgmanite (OT2427).

3.5.1. Al-free bridgmanite

Figure 3.30 shows Raman spectra of Al-free bridgmanite recovered from the experimental conditions of 28 GPa and from 1400 °C to 1700 °C. All the obtained Raman spectra revealed bridgmanite, and the Raman shifts did not change with experimental temperatures.

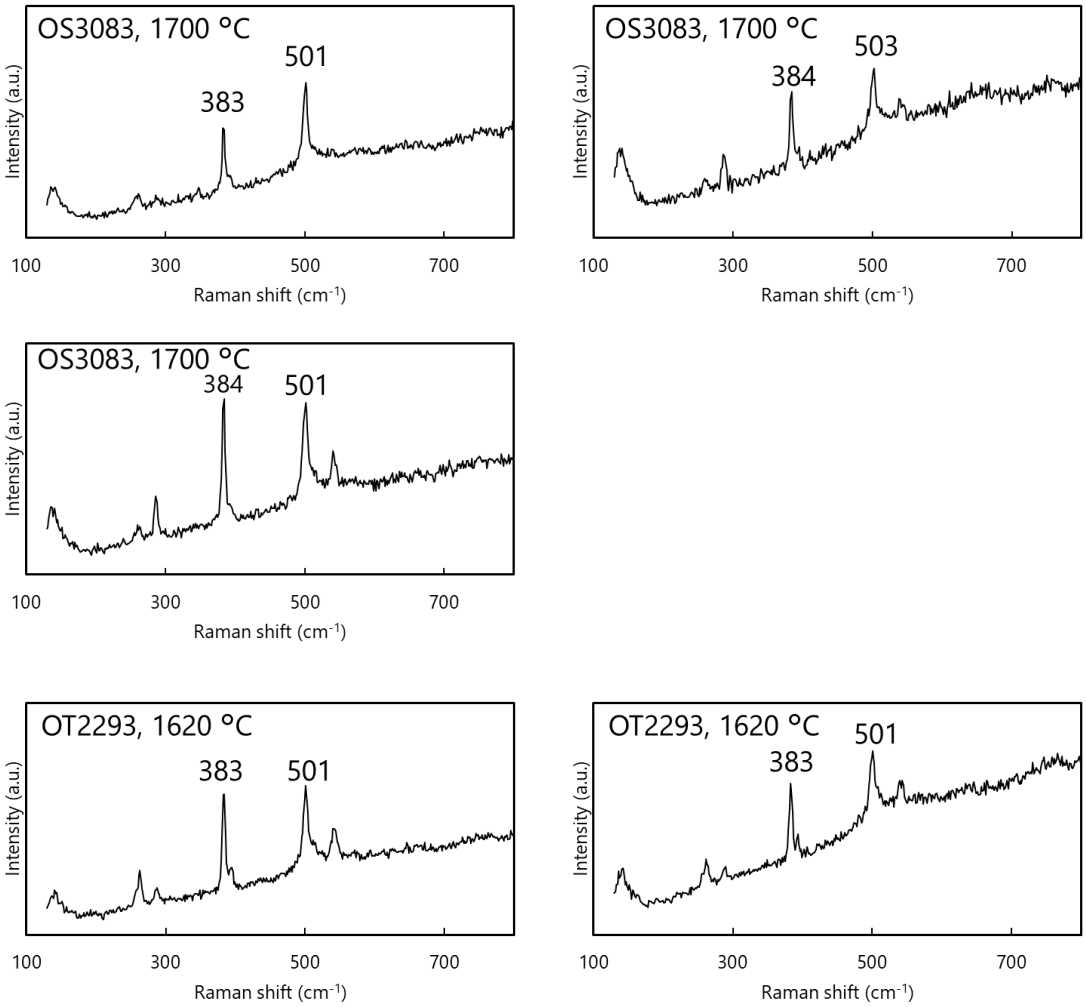

Figure 3.30. Raman spectra of Al-free bridgmanite

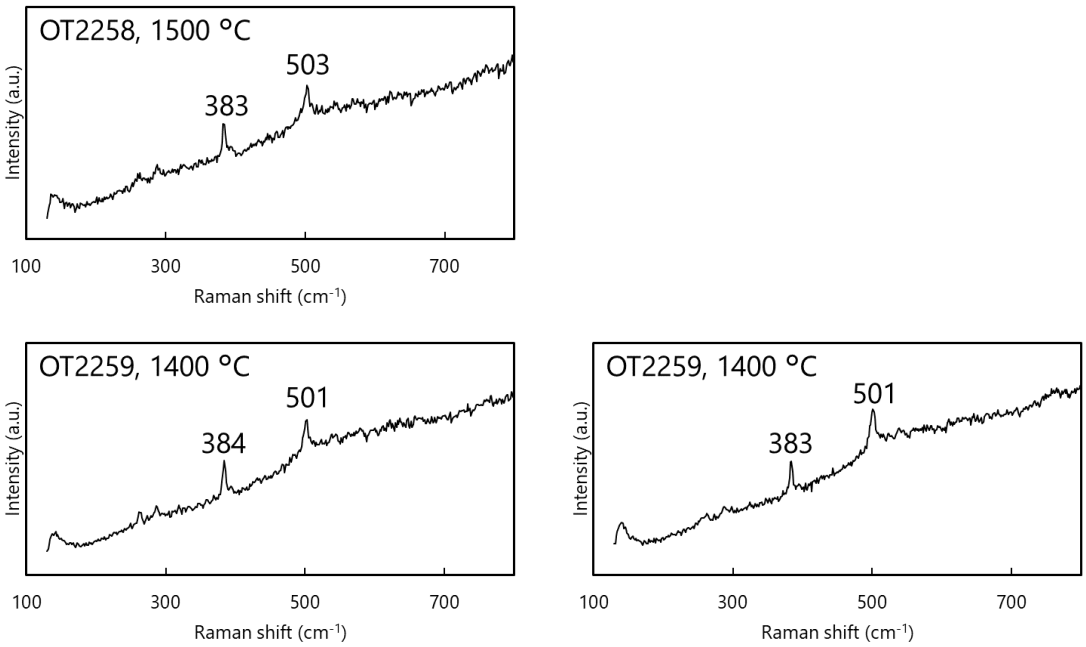

Figure 3.30 (Continued.)

3.5.2. Al-bearing bridgmanite

Figure 3.31 shows Raman spectra of Al-bearing bridgmanite 28 GPa from 1400 °C to 1700 °C. The obtained Raman spectra were not clear compared to Al-free bridgmanite and most of them were vitrified. The Raman shifts did not change with experimental temperatures or Al content.

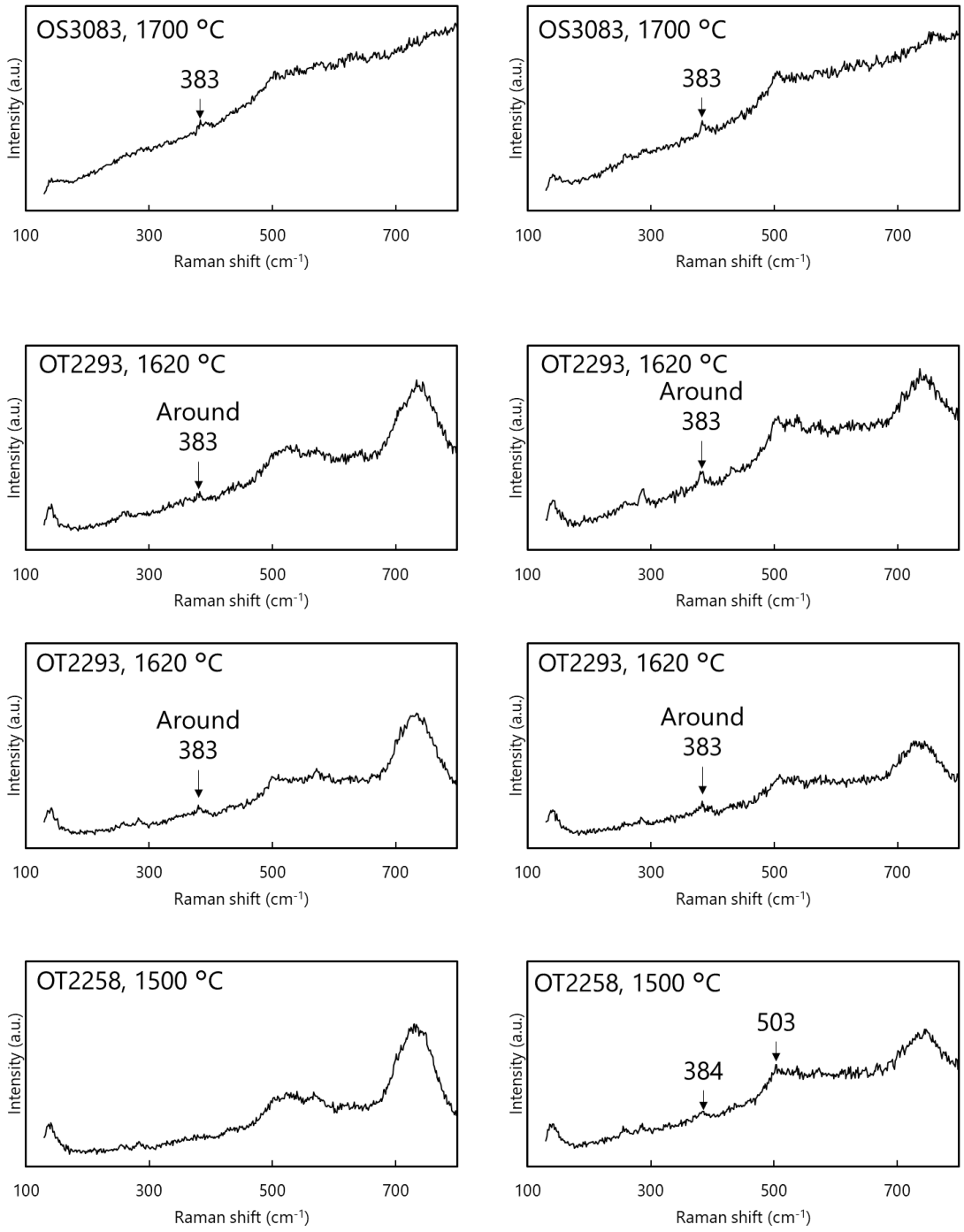

Figure 3.31. Raman spectra of Al-bearing bridgmanite.

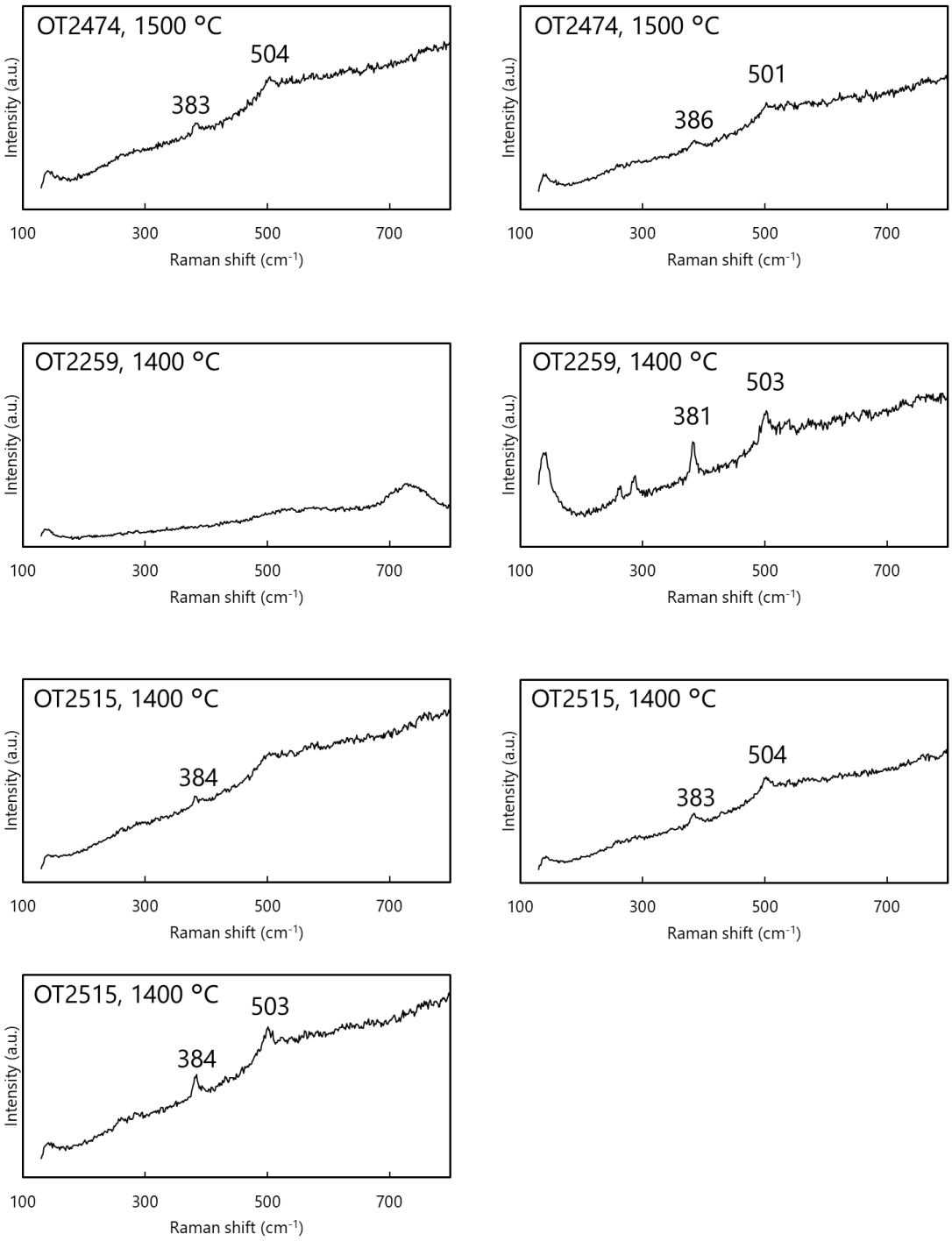

Figure 3.31 (Continued.)

3.5.3. Fe-bearing bridgmanite

Figure 3.32 shows Raman spectra of Fe-bearing bridgmanite under 28 GPa from 1620 °C. All the obtained Raman spectra were clear to identify bridgmanite and Raman shifts of bridgmanite did not change with experimental temperatures and Fe content in bridgmanite.

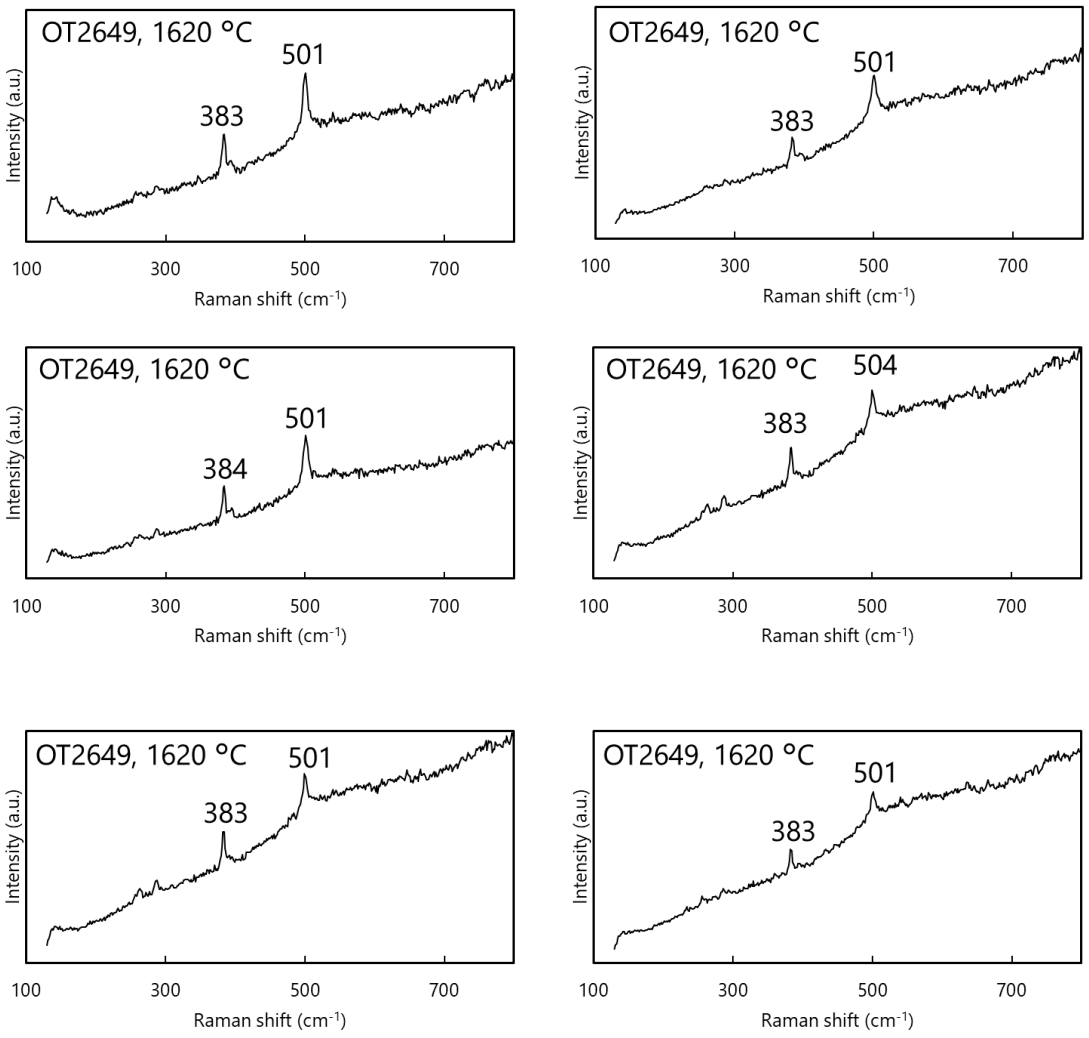

Figure 3.32. Raman spectra of Fe-bearing bridgmanite.

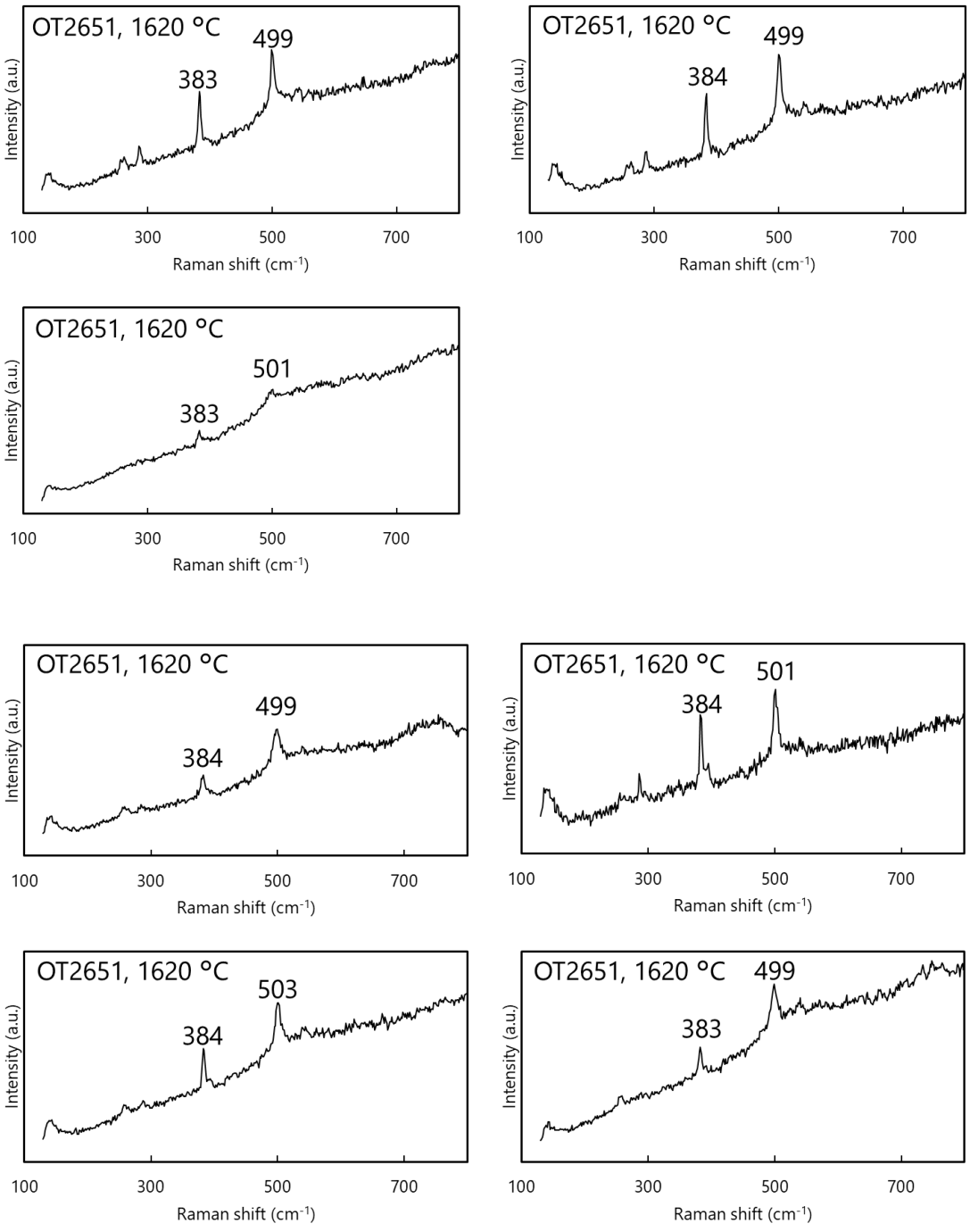

Figure 3.32 (Continued.)

3.5.4. Al-free stishovite

Figure 3.33 shows Raman spectra of Al-bearing stishovite produced under 28 GPa from 1400 to 1700 °C. the obtained Raman spectra clearly indicated bridgmanite, and its Raman shifts of did not change with experimental temperatures.

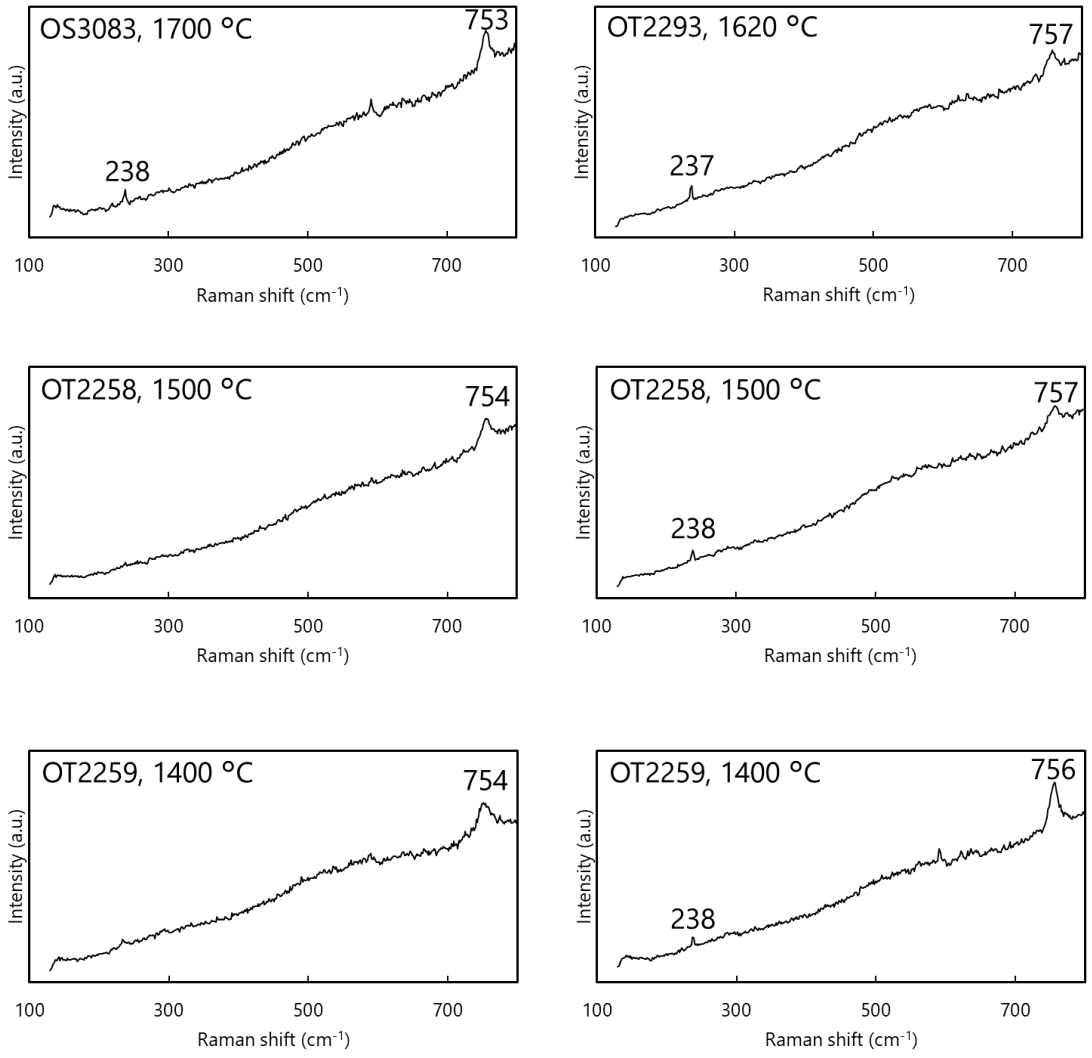

Figure 3.33. Raman spectra of Al-free stishovite.

3.5.5. Al-bearing stishovite

Figure 3.34 shows Raman spectra of Al-bearing stishovite produced under 28 GPa and 1400 °C. Raman spectroscopy was not conducted at all temperatures. However, Al-bearing stishovite was likely synthesized at the other temperatures because Al-free stishovite in the same cell was identified (see Figure 3.33).

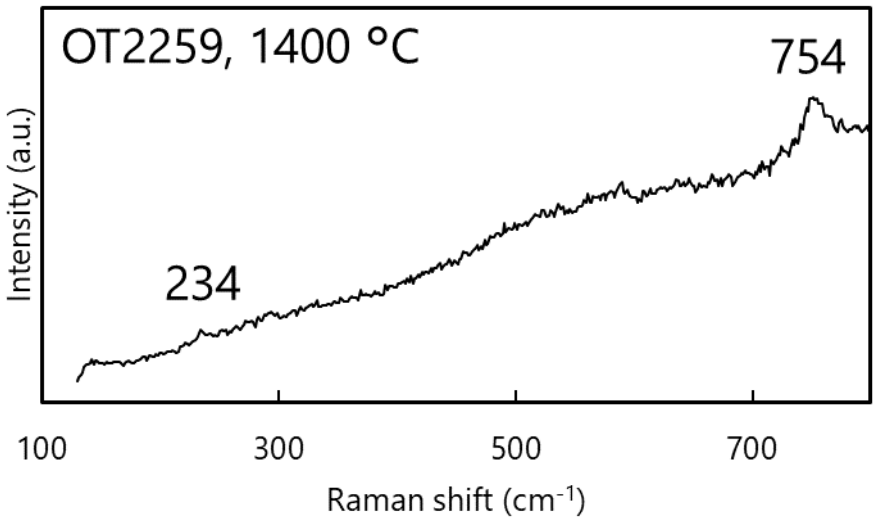

Figure 3.34. Raman spectrum of Al-bearing stishovite.

4. Discussion

4.1. Temperature dependence of nitrogen solubilities in stishovite

Figure 4.1 shows the temperature dependence of nitrogen solubility in Al-free stishovite. The nitrogen solubility in stishovite varied from 90 ppm (μg/g) to 404 ppm (μg/g) based on OT2259 (1400 °C), OT2258 (1500 °C), OT2293 (1620 °C), and OS3083 (1700 °C). Stishovite can incorporate higher nitrogen concentrations than bridgmanite (21.5 ± 18.1 ppm, Yoshioka et al., 2018). Additionally, the nitrogen solubility in stishovite increases with temperature, suggesting that nitrogen might be incorporated into lattice defects. Li et al. (2013) raised two possibilities for nitrogen incorporation: N^{3-} into oxygen vacancies and N_2 as Schottky defects in enstatite. The substitution of N^{3-} can occur in stishovite because oxygen vacancies may increase in stishovite at higher temperatures, although substitutions between N^{3-} and O^{2-} require charge compensation. Nitrogen in stishovite can also exist as NH_4^+ because stishovite recovered from high temperature and high temperature contained several thousand ppm of potassium, which can replace NH_4^+ (e.g., Irifune et al., 1994). NH_4-bearing silicate minerals release nitrogen at temperatures of 750–1000 °C (Yang et al., 2017; Sokol et al., 2018; Liu et al., 2019), but this trend may not apply to stishovite, which has a crystal structure different from NH_4-bearing silicate minerals. Nitrogen solubilities in stishovite are higher than those of mantle minerals (see Figure 1.6).

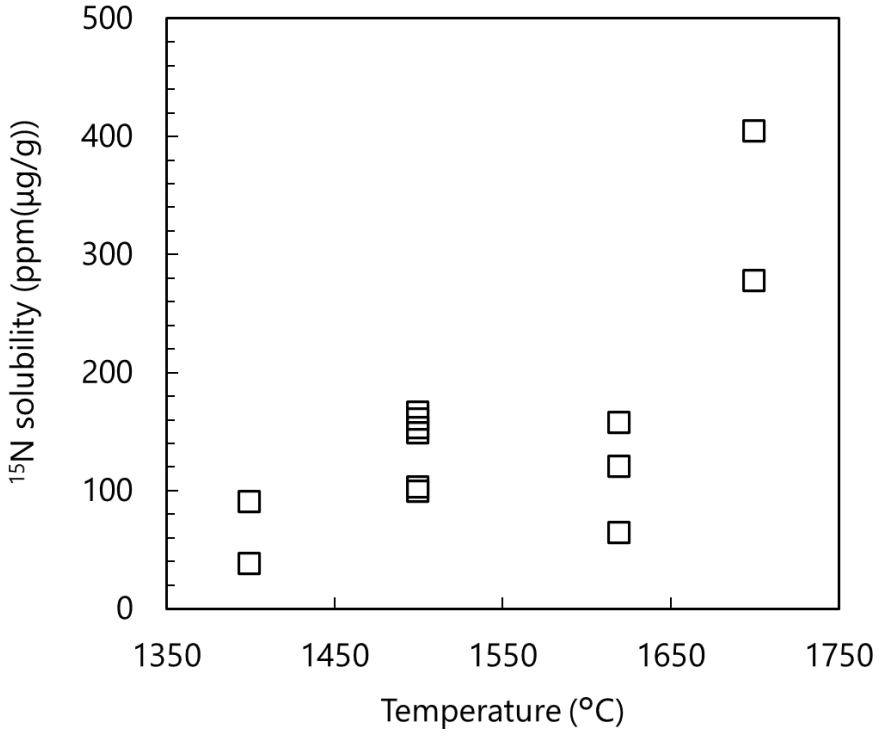

Figure 4.1. Nitrogen solubility in Al-free stishovite at different temperatures. All points correspond to single measurement points.

4.2. Relationship between Al content and nitrogen solubilities in stishovite

4.3. Temperature dependence of nitrogen solubilities in bridgmanite ($MgSiO_3$)

4.4. Relationship between Al_2O_3 contents and nitrogen solubilities in bridgmanite

4.5. Relationship between FeO contents and nitrogen solubilities in bridgmanite

4.6. Relationship between FeO content and nitrogen incorporation in periclase

4.7. Transportation of nitrogen into the deep upper mantle by major minerals in subducted continental crusts and sediments.

As shown in Figure 4.2, subducting oceanic crusts have three layers: the sediment layer, the basaltic layer, and the gabbro layer.

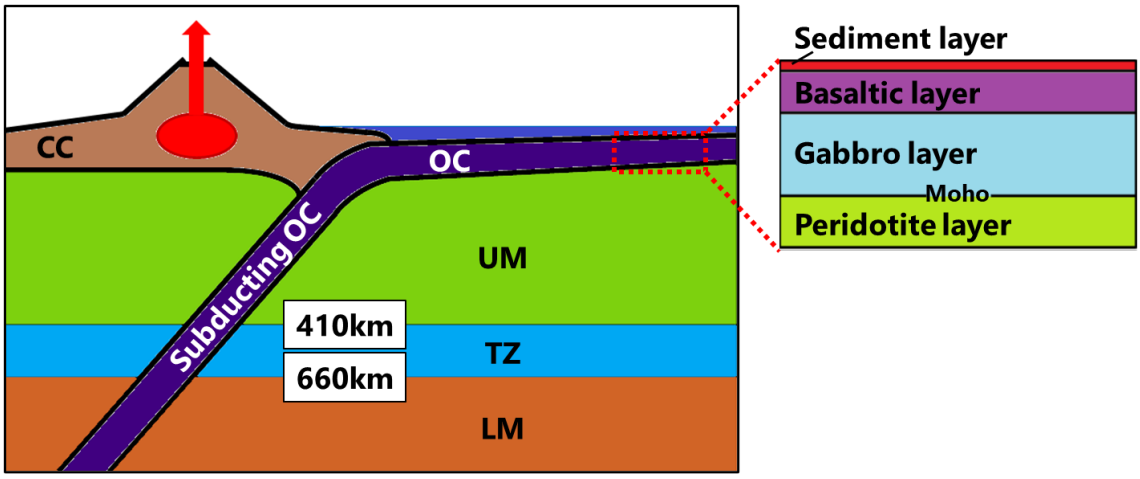

Figure 4.2. Schematics of subducting oceanic crust and layer structure of the oceanic crust based on Bodnar (2013). CC: continental crust, OC: oceanic crust, UM: upper mantle, TZ: mantle transition zone, LM: lower mantle.

The phase relations of these subducted materials in the deeper part of the Earth's mantle have been determined from high-pressure and high-temperature experiments (e.g., Irifune et al., 1994; Ono et al., 2001). The sediment layer rich in nitrogen (Johnson and Goldblatt et al., 2015) is important for discussing nitrogen behavior in subducting slabs, and the phase relations of the sediment layer are shown in Figure 4.3. Stishovite crystallizes at approximately 9 GPa and accounts for approximately 40 vol% of the subducted sediment. The density of stishovite is the highest in minerals in the sediment layer (e.g., Irifune et al., 1994) and can be gravitationally stable in the lower mantle.

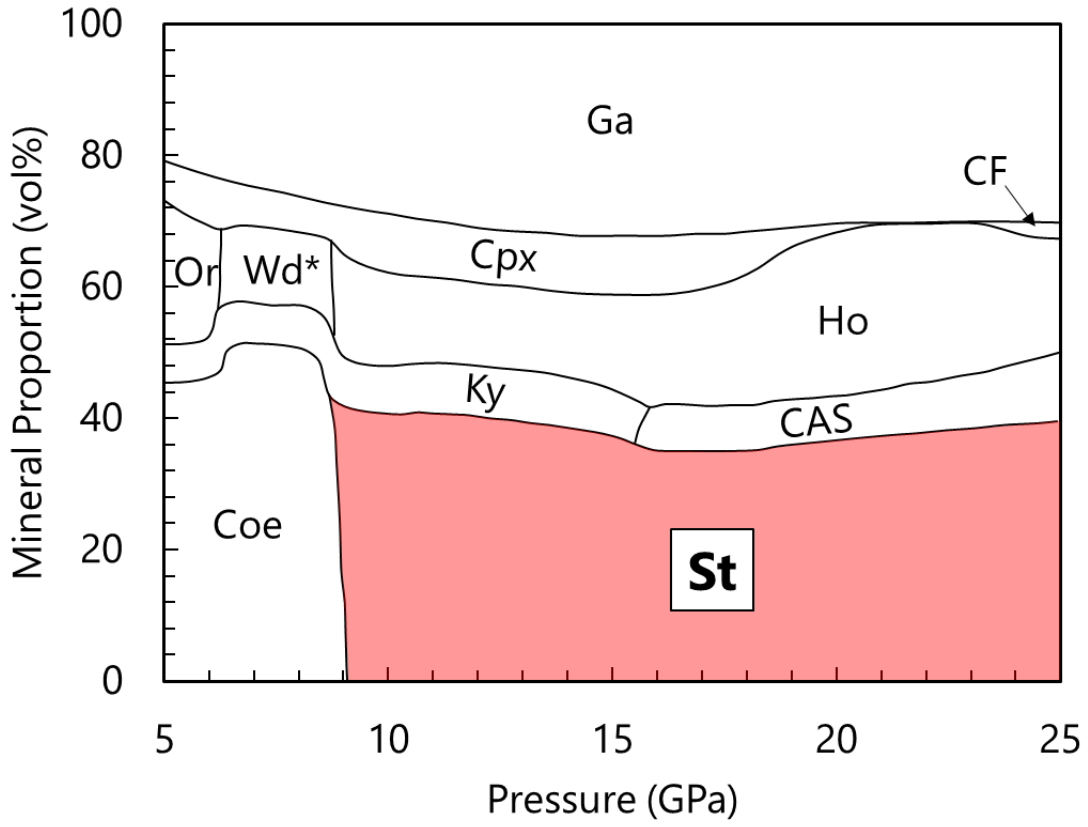

Figure 4.3. Mineral assemblages in subducting sediments depending on pressure (modified from Irifune et al. (1994)). Ga: garnet, Cpx: clinopyroxene, Or: orthoclase, Ky: kyanite, Coe: coesite, Wd: wadeite, Ho: hollandite, St: stishovite, CAS: unidentified Ca and Al-rich silicate, CF: calcium ferrite-type phase.

***Some potassium-rich phases that can be wadeite were identified, but they were too small to be analyzed by electron microprobe.**

The subducting continental crust rich in nitrogen (Johnson and Goldblatt et al., 2015) also influences nitrogen behavior in subducting slabs, and the phase relations of continental crusts are shown in Figure 4.4. Stishovite crystallizes at approximately 9 GPa and accounts for approximately 30 vol% of the subducted continental crust. Ingalls et al. (2016) reported that continental crusts can subduct into the mid-upper mantle despite its high buoyancy. Lee et al. (2017) reported that subduction erosion plays an important role in nitrogen transport into the mantle based on nitrogen isotope data.

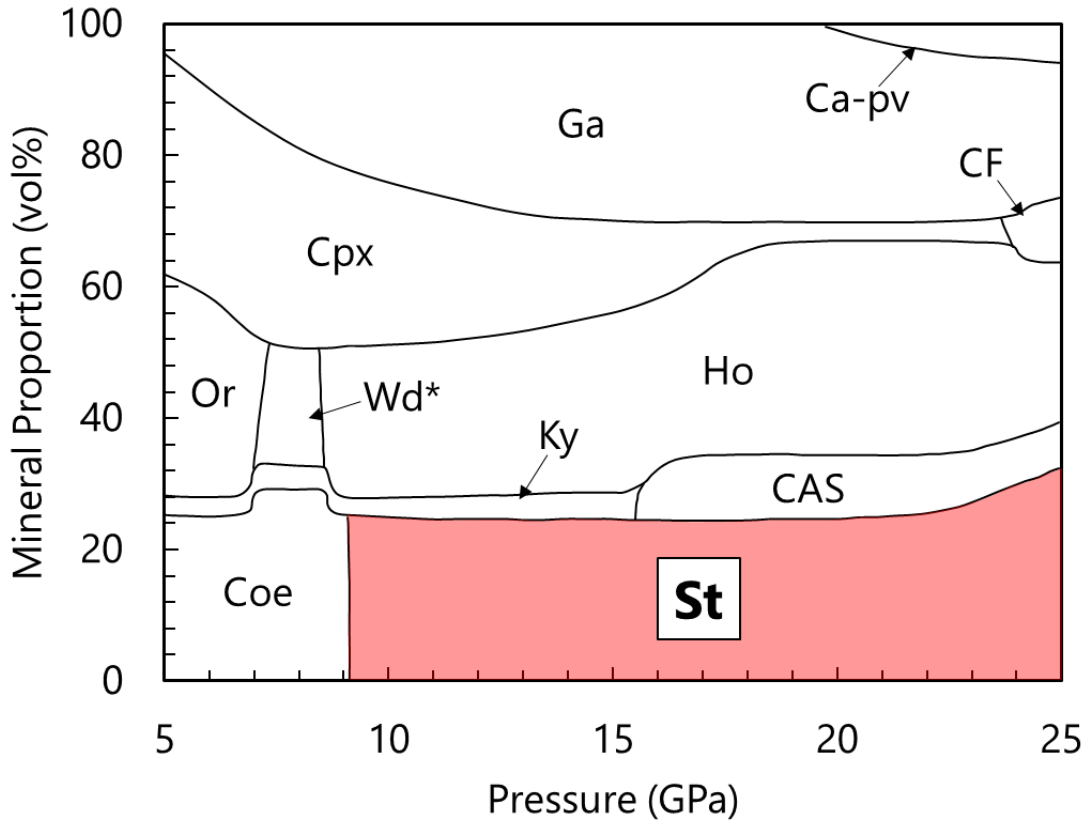

Figure 4.4. Mineral assemblages in subducting continental crust versus pressure (modified from Irifune et al. (1994)). Ga: garnet, Cpx: clinopyroxene, Or: orthoclase, Ky: kyanite, Coe: coesite, Wd: wadeite, Ho: hollandite, St: stishovite, CAS: unidentified Ca and Al-rich silicate, Ca-pv: $CaSiO_3$ perovskite, CF: calcium ferrite-type phase.

***Some potassium-rich phases that can be wadeite were identified, but they were too small to be analyzed by electron microprobe.**

4.7.1. Estimation of subducted materials and maximum nitrogen mass transported by stishovite into the lower mantle through the Earth's history

The mineral proportion of clinopyroxene can incorporate a significant nitrogen concentration (Watenphul et al., 2010; Li et al., 2013) in subducted sediments and eroded continental crust and decreases with increasing depth (Irifune et al., 1994). Additionally, NH_4-bearing silicate minerals are thermodynamically unstable at high temperatures (Yang et al., 2017; Sokol et al., 2018; Liu et al., 2019). In contrast, stishovite, which can incorporate nitrogen at higher temperatures corresponding to the mantle geotherm (Katsura et al., 2010), as shown in this thesis, is the primary mineral in the subducted sediment and in the subducted eroded continental crust. Moreover, stishovite has the highest nitrogen solubility in major minerals formed by the phase transition in subducting slabs as clarified in this thesis. However, nitrogen solubilities in K-hollandite and garnet have not been estimated under the *P-T* conditions corresponding to the lower mantle, and future studies are expected to estimate nitrogen solubility in these minerals. I propose stishovite as the significant nitrogen carrier down to the transition zone and the lower mantle if stishovite can inherit nitrogen from clinopyroxene (Watenphul et al., 2010; Li et al., 2013) or other NH_4-bearing high-pressure minerals that are stable up to 12.8 GPa and 700 °C (Watenphul et al., 2009). This *P-T* condition corresponds to a depth of 400 km, where stishovite forms from the metamorphism of the subducted sediment.

Based on the mass of the subducted material, I estimated the mass of nitrogen exclusively transported by stishovite. Current subduction rates derived from sediments and continental crusts are, respectively, 1.65 km^3/ year and 2.1 km^3/year, consisting of > 1.7 km^3/year from subduction erosion and 0.4 km^3/year from crustal subduction during continental collision (Stern et al., 2011) as shown in Figure 4.5.

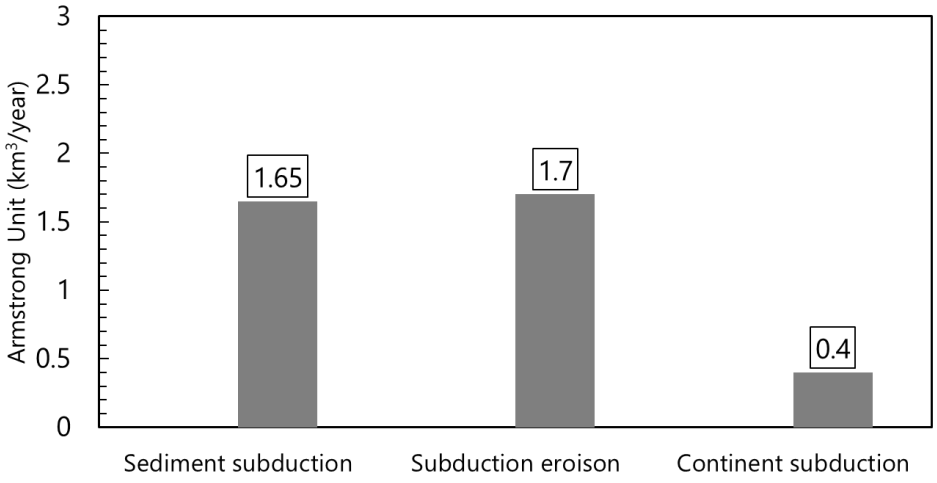

Figure 4.5. Mass of subducting materials originating from sediment and continental crusts (based on Stern et al., 2011).

Stishovite accounts for about 40 vol% of the subducted sediment and about 30 vol% of the continental crust, at pressures higher than 12.8 GPa or depths greater than 400 km (see Figure 4.3 and Figure 4.4). Stishovite can incorporate up to 90 μg/g nitrogen at 28 GPa and 1400 °C (see Figure 4.1) corresponding to the present cold slab geotherm (Syracuse et al., 2010). I estimated that stishovite could transport a maximum nitrogen quantity of 5.0×10^8 kg/year into the mantle transition zone and the lower mantle from these parameters. If stishovite can transport nitrogen into the lower mantle, almost all transported nitrogen can be retained. This is because the current nitrogen outgassing from the lower mantle (Ocean island basalt (OIB): 1.15×10^5 kg/year, see Table 1.3) is three orders of magnitude lower than the nitrogen amount transported into the lower mantle by stishovite. This estimation is based on the assumption that the mantle convection is layered or the chemical composition of the whole mantle is not homogeneous (e.g., Murakami et al., 2012; Mashino et al., 2020). Degassing of nitrogen from MORB should also be considered because the whole mantle convection is widely accepted (e.g., Brown and Shankland, 1981; Wang et al., 2015). If mass of nitrogen degassing from the lower mantle is attributed from both OIB and MORB, estimated mass of nitrogen released to the atmosphere is 6.18×10^7 kg (see Table 1.3) and that subducted into the lower mantle is 4.4×10^8 kg.

The start time of plate tectonics is essential for estimating the mass of subducted materials through the Earth's history but remains controversial. In previous studies, the start time of plate tectonics is varied from 0.85 Ga to 4.2 Ga (e.g., Hamilton 2011; Stern 2005; Brown 2006; Nutman et al., 2002; Komiya et al., 1999; Shirey et al., 2008; Hopkins et al., 2008). If the start time of plate tectonics is assumed to be 3.6–4.2 Ga, as reported by Nutman et al. (2002), Komiya et al. (1999), and Shirey et al. (2008), and Hopkins et al. (2008), the maximum estimation of nitrogen transported into the lower mantle ranged from 0.46 to 0.53 PAN (PAN: Mass of Present Atmospheric Nitrogen, 3.92×10^{18} kg). Assuming the whole mantle convection, the maximum mass of nitrogen transported into the lower mantle ranged from 0.40 to 0.47 PAN.

4.7.2. Formation of "Hidden" nitrogen reservoir in the lower mantle via subduction and implications for "missing" nitrogen

A nitrogen reservoir in the lower mantle can be formed via stishovite in subducting slabs. The phase transition of stishovite to $CaCl_2$-type SiO_2 occurs above approximately 54 GPa (Andrault et al., 1998), and stishovite may release nitrogen into the lower mantle. Metallic iron and bridgmanite in the reduced lower mantle can be important nitrogen reservoirs in the lower mantle (Kaminsky et al., 2015; Kaminsky and Wirth, 2017; Speelmanns et al., 2018; Yoshioka et al., 2018). These lower-mantle materials are expected to play a crucial role in reserving nitrogen released from stishovite. K-hollandite and garnet are formed by the transition of sediments and continental crusts subducted in the mantle (see Figure 4.3 and Figure 4.4). These minerals can also incorporate a notable amount of nitrogen in discussing subducted nitrogen via subducting slabs. Watenphul et al. (2010) and Li et al. (2013) reported nitrogen solubilities of NH_4-hollandite and pyrope based on experiments conducted under *P-T* conditions corresponding to the deep upper mantle. Although nitrogen solubilities in K-hollandite and garnet have not been estimated under *P-T* conditions corresponding to the lower mantle, the maximum nitrogen mass transported into the lower mantle via subducting slabs might be greater than the estimates solely based on stishovite transport. Compared to carbon, the formation of a nitrogen reservoir in the lower mantle via subducting slabs can deplete nitrogen effectively (see Table 1.3) and might explain the "missing" nitrogen.

4.7.3. Implication for the faint young Sun paradox

Subduction is expected to play an essential role in the co-evolution of the atmosphere and deep mantle, and this thesis focused on nitrogen behavior in the lower mantle. The nitrogen concentration in the Archean atmosphere remains controversial. Some researchers have reported that the partial pressure of nitrogen (pN_2) or the ancient atmospheric pressure was either lower or not notably higher than that of the present atmosphere (Som et al., 2012; Marty et al., 2013; Som et al., 2016). In contrast, it has been suggested that the pN_2 in the Archean atmosphere might have been markedly higher than that at present. Goldblatt et al. (2009) reported that nitrogen was transported into the deep Earth via subduction zones, and its concentration in the atmosphere decreased to the present level. These results were supported by the high-pressure experiments of Mallik et al. (2018). Barry and Hilton (2016) also reported that the early atmospheric nitrogen content was approximately 50% higher than today.

The results obtained in this thesis are consistent with previous studies that reported that the mass of nitrogen in the ancient atmosphere was greater than that at present (Goldblatt et al., 2009; Barry and Hilton et al., 2016; Mallik et al., 2018) if the nitrogen fluxes outgassing from the ancient and the present OIB are similar. Nitrogen transported into the lower mantle by stishovite and the formation of the deep nitrogen reservoirs might have affected the global nitrogen cycle and the history of the Earth's atmosphere. The whole Earth was not frozen in the Archean Earth despite the fainter Sun (Sagan and Mullen, 1972). The higher pN_2 in the atmosphere might reconcile the faint young Sun paradox (Goldblatt et al., 2009): greater nitrogen contents in the early Earth's atmosphere might have enhanced the greenhouse effect of CO_2. If the lower mantle could capture the nitrogen transported by stishovite, then a deep "hidden" nitrogen reservoir has formed in the lower mantle since the plate tectonics started (Figure 4.6).

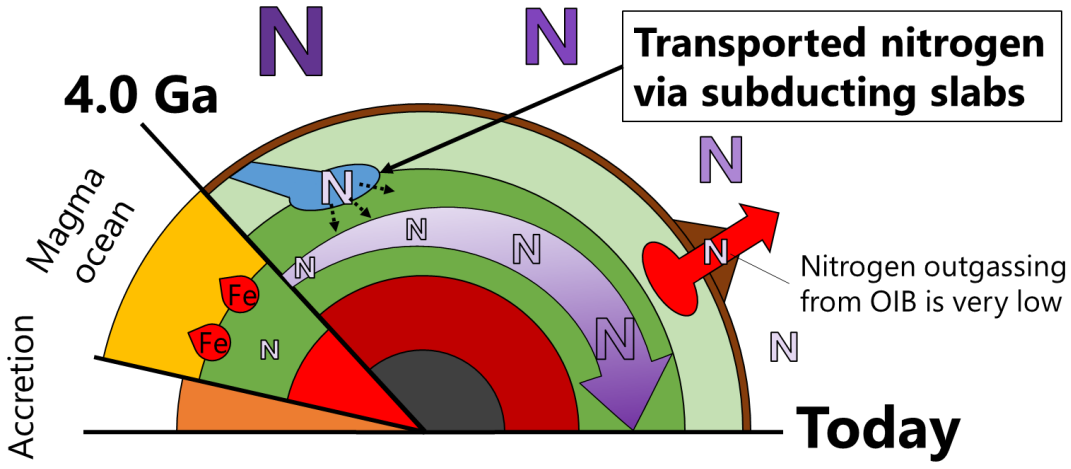

Figure 4.6. Deep "hidden" nitrogen reservoir formed by subducting slabs. UM the upper mantle, LM lower mantle, OIB oceanic island basalt.

4.8. Formation of nitrogen reservoir through solidification of magma ocean

In this chapter, I assume that the chemical composition of the Earth's lower mantle is equivalent to pyrolite (Ringwood, 1979) through the Earth's history, including the process of the magma ocean. Suppose the chemical composition of the early magma ocean was equivalent to ordinary chondrite or enstatite chondrite, stishovite could be crystallized during the solidification of the magma ocean (Ozawa et al., 2018), and stishovite can reserve more nitrogen than bridgmanite and ferropericlase (see Figure 4.1). Litvin et al. (2014) reported that stishovite coexisted with ferropericlase as inclusions in the super-deep diamonds originating in the lower mantle, although stishovite did not form Fe-bearing bridgmanite by reacting with ferropericlase. From high-pressure and high-temperature experiments, stishovite can be crystallized in the FeO-MgO-SiO_2 system (Litvin et al., 2016), and stishovite may be revealed to exist in the lower mantle in the future studies.

4.8.1. Role of bridgmanite coexisting metallic iron in formation of nitrogen reservoir in the lower mantle

4.8.2. Role of periclase as a nitrogen reservoir in the lower mantle

4.8.3. "Missing" nitrogen and the nitrogen capacity in the present lower mantle.

5. Conclusions

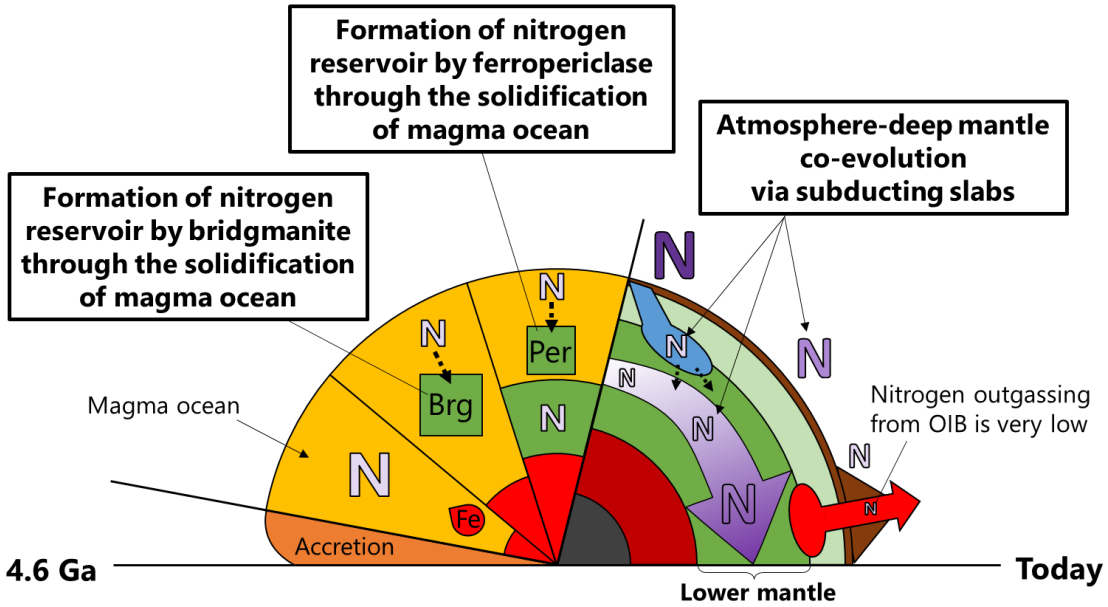

Figure 5.1. General implications in this thesis.

Here, I will mention about the perspectives and the implications in the future. In the mantle minerals, nitrogen solubility in majorite has not been reported in previous studies. In order to understand nitrogen budget in the bulk silicate Earth, nitrogen solubility in majorite is needed to be clarified. Majorite can be an important nitrogen reservoir because it occupies 15–40 vol% in the upper mantle and the mantle transition zone (see, Figure 1.6). The current nitrogen capacity in the upper mantle and the mantle transition zone will be larger. As mentioned before, majorite (garnet) occupies up to 30 vol% in the subducting slabs (see, Figure 4.3 and Figure 4.4), and can be an important nitrogen carrier down to the mantle transition zone.

Majorite can be an important nitrogen reservoir because it occupies 15–40 vol% in the upper mantle and the mantle transition zone (see, Figure 1.6). The current nitrogen capacities in the upper mantle (3.9 PAN) and the mantle transition zone (9 PAN) will be larger. As mentioned before, majorite (garnet) occupies up to 30 vol% in the subducting slabs (see, Figure 4.3 and Figure 4.4), and can be an important nitrogen carrier down to the mantle transition zone.

The *P-T* conditions in this thesis is limited to the lower mantle condition down to 750-800 km. In the future, nitrogen solubility in bridgmanite and ferropericlase needs to be investigated under higher pressure and temperature conditions corresponding to the whole lower mantle. The experimental pressure conditions of multi-anvil apparatus with sintered diamond anvils or nano-polycrystalline diamond anvils reached the lowermost-mantle conditions (Yamazaki et al., 2014; Kunimoto and Irifune, 2012), and the temperature conditions using boron-doped diamond heater reached 4000 K (Xie et al., 2017). This maximum temperature is higher than that of the magma ocean at temperatures of 3000–3600 K (Righter et al., 2011; Bouhifd and Jephcoat, 2011), allowing us a to discuss nitrogen behavior in the solidification of magma ocean without extrapolating temperature. Although it is still impossible to reproduce both high pressure and high temperature corresponding to the conditions in the lowermost mantle using a multi-anvil apparatus, the development of high-pressure and high-temperature experimental methods may reveal the capacity of nitrogen storage in the whole lower mantle in detail.

Acknowledgments

I deeply thank Professor Hiroyuki Kagi (Geochemical Research Center, Graduate School of Science, The University of Tokyo). Professor Hiroyuki Kagi was willing to have valuable discussions and gave me smart suggestions. Furthermore, he introduced a lot of researchers to me, which made a great contribution to this thesis and has greatly expanded my knowledge.

I gratefully thank Professor Toru Inoue (Graduate School of Advanced Science and Engineering, Hiroshima University) for their supports, guidance, and encouragements during the course of this work. He allowed me to join the collaborative research using multi-anvil apparatus gave me kind technical advices for multi-anvil apparatus.

I gratefully thank Professor Yuji Sano (Atmosphere and Ocean Research Institute, The University of Tokyo). He allowed me to join the collaborative research using NanoSIMS and gave me useful comments on my research.

I gratefully thank Dr. Shunichi Hishita (National Institute for Materials Science). He allowed me to collaborate using Ion Implanter RD-200l and gave me useful comments on my research.

I gratefully thank Dr. Evelyn Füri (Centre de Recherches Pétrographiques et Géochimiques), Ms. Cécile Deligny (University of Lorraine) and Professor Bernard Marty (University of Lorraine, CRPG-CNRS). They assigned me to join the collaborative research using high-resolution SIMS. Dr. Evelyn Füri and Ms. Cécile Deligny supported me during SIMS analysis.

I gratefully thank Dr. Hirotada Gotou (Institute for Solid State Physics of The University of Tokyo) for his technical support in operating a lathe for multi-anvil apparatus experiments.

I gratefully thank Dr. Toru Shinmei (Geodynamics Research center, Ehime University), Dr. Sho Kakizawa (Graduate School of Advanced Science and Engineering) and Mr. Masamichi Noda (Graduate School of Advanced Science and Engineering, Hiroshima Universoty) for their technical supports in operating Multi-anvil apparatus and crafting parts such as gaskets, pressure mediums, and metal capsules for high-pressure and high-temperature experiments.

I gratefully thank Dr. Naoto Takahata (Atmosphere and Ocean Research Institute, The University of Tokyo), Dr. Tsubasa Miki (Atmosphere and Ocean Research Institute, The University of Tokyo), and Dr. Hideto Yoshida (Department of Earth and Planetary Science, The University of Tokyo) for their technical supports during NanoSIMS and FE-SEM-EDS analysis.

I gratefully thank Professor Takashi Mikouchi (The University Museum, The University of Tokyo) for his technical supports during conducting the electric furnace.

I gratefully thank Dr. Kazuki Komatsu (Geochemical Research Center, Graduate School of Science, The University of Tokyo), Dr. Riko Iizuka (Geochemical Research Center, Graduate School of Science, The University of Tokyo), Emeritus Professor Takehiko Yagi (Geochemical Research Center, Graduate School of Science, The University of Tokyo) and Dr. Katsutoshi Aoki (Geochemical

Research Center, Graduate School of Science, The University of Tokyo). Their advices were very useful and very encouraging.

I also very gratefully thank all staffs and students in Geochemical research center for their many help and encouragement.

I gratefully thank Dr. Yuan Li (Guangzhou Institute of Geochemistry, Chinese Academy of Sciences) for valuable discussions about nitrogen in the Earth's interior.

I gratefully thank the previous academic advisors, Emeritus Professor Eiji Ohtani (Tohoku University), Dr. Akio Suzuki (Department of Earth Science, Tohoku University) and Dr. Yuki Shibazaki (High Energy Accelerator Research Organization). They introduced me to basics of high-pressure experiments when I was an undergraduate student, and these knowledges are very important for conducting this thesis.

I gratefully thank Professor Hikaru Iwamori (Earthquake Research Institute, The University of Tokyo), Professor Toshihiro Kogure (Department of Earth & Planetary Science, The University of Tokyo), Professor Tsuyoshi Komiya (Graduate School of Arts and Sciences, The University of Tokyo), Associate professor Hirochika Sumino (Graduate School of Arts and Sciences, The University of Tokyo), and Professor Kei Hirose (Department of Earth & Planetary Science, The University of Tokyo). They reviewed this doctoral dissertation.

Finally, I would like to thank my parents, Mr. Hiroshi Fukuyama and Dr. Ayako Fukuyama. They are so supportive and encouraging me. I can never thank you enough.

Reference

Allègre, C. J., Poirier, J. P., Humler, E. & Hofmann, A. W. The chemical composition of the Earth. *Earth Planet. Sci. Lett.* **134**, 515–526 (1995).

Bajgain, S. K., Mookherjee, M., Dasgupta, R., Ghosh, D. B. & Karki, B. B. Nitrogen Content in the Earth's Outer Core. *Geophys. Res. Lett.* **46**, 89–98 (2019).

Barry, P. H. & Hilton, D. R. Release of subducted sedimentary nitrogen throughout Earth's mantle. *Geochemical Perspect. Lett.* **2**, 148–159 (2016).

Barth, C.A. The photochemistry of the atmosphere of Mars, in *The Photochemistry of Atmospheres*, ed. by J.S. Levine (Academic Press, New York, 1985).

Bebout, G. E. & Fogel, M. L. Nitrogen-isotope compositions of metasedimentary rocks in the Catalina Schist, California: Implications for metamorphic devolatilization history. *Geochim. Cosmochim. Acta* **56**, 2839–2849 (1992).

Bergin, E. A., Blake, G. A., Ciesla, F., Hirschmann, M. M. & Li, J. Tracing the ingredients for a habitable earth from interstellar space through planet formation. **112**, 8965–8970 (2015).

Bodnar, R. J. *et al.* Whole Earth geohydrologic cycle, from the clouds to the core: The distribution of water in the dynamic Earth system. *Spec. Pap. Geol. Soc. Am.* **500**, 431–461 (2013).

Bogard, D. D., Clark, R. S., Keith, J. E. & Reynolds, M. A. Noble gases and radionuclides in Lost City and other recently fallen meteorites. *J. Geophys. Res.* **76**, 4076–4083 (1971).

Bouhifd, M. A. & Jephcoat, A. P. Convergence of Ni and Co metal-silicate partition coefficients in the deep magma-ocean and coupled silicon-oxygen solubility in iron melts at high pressures. *Earth Planet. Sci. Lett.* **307**, 341–348 (2011).

Brown, J. M. & Shankland, T. J. Thermodynamic parameters in the Earth as determined from seismic profiles. *Geophys. J. R. Astron. Soc.* **66**, 579–596 (1981).

Brown, M. Duality of thermal regimes is the distinctive characteristics of plate tectonics since the Neoarchean. *Geology* **34**, 961–964 (2006).

Busigny, V., Cartigny, P. & Philippot, P. Nitrogen isotopes in ophiolitic metagabbros: A re-evaluation of modern nitrogen fluxes in subduction zones and implication for the early Earth atmosphere. *Geochim. Cosmochim. Acta* **75**, 7502–7521 (2011).

Busigny, V., Cartigny, P., Philippot, P., Ader, M. & Javoy, M. Massive recycling of nitrogen and other fluid-mobile elements (K, Rb, Cs, H) in a cold slab environment: Evidence from HP to UHP oceanic metasediments of the Schistes Lustrés nappe (western Alps, Europe). *Earth Planet. Sci. Lett.* **215**, 27–42 (2003).

1Canfield, D. E., Glazer, A. N. & Falkowski, P. G. The evolution and future of earth's nitrogen cycle. *Science.* **330**, 192–196 (2010).

Cedeño, D. G. *et al.* An experimental study on smectites as nitrogen conveyors in subduction zones. *Appl. Clay Sci.* **168**, 1–6 (2019).

Chen, C., Smallwood, J. L., Martin, R. G. & Livio, M. Late delivery of nitrogen to Earth. *Astron. J.* **157**, 1–10 (2019).

Cline, C. J., Faul, U. H., David, E. C., Berry, A. J. & Jackson, I. Redox-influenced seismic properties of uppermantle olivine. *Nature* **555**, 355–358 (2018).

Costa, A., Caricchi, L. & Bagdassarov, N. A model for the rheology of particle-bearing suspensions and partially molten rocks. *Geochemistry, Geophys. Geosystems* **10**, 1–13 (2009).

Dalou, C., Hirschmann, M. M., von der Handt, A., Mosenfelder, J. & Armstrong, L. S. Nitrogen and carbon fractionation during core–mantle differentiation at shallow depth. *Earth Planet. Sci. Lett.* (2017).

Diaz, R. J. & Rosenberg, R. Spreading dead zones and consequences for marine ecosystems. *Science.* **321**, 926–929 (2008).

Dobrzhinetskaya, L. F. *et al.* High-pressure highly reduced nitrides and oxides from chromitite of a Tibetan ophiolite. *Proc. Natl. Acad. Sci. U. S. A.* **106**, 19233–19238 (2009).

Dobrzhinetskaya, L. F. *et al.* Qingsongite, natural cubic boron nitride: The first boron mineral from the Earth's mantle. *Am. Mineral.* **99**, 764–772 (2014).

Duce, R. A. *et al.* Impacts of atmospheric anthropogenic nitrogen on the open ocean. *Science.* **320**, 893–897 (2008).

Dziewonski, A. M. & Anderson, D. L. Preliminary reference Earth model. *Phys. Earth Planet. Inter.* **25**, 297–356 (1981).

Elkins-Tanton, L. T. Magma oceans in the inner solar system. *Annu. Rev. Earth Planet. Sci.* **40**, 113–139 (2012).

Fegley, B., Properties and composition of the terrestrial oceans and of the atmospheres of the Earth and other planets, *in Global Earth Physics: A Handbook of Physical Constants*, edited by T. J. Ahrens, AGU, Washington, D. C. 320–345 (1995).

Fei, H., Liu, Z., McCammon, C. & Katsura, T. Oxygen Vacancy Substitution Linked to Ferric Iron in Bridgmanite at 27 GPa. *Geophys. Res. Lett.* **47**, 1–9 (2020).

Fei, Y. *et al.* Experimentally determined postspinel transformation boundary in Mg 2 SiO 4 using MgO as an internal pressure standard and its geophysical implications. *J. Geophys. Res. Solid Earth* **109**, 1–8 (2004).

Elkins-Tanton, L. T. Linked magma ocean solidification and atmospheric growth for Earth and Mars. *Earth Planet. Sci. Lett.* **271**, 181–191 (2008).

Frost, D. J. *et al.* Experimental evidence for the existence of iron-rich metal in the Earth's lower mantle. *Nature* **428**, 409–412 (2004).

Frost, D. J. & McCammon, C. A. The Redox State of earth's mantle. *Annu. Rev. Earth Planet. Sci.* **36**, 389–420 (2008).

Fukao, Y. *et al.* Stagnant slab: A review. *Annu. Rev. Earth Planet. Sci.* **37**, 19–46 (2009).

Füri, E., Deloule, E. & Dalou, C. Nitrogen abundance and isotope analysis of silicate glasses by secondary ionization mass spectrometry. *Chem. Geol.* **493**, 327–337 (2018).

Galloway, J. N. *et al. Nitrogen cycles: past, present, and future*. *Biogeochemistry* vol. 70 (2004).

Galloway, J. N. *et al.* Transformation of the Nitrogen Cycle: Recent Trends, Questions, and Potential Solutions. *Science.* **320**, 889–893 (2008).

Gibbs, G. V., Cox, D. F. & Ross, N. L. A modeling of the structure and favorable H-docking sites and defects for the high-pressure silica polymorph stishovite. *Phys. Chem. Miner.* **31**, 232–239 (2004).

Gillet, P., Daniel, I., Guyot, F., Matas, J. & Chervin, J. C. A thermodynamic model for MgSiO3-perovskite derived from pressure, temperature and volume dependence of the Raman mode frequencies. *Phys. Earth Planet. Inter.* **117**, 361–384 (2000).

Goldblatt, C. *et al.* Nitrogen-enhanced greenhouse warming on earlyEarth. *Nat. Geosci.* **2**, 891–896 (2009).

Grewal, D. S., Dasgupta, R., Sun, C., Tsuno, K. & Costin, G. Delivery of carbon, nitrogen, and sulfur to the silicate earth by a giant impact. *Sci. Adv.* **5**, 1–13 (2019a).

Grewal, D. S. *et al.* The fate of nitrogen during core-mantle separation on Earth. *Geochim. Cosmochim. Acta* **251**, 87–115 (2019b).

Gruber, N. & Galloway, J. N. An Earth-system perspective of the global nitrogen cycle. *Nature* **451**, 293–296 (2008).

Grüninger, H. *et al.* Oxygen Vacancy Ordering in Aluminous Bridgmanite in the Earth's Lower Mantle. *Geophys. Res. Lett.* **46**, 8731–8740 (2019).

Halama, R., Bebout, G. E., John, T. & Schenk, V. Nitrogen recycling in subducted oceanic lithosphere: The record in high- and ultrahigh-pressure metabasaltic rocks. *Geochim. Cosmochim. Acta* **74**, 1636–1652 (2010).

Hamilton, W. B. Plate tectonics began in Neoproterozoic time, and plumes from deep mantle have never operated. *Lithos* **123**, 1–20 (2011).

Hart, S. R. & Zindler, A. In search of a bulk-Earth composition. *Chem. Geol.* **57**, 247–267 (1986).

Hashizume, K., Kase T., Matsuda J. I. & Sato H. On the siderophile behavior of nitrogen and carbon: Implications for their inventory in the Earth. *Kazan* **42**, S293-S301 (1997).

Hemley, R. J., Mao, H. K. & Chao, E. C. T. Raman spectrum of natural and synthetic stishovite. *Phys. Chem. Miner.* **13**, 285–290 (1986).

Hirose, K., Sinmyo, R. & Hernlund, J. Perovskite in the Earth's deep interior. *Science.* **738**, 734–738 (2017).

Hirschmann, M. M. & Dasgupta, R. The H/C ratios of Earth's near-surface and deep reservoirs, and consequences for deep Earth volatile cycles. *Chem. Geol.* **262**, 4–16 (2009).

Hopkins, M., Harrison, T. M. & Manning, C. E. Low heat flow inferred from >4 Gyr zircons suggests Hadean plate boundary interactions. *Nature* **456**, 493–496 (2008).

Ingalls, M., Rowley, D. B., Currie, B. & Colman, A. S. Large-scale subduction of continental crust implied by India-Asia mass-balance calculation. *Nat. Geosci.* **9**, 848–853 (2016).

Irifune, T., Ringwood, A. E. & Hibberson, W. O. Subduction of continental crust and terrigenous and pelagic sediments: an experimental study. *Earth Planet. Sci. Lett.* **126**, 351–368 (1994).

Irifune, T. *et al.* Iron partitioning and density changes of pyrolite in Earth's lower mantle. *Science.* **327**, 193–195 (2010).

Jagoutz, E. *et al.* The abundances of major, minor and trace elements in the earth's mantle as derived from primitive ultramafic nodules. *Lunar Planet. Sci. Conf. Proc.* **10**, 2031–2050 (1979).

Jephcoat, A. P. Rare-gas solids in the earth's deep interior. *Nature* **393**, 355–358 (1998).

Johnson, B. & Goldblatt, C. The nitrogen budget of Earth. Earth Sci. Rev. 148, 150–173 (2015)

Johnston, D. T., Wolfe-Simon, F., Pearson, A. & Knoll, A. H. Anoxygenic photosynthesis modulated Proterozoic oxygen and sustained Earth's middle age. *Proc. Natl. Acad. Sci. U. S. A.* **106**, 16925–16929 (2009).

Kakizawa, S., Inoue, T. & Nishi, M. Behavior of Al-bearing hydrous bridgmanite at high pressure Crystal chemistry of a hydrous phase. 345–357 (2016).

Kaminsky, F. Mineralogy of the lower mantle: A review of 'super-deep' mineral inclusions in diamond. *Earth-Science Rev.* **110**, 127–147 (2012).

Kaminsky, F. & Wirth, R. Nitrides and carbonitrides from the lowermost mantle and their importance in the search for Earth's 'lost' nitrogen. *Am. Mineral.* **102**, 1667–1676 (2017).

Katsura, T., Yoneda, A., Yamazaki, D., Yoshino, T. & Ito, E. Adiabatic temperature profile in the mantle. *Phys. Earth Planet. Inter.* **183**, 212–218 (2010).

Keppler, H., Wiedenbeck, M. & Shcheka, S. S. Carbon solubility in olivine and the mode of carbon storage in the Earth's mantle. *Nature* **424**, 414–416 (2003).

Kerridge, J. F. Carbon, hydrogen and nitrogen in carbonaceous chondrites: Abundances and isotopic compositions in bulk samples. *Geochim. Cosmochim. Acta* **49**, 1707–1714 (1985).

Komiya, T. *et al.* Plate tectonics at 3.8-3.7 Ga: Field evidence from the Isua Accretionary Complex, southern West Greenland. *J. Geol.* **107**, 515–554 (1999).

Korenaga, J. Initiation and evolution of plate tectonics on earth: Theories and observations. *Annu. Rev. Earth Planet. Sci.* **41**, 117–151 (2013).

Kunimoto, T. & Irifune, T. Pressure generation to 125 GPa using a 6-8-2 type multianvil apparatus with nano-polycrystalline diamond anvils. *J. Phys. Conf. Ser.* **215**, (2010).

Kuypers, M. M. M., Marchant, H. K. & Kartal, B. The microbial nitrogen-cycling network. *Nat. Rev. Microbiol.* **16**, 263–276 (2018).

Lammer, H. *et al.* Origin and evolution of the atmospheres of early Venus, Earth and Mars. *Astron. Astrophys. Rev.* **26**, (2018).

Lee, H. *et al.* Nitrogen recycling at the Costa Rican subduction zone: The role of incoming plate structure. *Sci. Rep.* **7**, 1–10 (2017).

Li, Y., Wiedenbeck, M., Shcheka, S. & Keppler, H. Nitrogen solubility in upper mantle minerals. *Earth Planet. Sci. Lett.* **377**–**378**, 311–323 (2013).

Li, Y. & Keppler, H. Nitrogen speciation in mantle and crustal fluids. *Geochim. Cosmochim. Acta* **129**, 13–32 (2014).

Libourel, G., Marty, B. & Humbert, F. Nitrogen solubility in basaltic melt. Part I. Effect of oxygen fugacity. *Geochim. Cosmochim. Acta* **67**, 4123–4135 (2003).

Litvin, Y. A. The stishovite paradox in the genesis of superdeep diamonds. *Dokl. Earth Sci.* **455**, 274–278 (2014).

Litvin, Y. A., Spivak, A. V. & Dubrovinsky, L. S. Magmatic evolution of the material of the Earth's lower mantle: Stishovite paradox and origin of superdeep diamonds (Experiments at 24–26 GPa). *Geochemistry Int.* **54**, 936–947 (2016).

Liu, W., Yang, Y., Busigny, V. & Xia, Q. K. Intimate link between ammonium loss of phengite and the deep Earth's water cycle. *Earth Planet. Sci. Lett.* **513**, 95–102 (2019).

Liu, Z., Akaogi, M. & Katsura, T. Increase of the oxygen vacancy component in bridgmanite with temperature. *Earth Planet. Sci. Lett.* **505**, 141–151 (2019).

Mahaffy, P. R. *et al.* Abundance and Isotopic Composition of Gases in the Martian Atmosphere from the Curiosity Rover. *Science.* **341**, 263–266 (2013).

Mallik, A., Li, Y. & Wiedenbeck, M. Nitrogen evolution within the Earth's atmosphere–mantle system assessed by recycling in subduction zones. *Earth Planet. Sci. Lett.* **482**, 556–566 (2018).

Marty, B. Nitrogen content of the mantle inferred from N2-Ar correlation in oceanic basalts. *Nature* **377**, 326–329 (1995).

Marty, B. The origins and concentrations of water, carbon, nitrogen and noble gases on Earth. *Earth Planet. Sci. Lett.* **313**–**314**, 56–66 (2012).

Marty, B. *et al.* An evaluation of the C/N ratio of the mantle from natural CO_2-rich gas analysis: Geochemical and cosmochemical implications. *Earth Planet. Sci. Lett.* **551**, 116574 (2020).

Marty, B. & Dauphas, N. The nitrogen record for crust-mantle interaction and mantle convection from Archean to Present. *Earth Planet. Sci. Lett.* (2003).

Marty, B. & Zimmermann, L. Volatiles (He, C, N, Ar) in the Mantle: Assesment of Shallow-Level Assimilation and Fractionation, and Evaluation of Source Composition. *Geochim. Cosmochim. Acta* **63**, 3619–3633 (1999).

Marty, B., Zimmermann, L., Pujol, M., Burgess, R. & Philippot, P. Nitrogen isotopic composition and density of the Archean atmosphere. *Science.* **342**, 101–104 (2013).

Mashino, I., Murakami, M., Miyajima, N. & Petitgirard, S. Experimental evidence for silica-enriched Earth's lower mantle with ferrous iron dominant bridgmanite. *Proc. Natl. Acad. Sci. U. S. A.* **117**, 27899–27905 (2020).

Mazor, E., Heymann, D. & Anders, E. Noble gases in carbonaceous chondrites. *Geochim. Cosmochim. Acta* **34**, 781–824 (1970).

McDonough, W. F. & Sun, S. s. The composition of the Earth. *Chem. Geol.* **120**, 223–253 (1995).

Michael, P. J. The concentration, behavior and storage of H_2O in the suboceanic upper mantle: Implications for mantle metasomatism. *Geochim. Cosmochim. Acta* **52**, 555–566 (1988).

Mikhail, S. & Sverjensky, D. A. Nitrogen speciation in upper mantle fluids and the origin of Earth's nitrogen-rich atmosphere. *Nat. Geosci.* **7**, 816–819 (2014).

Mikhail, S., Barry, P. H. & Sverjensky, D. A. The relationship between mantle pH and the deep nitrogen cycle. *Geochim. Cosmochim. Acta* **209**, 149–160 (2017).

Murakami, M., Hirose, K., Kawamura, K., Sata, N. & Ohishi, Y. Post-Perovskite Phase Transition in $MgSiO_3$. *Science.* **304**, 855–858 (2004).

Murakami, M., Ohishi, Y., Hirao, N. & Hirose, K. A perovskitic lower mantle inferred from high-pressure, high-temperature sound velocity data. *Nature* **485**, 90–94 (2012).

Mysen, B. Nitrogen in the Earth: abundance and transport. *Prog. Earth Planet. Sci.* **6**, (2019).

Nishio-Hamane, D., Yagi, T., Sata, N., Fujita, T. & Okada, T. No reactions observed in Xe-Fe system even at Earth core pressures. *Geophys. Res. Lett.* **37**, 35–38 (2010).

Nishizawa, M., Sano, Y., Ueno, Y. & Maruyama, S. Speciation and isotope ratios of nitrogen in fluid inclusions from seafloor hydrothermal deposits at ~ 3.5 Ga. *Earth Planet. Sci. Lett.* **254**, 332–344 (2007).

Nomura, R. *et al.* Spin crossover and iron-rich silicate melt in the Earth's deep mantle. *Nature* **473**, 199–202 (2011).

Nutman, A. P., Friend, C. R. L. & Bennett, V. C. Evidence for 3650-3600 Ma assembly of the northern end of the Itsaq Gneiss Complex, Greenland: Implication for early Archaean tectonics. *Tectonics* **21**, 5-1-5–28 (2002).

Ono, S., Ito, E. & Katsura, T. Mineralogy of subducted basaltic crust (MORB) from 25 to 37 GPa, and chemical heterogeneity of the lower mantle. *Earth Planet. Sci. Lett.* **190**, 57–63 (2001).

Otsuka, K., Longo, M., McCammon, C. A. & Karato, S. ichiro. Ferric iron content of ferropericlase as a function of composition, oxygen fugacity, temperature and pressure: Implications for redox conditions during diamond formation in the lower mantle. *Earth Planet. Sci. Lett.* **365**, 7–16 (2013).

Oyama, V. I. *et al.* Pioneer Venus Gas Chromatography of the Lower Atmosphere of Venus. *J. Geophys. Res.* **85**, 7891–7902 (1980).

Ozawa, K., Anzai, M., Hirose, K., Sinmyo, R. & Tateno, S. Experimental Determination of Eutectic Liquid Compositions in the MgO-SiO_2 System to the Lowermost Mantle Pressures. *Geophys. Res. Lett.* **45**, 9552–9558 (2018).

Ozima, M. & Podosek, F. A. *Noble Gas Geochemistry* (Cambridge Univ. Press, 2002).

Palme, H. & Nickel, K. G. Ca Al ratio and composition of the Earth's upper mantle. *Geochim. Cosmochim. Acta* **49**, 2123–2132 (1985).

Panero, W. R. Aluminum incorporation in stishovite. *Geophys. Res. Lett.* **33**, 1–5 (2006).

Righter, K. Prediction of metal-silicate partition coefficients for siderophile elements: An update and assessment of PT conditions for metal-silicate equilibrium during accretion of the Earth. *Earth Planet. Sci. Lett.* **304**, 158–167 (2011).

Ringwood, A. E. A Model for the Upper Mantle. **67**, (1962).

Ringwood, A. E. Origin of the Earth and Moon (Springer, 1979).

Robert, F. The D/H ratio in chondrites. *Space Sci. Rev.* **106**, 87–101 (2003).

Rubey, W. *Geologic History of Sea Water*. *Geological Society of America Bulletin* vol. 62 (1951).

Rubie, D. C. *et al.* Accretion and differentiation of the terrestrial planets with implications for the compositions of early-formed Solar System bodies and accretion of water. *Icarus* **248**, 89–108 (2015).

Roskosz, M., Bouhifd, M. A., Jephcoat, A. P., Marty, B. & Mysen, B. O. Nitrogen solubility in molten metal and silicate at high pressure and temperature. *Geochim. Cosmochim. Acta* **121**, 15–28 (2013).

Sagan, C. & Mullen, G. Earth and Mars: Evolution of atmospheres and surface temperatures. *Science.* **177**, 52–56 (1972).

Sakamaki, T. *et al.* Geophysics: Constraints on earth's inner core composition inferred from measurements of the sound velocity of hcp-iron in extreme conditions. *Sci. Adv.* **2**, (2016).

Sakuraba, H., Kurokawa, H. & Genda, H. Impact degassing and atmospheric erosion on Venus, Earth, and Mars during the late accretion. *Icarus* **317**, 48–58 (2019).

Sano, Y., Takahata, N., Nishio, Y., Fischer, T. P. & Williams, S. N. Volcanic flux of nitrogen from the Earth. *Chem. Geol.* **171**, 263–271 (2001).

Sano, Y. & Williams, S. N. Fluxes of mantle and subducted carbon along convergent plate boundaries. *Geophys. Res. Lett.* **23**, 2749–2752 (1996).

Schlichting, H. E., Sari, R. & Yalinewich, A. Atmospheric mass loss during planet formation: The importance of planetesimal impacts. *Icarus* **247**, 81–94 (2015).

Schubert, G. *Venus* (eds Hunten, D. M., Colin, L., Donahue, T. M. & Moroz, V. I.) 681–765 (University of Arizona Press, 1983).

Shcheka, S. S., Wiedenbeck, M., Frost, D. J. & Keppler, H. Carbon solubility in mantle minerals. *Earth Planet. Sci. Lett.* **245**, 730–742 (2006).

Shirey, S. B., Kamber, B. S., Whitehouse, M. J., Mueller, P. A. & Basu, A. R. A review of the isotopic and trace element evidence for mantle and crustal processes in the Hadean and Archean: Implications for the onset of plate tectonic subduction. *Spec. Pap. Geol. Soc. Am.* **440**, 1–29 (2008).

Smart, K. A. *et al.* Diamond growth from oxidized carbon sources beneath the Northern Slave Craton, Canada: A δ13C-N study of eclogite-hosted diamonds from the Jericho kimberlite. *Geochim. Cosmochim. Acta* **75**, 6027–6047 (2011).

Smith, E. M. *et al.* Large gem diamonds from metallic liquid in Earth's deep mantle. *Science.* **354**, 1403–1405 (2016).

Smyth, J. R., Swope, R. J. & Pawley, A. R. H in rutile-type compounds: II. Crystal chemistry of Al substitution in H-bearing stishovite. *Am. Mineral.* **80**, 454–456 (1995).

Sokol, A. G., Sokol, E. V., Kupriyanov, I. N. & Sobolev, N. V. Synthesis of NH4-substituted muscovite at 6.3 GPa and 1000°C: Implications for nitrogen transport to the earth's mantle. *Dokl. Earth Sci.* **479**, 404–407 (2018).

Som, S. M. *et al.* Earth's air pressure 2.7 billion years ago constrained to less than half of modern levels. *Nat. Geosci.* **9**, 448–451 (2016).

Som, S. M., Catling, D. C., Harnmeijer, J. P., Polivka, P. M. & Buick, R. Air density 2.7 billion years ago limited to less than twice modern levels by fossil raindrop imprints. *Nature* **484**, 359–362 (2012).

Speelmanns, I. M., Schmidt, M. W. & Liebske, C. Nitrogen Solubility in Core Materials. *Geophys. Res. Lett.* **45**, 7434–7443 (2018).

Speelmanns, I. M., Schmidt, M. W. & Liebske, C. The almost lithophile character of nitrogen during core formation. *Earth Planet. Sci. Lett.* **510**, 186–197 (2019).

Stern, C. R. Subduction erosion: Rates, mechanisms, and its role in arc magmatism and the evolution of the continental crust and mantle. *Gondwana Res.* **20**, 284–308 (2011).

Stern, R. J. Evidence from ophiolites, blueschists, and ultrahigh-pressure metamorphic terranes that the modern episode of subduction tectonics began in Neoproterozoic time. *Geology* **33**, 557–560 (2005).

Syracuse, E. M. *et al.* The global range of subduction zone thermal models. *Phys. Earth Planet. Inter.* **183**, 73–90 (2010).

Taylor, R. & McLennan, S. M. *The Continental Crust: its Composition and Evolution* (Blackwell Science Publishing, 1985)

Wang, X., Tsuchiya, T. & Hase, A. Computational support for a pyrolitic lower mantle containing ferric iron. **8**, (2015).

Warneck, P., Chemistry of the Natural Atmosphere (Academic, San Diego, 1988).

Wasson, J. T. & Kallemeyn, G. W. Compositions of Chondrites. *Philos. Trans. R. Soc. London. Ser. A, Math. Phys. Sci.* **325**, 535–544 (1988).

Watenphul, A., Wunder, B. & Heinrich, W. High-pressure ammonium-bearing silicates: Implications for nitrogen and hydrogen storage in the earth's mantle. *Am. Mineral.* **94**, 283–292 (2009).

Watenphul, A., Wunder, B., Wirth, R. & Heinrich, W. Ammonium-bearing clinopyroxene: A potential nitrogen reservoir in the Earth's mantle. *Chem. Geol.* **270**, 240–248 (2010).

Wordsworth, R. & Pierrehumbert, R. Warming in Earth's Early Atmosphere. *Science.* **339**, 64–67 (2013).

Xu, S., Lin, J. F. & Morgan, D. Iron partitioning between ferropericlase and bridgmanite in the Earth's lower mantle. *J. Geophys. Res. Solid Earth* **122**, 1074–1087 (2017).

Yang, Y., Busigny, V., Wang, Z. & Xia, Q. The fate of ammonium in phengite at high temperature. *Am. Mineral.* **102**, 2244–2253 (2017).

Yamazaki, D. *et al.* Over 1Mbar generation in the Kawai-type multianvil apparatus and its application to compression of $(Mg_{0.92}Fe_{0.08})SiO_3$ perovskite and stishovite. *Phys. Earth Planet. Inter.* **228**, 262–267 (2014).

Yoshioka, T., Wiedenbeck, M., Shcheka, S. & Keppler, H. Nitrogen solubility in the deep mantle and the origin of Earth's primordial nitrogen budget. *Earth Planet. Sci. Lett.* **488**, 134–143 (2018).

Zedgenizov, D. A. & Litasov, K. D. Looking for 'missing' nitrogen in the deep Earth. *Am. Mineral.* **102**, 1769–1770 (2017).

Zerkle, A. L. & Mikhail, S. The geobiological nitrogen cycle: From microbes to the mantle. *Geobiology* **15**, 343–352 (2017).

Zerr, A. & Boehier, R. Melting of (Mg,Fe) SiO_3-perovskite to 625 kilobars: Indication of a high melting temperature in the lower mantle. *Science.* **262**, 553–555 (1993).